Sea Ice Discrete Element Modeling: Melt and Fracture of Floes and Sheets

Thesis by
Rigoberto Moncada Lopez

In Partial Fulfillment of the Requirements for the
Degree of
Doctorate of Philosophy in Civil Engineering

CALIFORNIA INSTITUTE OF TECHNOLOGY
Pasadena, California

2024
Defended November 13, 2023

ACKNOWLEDGEMENTS

As with any significant endeavor, a thesis is only possible through the support and intervention of multiple people; as humans, we are the result of others' collaboration and contribution, just as we enrich the projects of our peers.

First of all I want thank my advisor Prof. Jose Andrade for the opportunity to work in this amazing area of research and for providing the conditions and freedom to develop my PhD studies. I greatly appreciate his support and advice when I was choosing research topics and the methodology, his insistence on keeping a grasp of the bigger picture and his emphasis on the effective communication of our results. I am also very grateful to Prof. Andrew Thompson for all his guidance regarding the science questions of our work, his always on-spot comments, and for leading the other half of our multidisciplinary collaboration between applied mechanics and geophysical sciences. Moreover, I want to thank my thesis committee, Prof. Nadia Lapusta and Prof. Domniki Asimaki, for their comments and observations when defining our line of research and for improving the quality of our work. I want to thank Prof. Ruby Fu as well for her constant feedback and keen eye in identifying aspects that could more effectively conveyed during our meetings. Furthermore, I want to mention the critical role of my co-authors Prof. Mukund Gupta and Dr. Jacinto Ulloa, all their support and advice during our multiple meetings and their insight of how to approach a research project step by step and how to write good quality papers. In terms of funding, the research in this thesis was supported by the ARO Grant W911NF-19-1-0245 and the NSF grant JEA.NSFCMMIECI-1-NSF.2033779; as well as the award NSF-OCE 1829969 and the Office of Naval Research Multidisciplinary University Research Initiative (MURI) on Mathematics and Data Science for Physical Modeling and Prediction of Sea Ice, N00014-19-1-2421.

I want to acknowledge the help of my COSYMO group members in implementing the image processing (Konstantinos Karapiperis) and LS-DEM implementation (Liuchi Li, John Harmon, and Robert Buarque de Macedo) and for vital discussions and exchanges (Ziran Zhou and John Baglino). I am also thankful for the comments and recommendations of all Sea ice MURI members (particularly Prof. Giannakis and Prof. Manucharyan), and for providing me with the opportunity to learn about the latest sea ice research. I am also very grateful for my Mechanical and Civil Engineering Department colleagues and faculty, from whom I learned a lot about

continuum and solid mechanics and who provided a nice collaborative environment. Also, for the administrative members of MCE, whose aid was essential at so many stages of my PhD.

Outside of Caltech, I want to mention some of my former mentors, including Prof. Motoki Kazama for all his advice during my master's degree and my first publication. Also, I want to thank Prof. Hiromitsu Yamagishi and Prof. Kiyoharu Hirota from the Japanese International Cooperation Agency for getting me more involved in the geosciences and re-igniting in me the spark of research and my desire to keep learning and specializing. Also my colleagues and teachers from UNITEC in Honduras, who laid the foundations of my interest as Civil and Geotechnical Engineer.

More personally, I am infinitely grateful for my parents, Elsa and Rigoberto, who always gave me the freedom to pursue my interests, believed in me finding my own path, and provided the means and support for me to be able to become a professional. I am the person that I am because of them. I also want to thank my parents in-law, Betty and Julio, for all their support and help that has allowed me to develop my work more effectively. I dedicate this work to my daughters, Victoria and Aurora, who are my driving motor to do my best and persevere, and to provide them with a good example for them to follow. Ultimately, I dedicate this work to my wife, Diana, who has been by my side all the way, always pushes me to improve and grow, and particularly encouraged me to apply and come to Caltech. Leaving our prior life in order to come here is a sacrifice she made for which I might never be grateful enough. This achievement is hers as well.

ABSTRACT

Over the last 40 years, the Arctic Ocean has experienced a significant reduction in surface area and thickness of sea ice for its minimum summer and year-round values. Sea ice, existing both as continuous ice sheets and distinct broken floes or blocks, is disappearing earlier and faster over time. These changes are largely occurring within marginal ice zones, where ice is most vulnerable to thermal forcings from the sun, oceans, and atmosphere and wind and ocean currents. Given that sea ice plays a vital role in regulating climate by delaying global energy exchanges, its loss is a vital factor in increasing global temperatures and the frequency of extreme weather events. Understanding and projecting seasonal variations in sea ice is imperative to improve climate predictions. However, many of the processes in sea ice are not fully described by most existing models, due to the limitations of continuum sea ice approaches. As a result the use of discontinuum techniques on sea ice is a very active field. In this work, we combine discrete element methods with satellite image analysis to study changes in sea ice concentration and floe size distribution during the summer melt transition for ensembles of distinct floes decaying into open waters and continuous fast sea ice sheets breaking into multiple floes. For the pure floe-like behavior, we use the 'Level Set Discrete Element Method for Sea Ice' or LS-ICE method. This model can resolve individual sea ice floes with realistic shapes, and represent their physical interactions by leveraging level-set functions to detect contacts. LS-ICE can also be coupled to atmospheric and oceanic heat and momentum forcings and simulate associated melt and breakage processes. With it, we are able to reproduce sea ice concentration decline for the summers of 2018 and 2020 at Baffin Bay. Using LS-ICE we also unveil the sensitivity of sea ice loss and floe size distribution to different intensities of fracturing and ocean/solar melt and how sea ice floe size determines which is more dominant. For monolithic landfast sea ice sheets, we use a bonded particle method within the level set discrete element model called LS-DEM-BPM. We explore the relationship between landfast sea ice breakage and area decline, ocean currents and floe size distribution for a region in Fram Strait in 2023. We also replicate its fracture characteristics, using idealized pulses and arbitrary eddying ocean currents, and unveil particular combinations of wavelengths and wave speeds that facilitate breakage. Our results give new insight on sea ice melt and breakage interactions and provide a numerical framework for simulating the complete transition of sea ice from intact sheets to open oceans.

PUBLISHED CONTENT AND CONTRIBUTIONS

Moncada, R., Ulloa, J., Gupta, M., Thompson, A., & Andrade, J. (2024). Impact of ocean currents on landfast sea ice fracture: Bonded discrete element method analysis. *Computer Methods in Applied Mechanics and Engineering. In Preparation.*

R.M. participated in the conception of the project, adapted an existing bonded particle method for landfast sea ice, added eddying ocean current input as forcings into the simulations, developed the code to analyze sea ice sheet and floes from satellite data, interpreted results, generated post-processing output, and participated in the writing of the manuscript.

Moncada, R., Gupta, M., Thompson, A., & Andrade, J. (2023). Level set discrete element method for modeling sea ice floes. *Computer Methods in Applied Mechanics and Engineering*, *406*, 115891. https://doi.org/10.1016/j.cma.2023.115891.

R.M. participated in the conception of the project, developed the sea ice breakage and melt code modules for the LS-ICE method, solved and analyzed simulation results, prepared and processed satellite images and input data, and participated in the writing of the manuscript.

Moncada, R., Gupta, M., Thompson, A., & Andrade, J. E. (2023). Role of breakage, melt and floe size distribution on sea ice summer transition. *Geophysical Research Letters. In Review.*

R.M. participated in the conception of the project, worked in defining the specific independent and dependent variables to develop the experiments, managed the data and post-processing, and participated in the writing of the manuscript.

TABLE OF CONTENTS

LIST OF ILLUSTRATIONS

LIST OF TABLES

NOMENCLATURE

BPM. Bonded Particle Method.

CFND. Cumulative Floe Number Distribution, widespread way of keeping track of FSD in sea ice literature. Instead of just counting number of floes as in the FND, it accumulates from larger to smaller sizes the amount of floes equal to or smaller than the FSD bins.

DEM. Discrete/Distinct Element Method.

Equivalent Diameter. Diameter of a floe with an arbitrary shape if it were transformed into a circular floe with the same area.

Fast ice. Also known as landfast sea ice. Mass of sea ice in the form of a monolithic sheet formed by the anchoring or grounding at coasts of large agglomerations of floes.

Floe. Distinct block of sea ice formed from freezing at the surface of ocean waters or from the breakage of a larger sea ice sheet or landfast sea ice.

FND. Floe Number Distribution, widespread way of keeping track of FSD in sea ice literature. It measures the number of floes within a unit cell or total domain which comply with certain size requirements.

FSD. Floe size distribution, sea ice analogue of the grain size distribution used in soil mechanics. Percent mass or number count of a grains within a particular size range, grouped in bins as a histogram.

GPU. Graphical Processing Unit.

HYCOM. Hybrid Coordinated Ocean Model.

LS-DEM. Level Set Discrete Element Method.

LS-ICE. Level Set Discrete Element Method for Sea Ice.

MITgcm. Massachusetts Institute of Technology General Circulation Model.

MIZ. Marginal ice zone, transitional zone between a solid ice sheet and the open ocean.

MODIS. Moderate Resolution Imaging Spectroradiometer.

NASA. National Aeronautics and Space Administration.

RMSE. Root Mean Square Error.

Rossby Number. Ratio of inertial forces, caused by ocean current velocities, to Coriolis forces, induced by the earth's rotation..

Chapter 1

INTRODUCTION

1.1 Full Thesis Summary

Understanding and projecting seasonal variations in sea ice is necessary to improve global climate predictions. However, accurately capturing changes in sea ice and its interactions with ocean and atmosphere variability remains a challenge for models, notably due to the complex behavior of sea ice at the floe scale. In this work, we introduce a method to capture the floe-like behavior of sea ice, named the 'Level Set Discrete Element Method for Sea Ice' (LS-ICE). This model can resolve individual sea ice floes with realistic shapes, and represent their physical interactions by leveraging level-set functions for detecting contact between floes. LS-ICE can also be coupled to heat and momentum forcings from the atmosphere and the ocean, and simulate associated melt and breakage processes. The discrete representation of sea ice floes reveals melt dynamics, associated with their shapes and thickness distributions, which are currently not well represented by continuum models. We illustrate the model capabilities for two different years involving the spring to summer transition in Baffin Bay, where the sea ice concentration declines from approximately 80% to 0% between the months of June and July. Satellite imagery, along with oceanographic reanalysis data based on field measurements, are used to initialize the model and validate its subsequent evolution during these months. For an appropriate set of parameters, the model can reproduce the evolution of sea ice concentration, floe size distribution, oceanic temperature and mean sea ice thickness, despite only a small number of tunable parameters. This study identifies the potential for LS-ICE to simulate the interaction between floe shape, melt and breakage, to enhance seasonal scale forecasts for sea ice floes.

With LS-ICE as a method for distinct floe analysis we can proceed to unveil more aspects of the Marginal Ice Zone and its Floe Size Distribution. MIZs are composed of individual sea ice floes, whose breakage and melt shape summer behavior of the pack. These processes are generally not resolved by global or regional models, due to the continuum approximations used for sea ice. Here, we leverage the advantages of the Discrete Element Model to investigate the summer transition of floes within Baffin Bay during June–July 2018. The model is initialized with imagery-based shapes and evolved using characteristic forcings from the region and a range of model parameters. For the parameter regime that best fits observations, breakage and melt both impact mass loss of resolved floes (>2 km). The mass loss and floe size distribution are most sensitive to the breakage rate, compared to solar and oceanic melt parameters. The number decay of the largest floes (>13 km) is controlled by breakage, while decay of smaller floes (2 – 13 km) depends strongly on lateral melt.

After focusing on already broken sea ice floes, we then shift to the study of solid ice sheets. Given that sea ice in the polar regions is subject to a variety of dynamic and thermodynamic processes its permanence throughout the year can be very difficult to predict and it is history-dependent. Wind forcing, ocean currents, thickness reduction due to temperature increases in ocean and atmosphere, floe collisions and wave action all contribute to induce the breakdown of sea ice through fracture and melt. An example of sea ice that has transitioned from multi-year permanence to seasonal formation and collapse are landfast sea ice sheets, which can span hundreds of square kilometers along coastal areas. Landfast sea ice or fast ice plays a vital role in regulating global climate, buttressing glacier shelves, facilitating offshore human activities and reducing coastal erosion. Fast ice is weakened by melt and it is fractured at its edge into smaller fragments. Breakage of edge fragments allows stronger currents to mobilize inward and induce the fracture of more ice. This breakage process can be conditioned by particular ocean current regimes. Loss of sea ice results in enhanced ocean current and eddy activity which in turn breaks and leads to the removal of more sea ice. In a similar way sea ice melt results in reduced albedo, which promotes ocean warming and even more melt. Hence a feedback loop exists not only for temperature but also for ocean currents that break up fast ice. Sea ice sheet fracture by ocean current forces regulate the floe size distribution as a product the breakage process. Conversely, ocean currents and wind forcing information could be deduced from the FSD obtained from observations. Adequate fast ice modeling is a pressing matter, as it defines the characteristics of the floe mosaics that are explored in this work, and how FSD impacts concentration decline. So, we proceed to use a bonded particle method within the level set discrete element model (LS-DEM-BPM) to explore the relationship between fast ice breakage, ocean currents, floe size distribution and concentration. As a benchmark, we choose a fast ice region in Fram Strait during 2023 and numerically replicate its fracture characteristics, using first idealized unidirectional pulse and then eddying ocean currents. For an idealized application of in-plane horizontal ocean currents, particular combinations of wavelengths and wave propagation speeds for horizontal velocity distributions result in more uniform FSDs and a greater prevalence of fast ice breakage. These ocean current parameters are then generalized to more arbitrary currents with characteristic eddy filament wavelengths, which can generate several small floes for more diffuse eddies or fewer large floes for sharp filament-like eddies. We find out that it is possible to approximate in situ breakage FSD conditions under certain combinations of diffuse eddying currents. Using this model, we can then tie in-situ measurements and climate models to understand and forecast future fast ice fracture events and also feed these results to LS-ICE and understand better the FSD and concentration changes along the spring to summer transition of sea ice.

1.2 Key Points

- Level sets can be used to accurately represent sea ice floe geometries inferred from satellite images and model their contact and kinematics via the discrete element method.
- LS-ICE can model floe breakage and non-uniform basal melt from the ocean and emulate the statistical evolution of sea ice floes in Baffin Bay during the spring to summer transition.
- Breakage and melt are comparably important in the summer decay of sea ice floes over Baffin Bay for the period and area analyzed in 2018 and similar results are obtained for the same region in 2020.
- The fracturing of the sea ice pack is essential to reproduce the observed sea ice decline within a discrete element model.
- The evolution of the floe size distribution is governed by breakage for large floes (> 13 km) and lateral melt for smaller floes (2–13 km).
- Breakage of a single sheet of fast ice can be modeled using a bonded particle version of LS-DEM, which is able to replicate fractal sheet breakdown into smoother floes and ice sheet decline in the spring to summer transition in Fram Strait for 2023.
- Critical factors for fast ice breakdown include wavelength of ocean eddies and wave propagation speeds. Longer wavelengths result in an increased destruction of fast ice into several small floes, but there is cutoff length below

which breakage is possible and above which differential currents are unable to exceed critical ice strength.

1.3 Introduction: Importance of Sea Ice

Sea ice is a vital component of the global climate system. It forms at the poles when surface ocean waters cool below their freezing point as a result of cold atmospheric temperatures. The ice is distributed in relatively thin layers (~ 0.1 – 0.5 m), but may subsequently grow to several meters in thickness due to snow accumulation, further cooling from the atmosphere, and mechanical packing as ice is deformed from winds, ocean currents and waves. In both the Arctic and Antarctic oceans, sea ice experiences a large seasonal cycle, with extended sea ice area in the winter and spring seasons, followed by much reduced sea ice concentration and thickness during summer and fall. This transition can also be observed spatially (Figure 1.1) from a continuous sheet, to a marginal ice zone (MIZ) of distinct floes, to sea ice slurry or fine floe area and into the open ocean. In addition to these variations in a particular region, significant spatial differences exist between and within the two polar oceans, due to differing land boundaries, atmospheric wind and radiative conditions, as well as ocean currents over synoptic and meso-scales. This heterogeneity in sea ice behavior poses a serious challenge for modelling sea ice in climate models, particularly as the spatial resolution of most remote sensors and continuum models is too coarse to resolve detailed mechanisms occurring at the sub-grid scale. Current climate models have significant uncertainty when projecting the negative trend in Arctic sea ice extent over the past decades (Notz & Community, 2020; Roach et al., 2018; Rosenblum & Eisenman, 2017), motivating the need for the development of improved numerical sea ice representations that can be efficiently incorporated into global-scale climate models.

In the last few decades, sea ice pack in the Arctic Ocean has experienced significant decline in areal concentration, multi-year ice fraction and thickness (Deser et al., 2010; Moon et al., 2021; Serreze & Stroeve, 2015b; Stroeve et al., 2014). The steady decrease in sea ice cover or extent (Figure 1.2) is causing a longer ice-free season (Kwok, 2004; Min et al., 2021; Tooth & Tschudi, 2018; Wei et al., 2019), with greater absorption of solar heating due to the ice albedo feedback. These summer-time changes in the pack are not well captured by climate models given the sea ice system's complex behavior that makes forecasting a challenging process (Andersson et al., 2021; Blanchard-Wrigglesworth et al., 2015; Guemas et al., 2016; Olonscheck et al., 2019; Serreze & Stroeve, 2015a). One of the factors that may

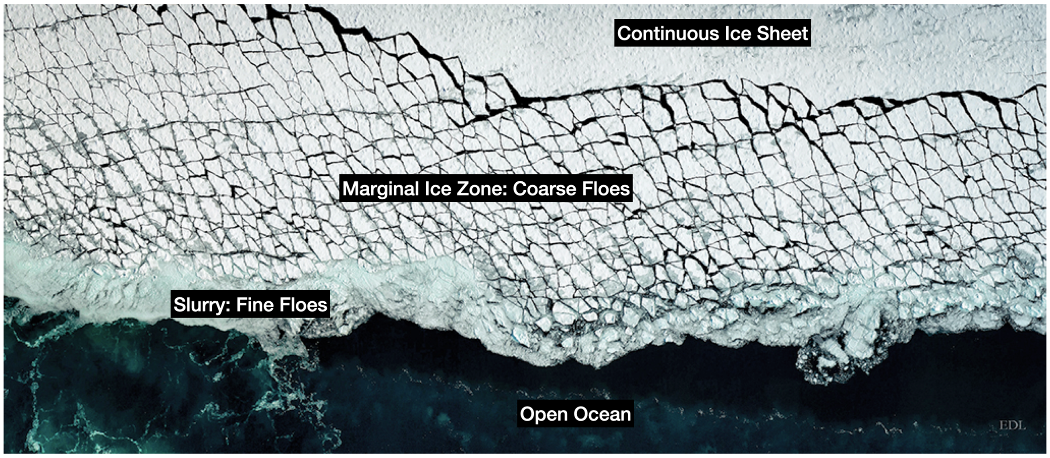

Figure 1.1: Transition of sea ice from a continuum sheet, to a MIZ, to fine floes, to open ocean. (Squire, 2022)

limit predictions is the lack of resolution at the scale of individual sea ice floes and the inability to capture the discrete-element physics of floes fracturing and melting in response to forcings from the ocean and atmosphere.

Global temperature increase has been especially intense in the Arctic region (Deser et al., 2010; Rantanen et al., 2022; Serreze & Stroeve, 2015a). Sea ice is a component in the polar regions that is highly susceptible to temperature change and external forcing. Its formation can be easily inhibited and it disintegration accelerated by these alterations (Kwok, 2004; Tooth & Tschudi, 2018; Wei et al., 2019). As a result, specially in the Arctic, sea ice concentration has declined and its properties have been significantly degraded, including snow cover, thickness and brine content (Moon et al., 2021; Stroeve et al., 2014).

Decline in sea ice concentration in the Arctic over the satellite record has motivated research on the mechanisms and rates of sea ice removal. Minimum Sea ice extent during the summer has reached record values, particularly in the last 15 years (Kumar et al., 2020; Meier, 2021). This has resulted in the removal of multi-year sea ice, either as discrete floes or monolithic landfast sheets, that used to survive the melt season. Most of existing floes and landfast sea ice are now first-year only (see Figure 1.3), with significant weaker properties and are easier to melt (Kacimi & Kwok, 2022; Kwok, 2018; Li et al., 2019). Similarly, Antarctic sea ice has been observed to start declining in area as well (Suryawanshi et al., 2023).

Sea ice loss in the northern hemisphere is bound to have a significant impact in climate stability (Zhang et al., 2023), as it presence delays the energy exchange

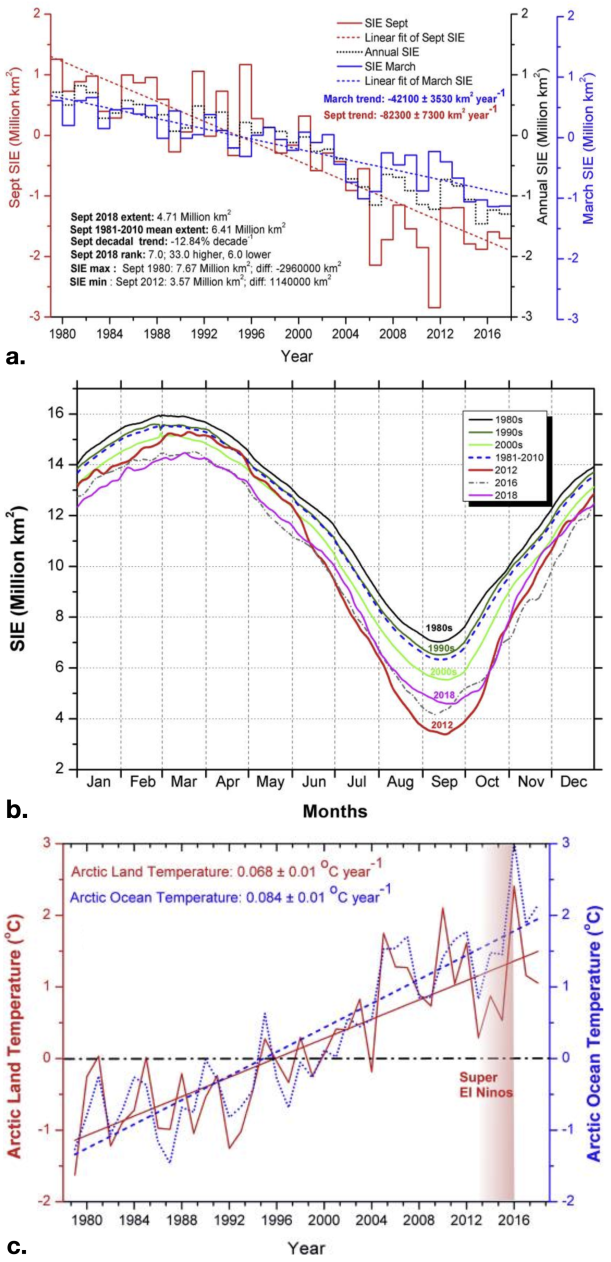

Figure 1.2: Arctic sea ice decline and its relation to temperature. a. Evolution of sea ice extent (SIE) trend for each March and September from 1980 to 2016. b. Monthly variation of sea ice for different years, note that while the same cyclic trends hold, the extent or concentration shifts down over time. c. Arctic land and ocean temperature anomalies from 1980 to 2018, ocean anomalies tend to be slightly higher (Kumar et al., 2020).

between the atmosphere and the ocean. Without sea ice, ocean temperatures rise at a much higher rate which results in perturbation of circulation currents that can then induce the frequency and intensity of events such as cyclones, storms, hurricanes

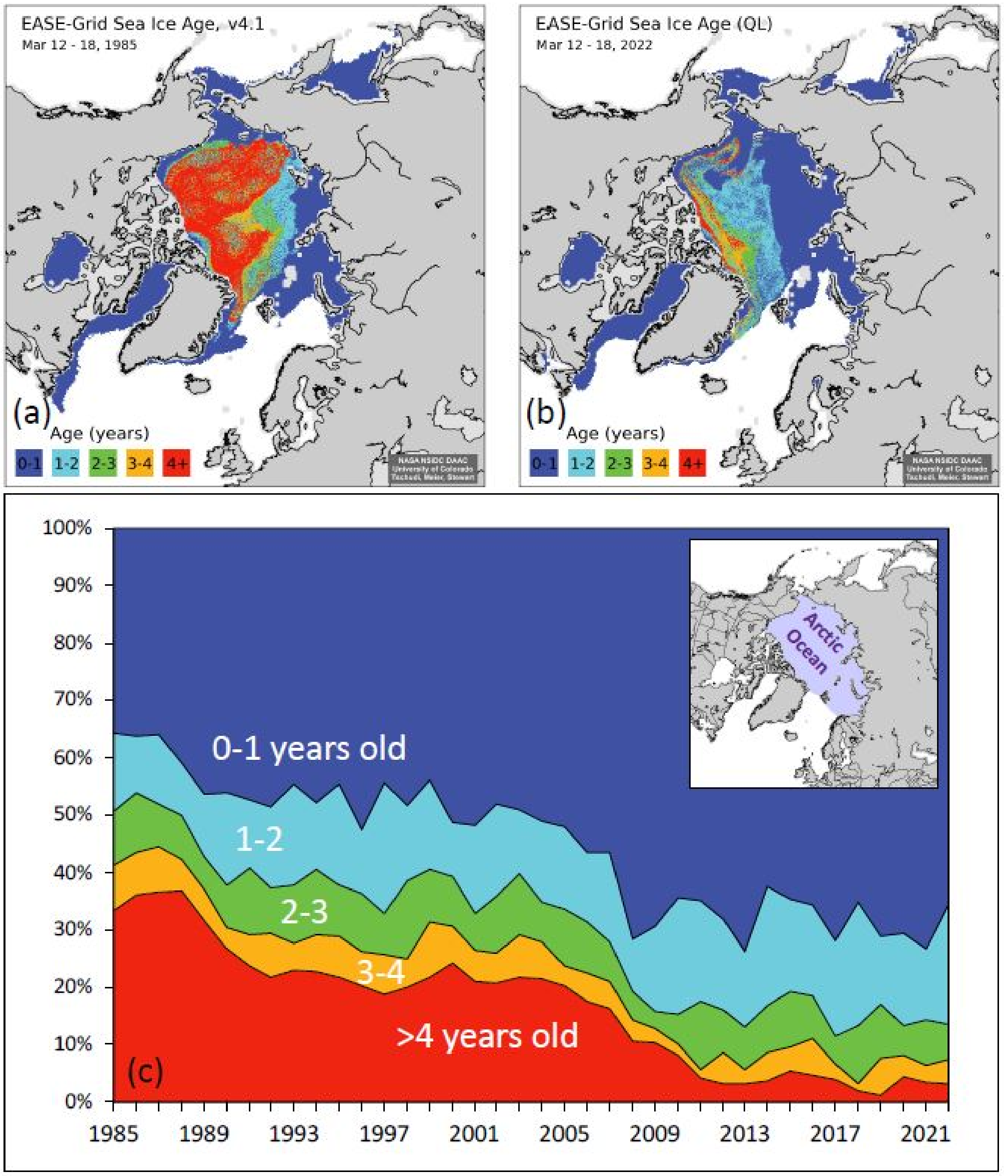

Figure 1.3: Sea ice changes in age: a. Distribution of Arctic sea ice age in 1983 according to its age. b. Distribution of Arctic sea ice age in 2022 according to its age. c. Evolution of the fraction for different ages of sea ice. (NSDIC, 2022; Serreze & Meier, 2018)

and droughts (Cohen et al., 2014; Jenkins & Dai, 2021; Valkonen et al., 2021). Knowing when specific regions of the Arctic will be completely ice-free during the summer, might aid in better predictions of climate models and policy-making. However, better models to predict this ice-free regime are necessary first. One of the most challenging aspects of studying sea ice is that, under this changing climate, it is a continuously evolving system (Figure 1.4). As part of its life cycle, sea ice in several regions starts as a monolithic ice sheet or fast ice, often fixed to land (Hwang & Wang, 2022). As wind and ocean currents act on this sheet, and if it has been partially melted underneath by warmer waters, it starts fracturing into very large floes. These very large floes can then be advected to regions with higher temperature, more aggressive currents and into floe fields that can induce higher stresses. As a result, larger floes break fractally into smaller blocks. Larger blocks tend to retain angular shapes and most of their initial thickness. But as floes are broken into smaller fragments they start chipping or wearing away into more rounded objects and they start melting more laterally and vertically, as temperature rises during the summer both in the atmosphere and ocean. Eventually they might decay into a very fine slurry and completely melt. When temperature decreases again towards the winter, new floes are formed and agglomerate into a new ice sheet, combining with any surviving floes (Lei et al., 2020; Lin et al., 2022).

We can conclude that to simulate this cycle better, reproducing the fracture behavior of sea ice is essential, as it determines when a particular floe or region breaks and what is the specific location and shape of this fracture. As this breakage affects the geometry of the smaller floes that will then be split again and expose priorly isolated sea ice, this is a history-dependent process for which initial conditions will affect the behavior of the system. In addition of the temporal and spatial evolution of geometry for future mechanical processes, geometry is also coupled to changing thermodynamic conditions affecting sea ice. For example, a region of fast ice breaking into fine and uniform fragments will lose more mass by melt than one that breaks into larger and well-graded blocks due to the increased surface area. This changing geometry also affects atmospheric and oceanic currents as well, since larger floes result in a stronger ice-ocean momentum exchange and dissipate inertial forces more effectively (Watkins et al., 2023; Willmes et al., 2023).

It also known that the sea ice floe size distribution (FSD) of the broken floe regime, heavily depends on breakage phenomena and is coupled to fluid thermal exchanges, strength of melt, thickness reduction and internal stresses (Bateson et al., 2020; Stern, Schweiger, Stark, et al., 2018). FSD is also a critical parameter for climate and numerical models to approximate large scale sea ice behavior. And just like other conditions, FSD ends up coupling with thermal and mechanical effects that then affect fracture.

During the fracture stage with contribution of melt to accelerate this breakage, multi-kilometer fast ice sheets transition into floes, until this sheet is mostly or

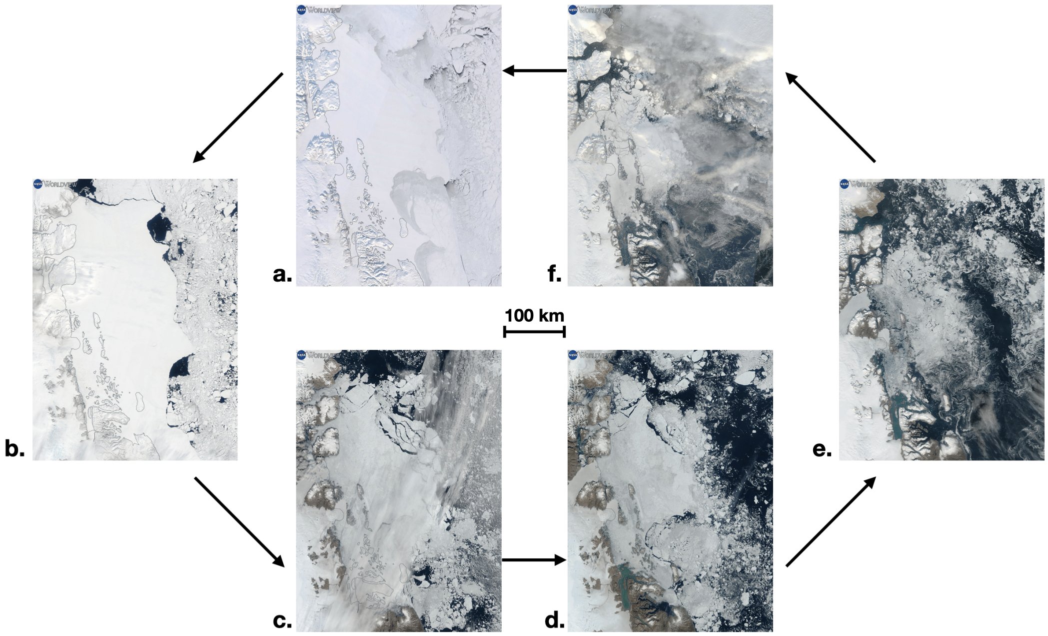

Figure 1.4: Example of sea ice life cycle, from MODIS snapshots of Fram Strait. a. March 14, 2023: Initial solid sea ice sheet with a few fractures and defects. b. June 1, 2023: Ice sheet decaying into several coarse floes, forming a marginal ice zone. c. July 31, 2023: Ice sheet shrinking and coarse floes becoming more widespread. d. August 8, 2023: More coarse floes are broken into fines or sea ice slurry and fast ice is almost gone. e. September 12, 2023: All sea ice is reduced into fines and open ocean, tending to zero concentration. f. September 23, 2023: As temperatures decrease towards fall and winter, sea ice starts refreezing at the coast and fast ice begins forming again until it creates a new solid sheet.

completely removed. Loss of sea ice results in enhanced ocean current and eddy activity (Armitage et al., 2020) which in turn breaks more and leads to the removal of additional sea ice. Greater abundance of first year ice and frequency of storm and rainfall events (Dou et al., 2022) is resulting in widespread sea ice sheet fracture and more mobile sea ice and this first-year-only trend increases over time (Asplin et al., 2014; Barber et al., 2018). Asides from its contribution to global climate stabilization and atmosphere and ocean energy exchange buffering, fast ice plays a very important role in reducing coastal erosion, buttressing ice shelves of glaciers, allowing human activities such as hunting, fishing and access to oil platforms, conditioning navigation of ships (Figure 1.5), and providing support for different lifeforms such as polar bears, seals, microorganisms and algae (Figure 1.6) (Steiner et al., 2021). Hence, accelerating and widespread fast ice fracture is inducing significant changes in the cryosphere and it requires to be understood and forecasted better.

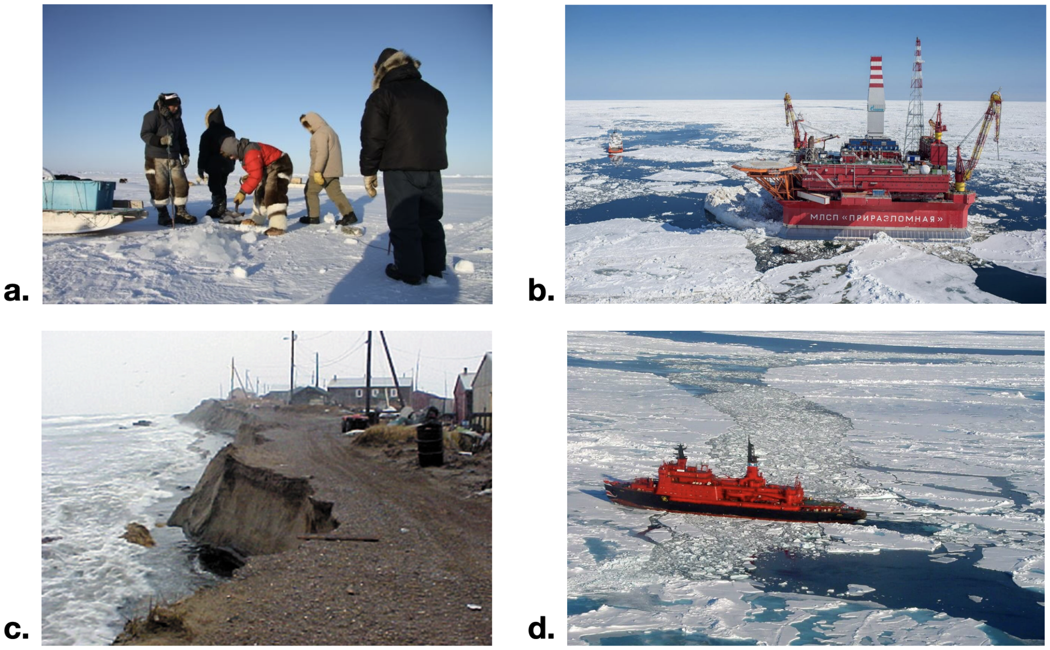

Figure 1.5: Examples of human activities affected by sea ice: a. Fishing and hunting (RadioCanadaInternational, 2013), b. Access to and interaction with ocean platforms (TheArcticInstitute, 2011), c. Coastal erosion and protection of permafrost (NOAA, 2022), d. Impact in polar navigation (ESA, 2021).

The floe-like and fast-ice behavior of sea ice has been investigated from aerial and satellite imagery, which report on floe size distribution (FSD) typically characterized by a power law relationship (Denton & Timmermans, 2022; Horvat et al., 2019; Rothrock & Thorndike, 1984; Steele, 1992; Stern, Schweiger, Stark, et al., 2018). The exponent of this power law, α, varies seasonally, with a shallower slope (evenly-distributed floe sizes) in winter and a steeper slope (several smaller floes and very few larger floes) in summer (Figure 1.7), before major removal of sea ice. During the spring-to-summer transition, floe breakage due to waves, floe collisions and melt fractures can steepen the FSD, while basal and lateral melt can cause a shoaling of the FSD due to their preferential impact on dissipating smaller floes (Hwang & Wang, 2022; Stern, Schweiger, Stark, et al., 2018). Breakage and melt processes are also coupled, since smaller floes tend to be more prone to lateral melt (Gupta & Thompson, 2022a; Horvat et al., 2016; Perovich & Jones, 2014; Steele, 1992), and thinner floes are more susceptible to fragmentation due to melt ponds and other weaknesses within the ice (Hwang et al., 2017; Ren et al., 2021).

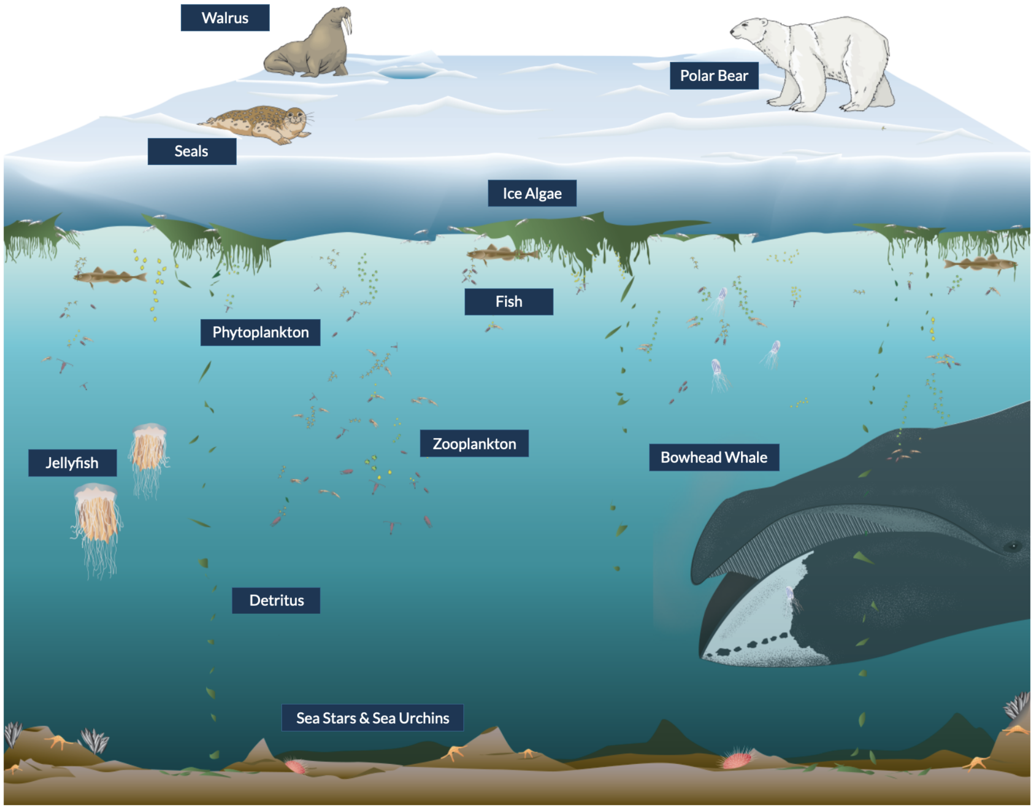

Figure 1.6: Organisms having significant interactions with sea ice extent. (WHOI, 2023)

1.4 Numerical Modeling of Sea Ice

Sea Ice Floe Modeling

Traditional sea ice modelling has sought to represent sea ice as a continuous fluid with parameterized rheology representing the effects of internal stresses, as ice is stretched and deformed from external forces (Figure 1.8). A variety of different rheologies have been developed, such as the Elastic-Viscous-Plastic (EVP), Elastic-Brittle (EB) and Viscous-Plastic (VP) representations (Coon et al., 1998; Feltham, 2008; Girard et al., 2011; Gray & Morland, 1994; Hibler, 1979; Hunke & Dukowicz, 1997; Kimmritz et al., 2017; Koldunov et al., 2019), which evolve gridded averages of sea ice drift, areal concentration, and thickness.

This is achieved by parameterizing the effects of finer scale processes, such internal deformation strength, floe collisions and ocean wave energy dissipation. When appropriately calibrated, this continuum-based approach has several advantages, including its computational efficiency (Koldunov et al., 2019), its ability to mesh

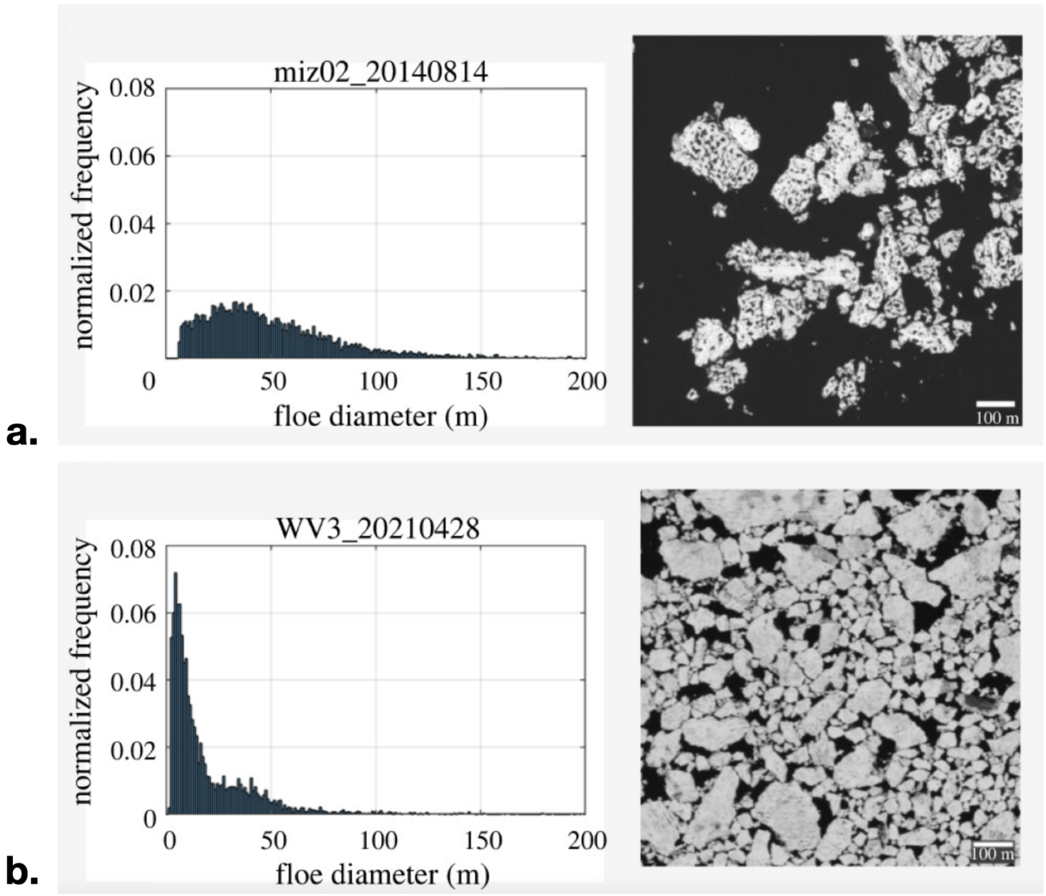

Figure 1.7: Examples of floe size distributions: a. Shallow slope or well-graded floe size distribution with MODIS snapshot for reference. b. Uniform or steep slope floe size distribution with MODIS snapshot for reference (Hwang & Wang, 2022). While not exactly the same method as explained later, the slope can be defined by plotting an imaginary straight line from the smallest size frequency value to the largest size frequency value. Note how the slope of a. is more shallow or less negative than b.

easily with ocean and atmospheric grids (also treated as continuum), and its relative success in modelling large-scale sea ice behavior.

Nonetheless, employing continuum sea ice models at increasingly higher resolutions may not be appropriate, as they are not explicitly designed to represent fine scale processes, and may therefore produce biased behavior. Instead of a continuous fluid, sea ice at finer scales consists of a collection of mechanically and thermodynamically interacting floes, whose sizes range between several meters to tens of kilometers. As the grid resolution approaches these scales, the floe-like behavior of sea ice becomes dominant. These dynamics are apparent in regions where the ice has been broken up by the action of winds, ocean waves and currents, notably within the marginal ice zones (MIZ). With anthropogenic climate change, the Arctic sea ice pack is expected to become more fragmented, less concentrated, thinner, and with a higher fraction of first-year ice, rather than consolidated multi-year floes (Notz & Community, 2020; Roach et al., 2018). Since weaker and thinner ice is more prone to breaking and melting, this transition to the 'New Arctic' may be associated with a positive albedo feedback, which further accelerates the warming of the polar oceans. The combination of these fine-scale processes, coupled to large scale climate dynamics, may then result in ice-free summers for the entire Arctic Ocean in less than two decades from now (Guarino et al., 2020). Improving our understanding of these floe-scale processes is therefore a pressing issue.

To improve sea ice modelling at the floe scale, discrete element methods (DEMs) have been developed to study floe-floe collisions, drag interactions with the ocean and the atmosphere (Gupta et al., 2020; Herman, 2011, 2013; Rabatel et al., 2015), floe agglomeration, as well as sintering and detachment processes (Dansereau et al., 2017). DEMs have also been employed to understand the breakage of bonded floes due to ocean waves (Herman, 2017), breakage and melting evolution from an ice sheet using polygonal tessellation (Manucharyan & Montemuro, 2022) or bonded particles (West et al., 2021), and interactions with naval structures (Tuhkuri & Polojärvi, 2018) and ships on broken and unbroken ice fields (Jou et al., 2019), among several other implementations (Damsgaard et al., 2018; Gutfraind & Savage, 1997; Hopkins, 2004). DEMs (Figure 1.9) have also provided insight into the interactions between land and sea ice within narrow straits, in which the melting of sea ice floes plays an important role in regulating the overall movement of sea ice across straits (Moore et al., 2021; West et al., 2021). In addition, this approach has allowed a better understanding of how external forcing induces ice-wave interaction (Xu et al., 2012) and drift (Rabatel et al., 2015). These modelling studies have been complemented with advances in the observations of individual sea ice floes, and the tracking of their motion as they drift in response to ocean currents and atmospheric winds (Lopez-Acosta et al., 2019).

Sea Ice Floe Size Distribution Modeling

Statistical models of floe size and thickness distributions evolution, in particular, have been used to represent the effect of floe-scale processes in climate models, but the appropriateness of these parameterizations remains uncertain due to challenges in validating models from observations (Bateson et al., 2020; Bateson et al., 2022;

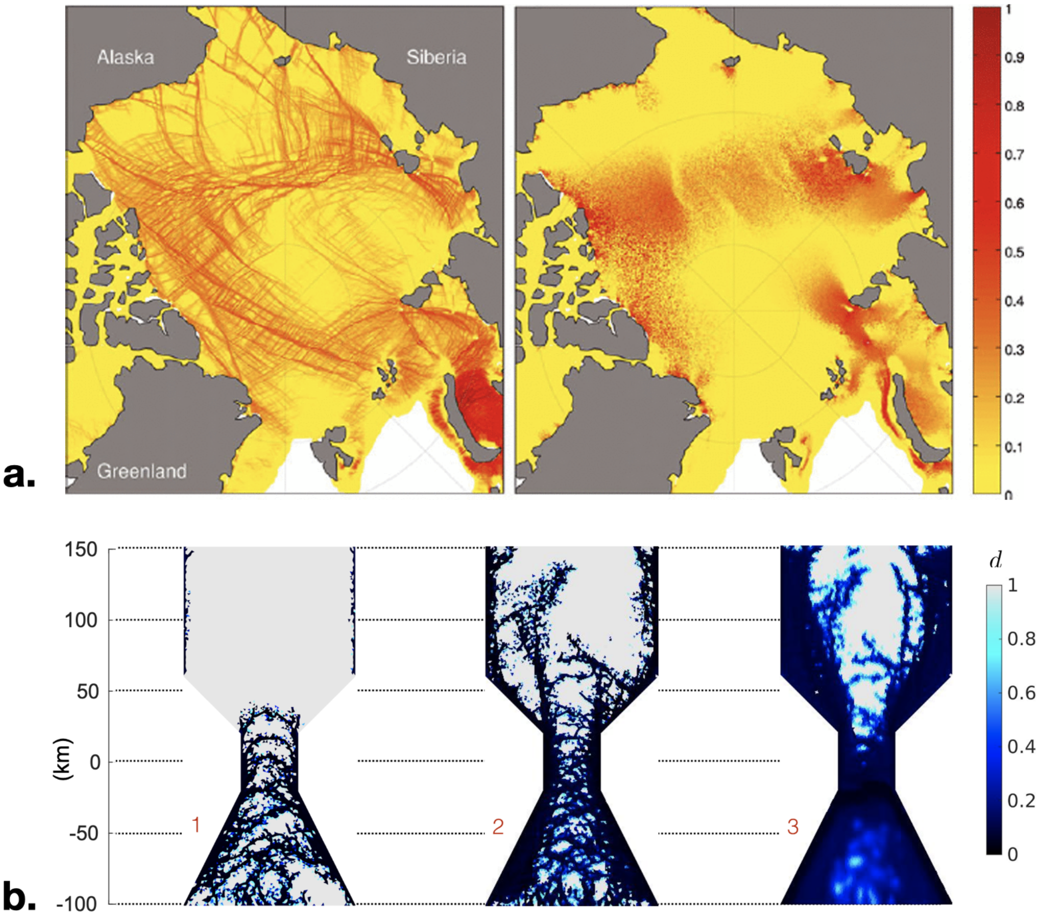

Figure 1.8: Examples of sea ice continuum models showing damage distribution in in their respective color bars (varying from 0 to 1) for: a. Elasto-brittle rheology with (left) and without (right) reduction of elastic modulus as the damage parameter evolves from 0 to 1 (Girard et al., 2011) and b. Maxwell elasto-brittle rheology to plot damage evolution of sea ice at a straight (Dansereau et al., 2017).

Horvat & Tziperman, 2015; Horvat & Tziperman, 2017; Roach et al., 2019; Roach et al., 2018).

To study sea ice floe size distribution several studies have been developed from observations of aerial photography, satellite data and instrumentation (Rothrock & Thorndike, 1984; Steele, 1992; Stern, Schweiger, Stark, et al., 2018) to describe floe mosaics and their change over time. From these observations and reanalysis data, sea ice numerical models that account for floe size distribution have been created, expanding continuum methods that previously did not account for FSD effects, like enhancing the CICE (Community Ice CodE) model (Rae et al., 2015; Roberts et al., 2018). Examples such as the prognostic FSTD (Floe-Size-Thickness distribution)

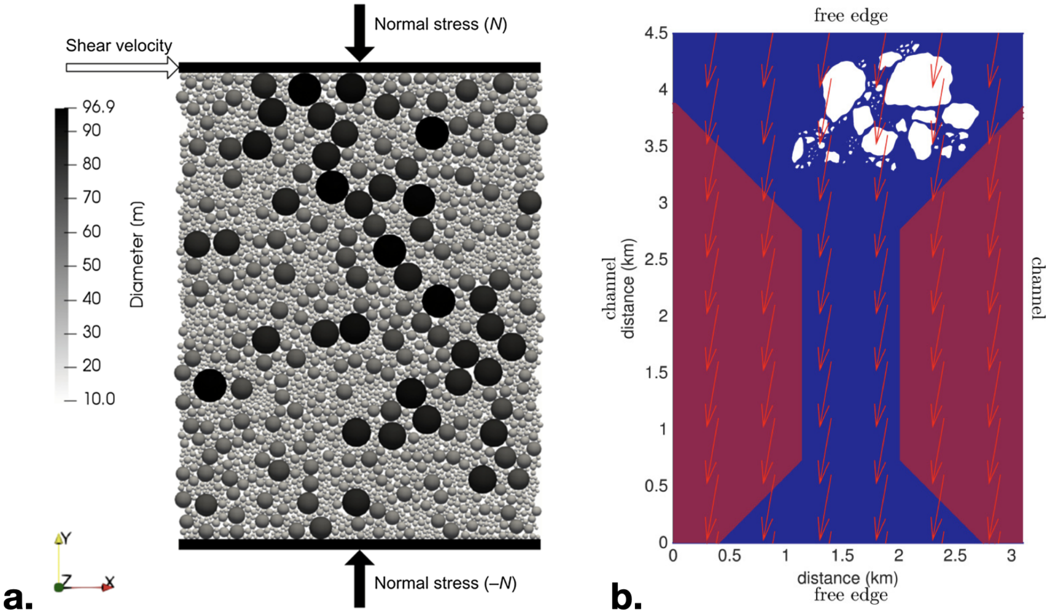

Figure 1.9: Examples of sea ice discrete element models under different conditions such as: a. Uniaxial loading on a floe array as done by (Damsgaard et al., 2018), and b. Floes going through an idealized channel (Rabatel et al., 2015).

model (Roach et al., 2019; Roach et al., 2018), the WIPoFSD (Waves-in-Ice module and Power law Floe Size Distribution) model (Bateson et al., 2020; Bateson et al., 2022), the FSDv2-WAVE model (Horvat & Tziperman, 2015; Horvat & Tziperman, 2017) and the CPOM-FSD (Center for Polar Observation and Modeling) (Roach et al., 2019; Roach et al., 2018; Y. Wang et al., 2022) have been implemented to study the role of sea ice floe size distribution with respect to concentration, melt, seasonal changes, wave breakage, among other factors.

Based on current understanding of sea ice from prior research, a widespread approach to characterize floe size distribution is by plotting cumulative floe number distribution (CFND) or floe number distribution (FND) versus floe size grouped in bins. Commonly and with sufficient spatial resolution (Denton & Timmermans, 2022; Horvat et al., 2019), a power law behavior has been obtained from this CFND or FND versus floe size plots based on observations, from the meter up to the kilometer scale, where $N(x) = Cx^{-\alpha}$ where N represents the number of floes, C is a fitting constant, x is floe size and α is a power law exponent or uniformity coefficient. While FSD is not always observed to behave as a power law (Herman et al., 2021), it is often a valid metric to assess the state of floes over time and space (Hwang & Wang, 2022; Hwang et al., 2017; Perovich & Jones, 2014; Stern, Schweiger, Stark, et al., 2018; Stern, Schweiger, Zhang, et al., 2018). Typical ranges for the power law exponent are in ranges of $\alpha = 1.6$ to 3.6 (Hwang & Wang, 2022; Stern, Schweiger, Stark, et al., 2018) when obtained from FND versus floe size. A higher FSD exponent or coefficient is often related to increased perimeter or surface area and more floe uniformity. This is because a more uniform distribution is associated to a larger number of smaller floes for which more perimeter is exposed per concentration value, compared to regimes with fewer and larger floes. Studies have found that in the winter to summer transition this exponent increases as sea ice breaks apart and decreases when refreezing occurs at the beginning of the fall to winter transition (Hwang & Wang, 2022; Perovich & Jones, 2014).

More recently, discrete element models (DEMs), with explicit representations of floes, have been proposed to help elucidate the dynamics of floe-scale processes and may provide a path towards developing better parameterizations for the FSD and FTD (Floe thickness distribution). DEMs have effectively been used to study the effects of waves on sea ice breakage (Herman, 2017; Montiel & Squire, 2017), glacier calving (Åström et al., 2021) and the effects of winds in setting the floe size and thickness distribution within narrow straits (Manucharyan & Montemuro, 2022; West et al., 2022). An idealized DEM coupled to a realistic model of the ocean showed that surface eddies can govern both the motion and melt rate of individual floes (Gupta & Thompson, 2022a), and enhance lateral melt enough to affect the largest floe sizes (1–50 km, (Horvat et al., 2016)).

Sea Ice Sheet Modeling

Sea ice fracture is a complex process depending on heterogeneous material properties and highly variable mechanical and thermal forcings acting on floes and sheets both at micro (Cole, 2001; Sammonds et al., 2017) and macro (King et al., 2018) scales. Internal structure of sea ice is subject to multiple uncertainties such as brine content, welding of older floes, damage accumulation, snow deposition, melt pond formation (Polashenski et al., 2012) and other aspects that induce defects through cracks that can nucleate and propagate. Ocean, wind, and inter-floe collisions are very difficult to predict and are coupled to each other in space and time. Beyond their interactions, these forcings can combine with melt and freezing events that modify geometric and material properties, further developing internal defects or healing damaged ice. Current numerical sea ice models are still limited in reproducing this behavior accurately and introduce several simplifications in material and geometric conditions. Hence, it is a significant challenge to replicate sea ice fracture as observed in the field and satellite observations (Rheinlænder et al., 2022). Nonetheless, fracture is a critical process in the transition of the Marginal Ice Zone (MIZ) and intact sheets into lower sea ice concentration regimes. Floes and sheets of fast ice of several kilometers in diameters can only be removed from the ocean at observed rates in several regions, like Beaufort Sea (Moore et al., 2022), Kara Sea (Astakhov, 1998) or Baffin Bay (Moncada, Gupta, Thompson, & Andrade, 2023b), among many others, if they break and provide warm waters more surface area to amplify melt. Prediction of sea ice complete loss during the summer and the onset of landfast sheet initial breakage in the winter to spring transition, requires a better understanding of sea ice fracture.

Simulating sea ice fracture in landfast sheets is particularly challenging due to the need to represent uncertain sea ice material properties and the multiple external forcings sea ice is subjected to. Sea ice is an heterogeneous material that forms by freezing at the surface of bodies of water, starting as agglomerations of thin pancake ice. These pancake ice gradually starts welding together into larger floes and eventually into a sheet as fast ice, as mentioned above. For ocean water this freezing process results in the formation of brine (salt water) pockets that introduce additional complexity to the already porous material that is columnar ice (Crabeck et al., 2019; Oggier & Eicken, 2022). When floes combine, they also develop weaker joints that can lead to defects which can manifest later, and are often difficult to identify unless the floe becomes very thin and its snow cover has been removed (Smith et al., 2023). Ice thickness also can be heterogeneous, as a floe can become thicker due to snowfall, but also weaken by the formation of melt ponds due to higher atmospheric temperature, rainfall or solar radiation. These melt ponds can create preferential surfaces along which fractures can develop, regardless of bulk material properties (Diamond et al., 2021). Therefore, it can become very difficult to predict, even for very idealized loading and isothermal conditions, where and when a block of sea ice will break.

On top of the material complexity, several external agents affect sea ice. Intricate atmospheric winds and ocean currents can exert irregular stress regimes through form and skin fluid drag forces (Kwok et al., 2013; Q. Wang et al., 2021). Ocean waves can exert forces that result in bending failures depending on the floe size and thickness, wave height and wavelength (Boutin et al., 2021; Montiel & Squire, 2017). Floe collisions can induce damage both in the bulk and boundaries, as well as more quasi-static inter-floe pressure that can break due to shear and compressional loading (Damsgaard et al., 2021; Lu et al., 2015). Sea ice thickness reduction due to melt can accentuate stress concentrations and lead to a critical thickness threshold for which the floe is unable to sustain any significant loads (Lilja et al., 2021). Differences in thermal gradient for sufficiently thick ice and strong ocean and atmospheric temperature gradient can result in thermal stress that break floes (Bažant, 1992). If we then couple the interaction of the ocean, atmosphere and sea ice system and consider how uncertain and how scarce is some of this information we arrive to a formidable task when executing models to reproduce sea ice fracture.

For numerical simulation of sea ice breakage, properties such as Young's Modulus, critical fracture release energy, fracture toughness and Poisson's modulus have been used for idealized linear elastic fracture mechanic (LEFM) conditions, for specimens such as rectangle or beam with a pre-existing notch or the Brazil-nut test. Different continuum and discrete methods (cohesive models) have been used to simulate sea ice fracture under these idealized LEFM cases or similar conditions (Bateman et al., 2019; Dempsey et al., 1999; Dempsey et al., 2018; Egger et al., 2019; Makarov & Bekker, 2021; Mulmule & Dempsey, 2000). These applications prove it is possible to study sea ice breakage through LEFM continuum methods, as long as its cross-section and properties are homogeneous.

However, for breakage of fast ice where the location of defects and the distribution of thickness is often uncertain, the use of continuum damage models appears to be a more appropriate tool to handle an ice mass that breaks at regions of stress concentration. For example, this has also been used for calving and hydrofracture in other types of ice, such as glaciers (Clayton et al., 2022; Sun et al., 2021). Sea ice continuum methods have used both elasto-brittle (Plante & Tremblay, 2021), visco-elastic (Dansereau et al., 2017) and visco-plastic (Panteleev et al., 2020) damage models via phase field fracture mechanics to identify the formation and propagation of fracture in sea ice without using pre-existing defects (Dinh et al., 2022). Those methods have considered a uniform thickness and idealized geometries and loading conditions. If upscaled to continental regimes, continuum models parameterize sea ice concentration and thickness.

While continuum methods represent sea ice considerably well for scales of several hundreds of kilometers to larger scales, below the 100 km resolution, localized sea ice properties start affecting bulk behavior. Floe size distribution, floe shape, aspect ratio and surface area to volume ratio start playing a more relevant role which is not sufficiently captured with continuum analysis (West et al., 2021). Individual floe size affects response of sea ice with respect to waves, ocean drag, albedo, pack rheology and drift. More uniform sea ice is susceptible to faster melt and has a different internal stress distribution than well-graded sea ice mosaics (Horvat et al., 2016; Moncada, Gupta, Thompson, & Andrade, 2023b). As a result, methods that deal with floes as individual or distinct entities have gained more traction in the last decade. They can help explain individual, floe pack and sheet fracture development.

Discrete element methods have been the most used methodology for analyzing individual floes and the transition of an intact or pre-damage ice sheet into multiple floes. Some implementations of this methods are explained next.

One of the earliest applications of DEM for landfast ice was from Zyryanov and Korsnes (2003) compiled in (Konietzky, 2017) using Particle Flow Code (PCF^{2D}) with bonded circular disk for an area in Kara Sea. Increase in wind stress magnitude was found to be correlated with the decrease in fast ice area. Their results showed a significant sensitivity to the direction of currents, which impact how well the behavior shown in observations is reproduced. Nonetheless, the earliest application of (Cundall & Strack, 1979a) to individual floe DEM simulations can be found in (Løset, 1994). More recently (Bateman et al., 2019; Herman, 2011, 2013, 2017) developed a DEM with circular disks subject to body and skin drag from the ocean and atmosphere, used to replicate distinct floe fields and sea ice as a sheet. In several applications of this model, disks were bonded to replicate the cohesive characteristics of sea ice and its breakage. Transversal wave effects with an off-plane bending moment component was used to analyze sea ice breakage, including particular wave height and wavelength regimes favoring fracture.

Similar to the methodology of prior papers, West et al., 2021 and Turner et al., 2022 have developed ParticLS DEM, which uses a Bonded Particle Method with information from wind currents and a geometry based on satellite data to develop ice fracture at the free edge, and then keep track of floe sizes. DEMSI can use both disk and level set-based polygonal elements with bonded discrete element method and utilize a non-local criterion for bond breakage and Mohr-Coulomb material modeling. The method was applied to an initial monolithic sheet of ice trapped within an idealized channel and then to a similar regime based on MODIS images from Nares strait. Their model allowed exploring the development of failure, arching, stress and strains, mass loss and floe sizes as a result of forcings in constrained sea ice. Bond cohesion was found to be inversely proportional to mass loss and number of floes generated by failure and geophysical data was used to calibrate material parameters. Sea ice arching and stress concentrations observed using satellite data were qualitatively reproduced, showing the potential of BPM-DEM in replicating sea ice stress FSD and fracture behavior. Examples of DEM models for fast ice are shown in Figure 1.10.

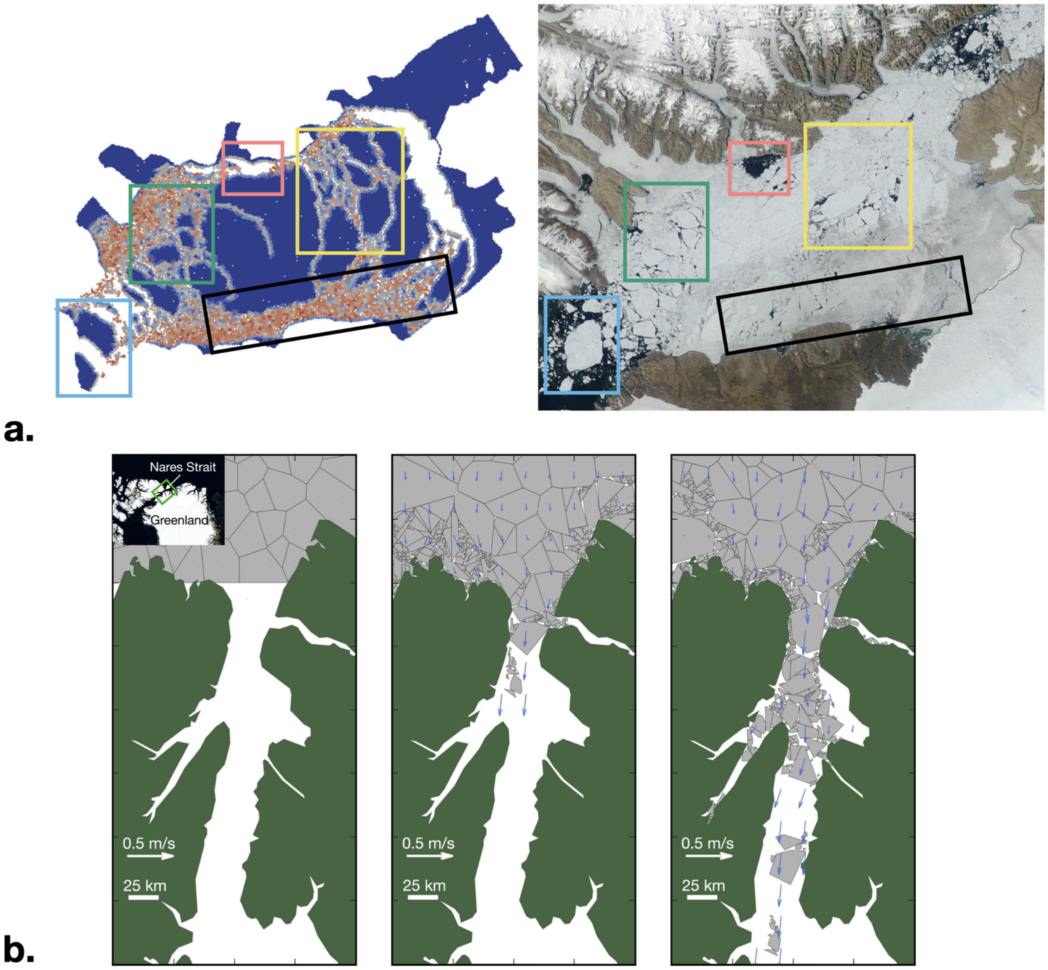

Figure 1.10: Examples of ice sheet discrete element models: a. DEMSI-BPM at the southern end of Nares Strait, compared to satellite data (West et al., 2022), and b. SubZero polygonal DEM simulating an ice sheet being pushed through the north of Nares Strait. (Manucharyan & Montemuro, 2022).

For approaches expanding on the bonded particle method, Lilja et al., 2021 developed a three-dimensional Finite-Discrete Element method for sea ice sheets. Finite elements were used for bonds, modeled as Timoshenko beams, with off-plane components, with polygonal discrete elements with evolving damage. Using this approach, uni-axial tensile failure, vertical penetration and interaction with structure were simulated for ice sheets. Manucharyan and Montemuro, 2022 modeled the marginal ice zone (MIZ) and an ice sheet in both periodic boundary conditions and pushed through the Nares strait geometry using SubZero. Rather than applying a bonded particle method to replicate fracture, SubZero applies a tessellation-based fracture method. Its DEM objects can change shape, assume non-convex geometries and reproduce melt, freezing, welding, grinding, rafting and ridging processes. Particularly for fracture, floes above a certain threshold can split into smaller ones, using homogenized floe stress obtained from contact data via a Mohr-Coulomb failure criterion. Then Voronoi tessellation defines fracture geometry using random coordinates. Evolution of fracture and floe size distribution has been qualitatively representative of sea ice.

A different alternative for distinct floe breakage was used by Moncada, Gupta, Thompson, and Andrade, 2023a to reproduce sea ice concentration changes in floes in the marginal ice zone. Realistic-shaped floes based on satellite data were create using the LS-ICE method, which uses level sets for contact detection of irregular objects. These distinct element also have the ability to change shape due to breakage and melt events. LS-ICE was able to replicate concentration changes parameterizing breakage frequency and melt rate. Breakage, nonetheless, was based on random occurrences rather than external ocean, wind or wave forcings. Even with just an approximation of fracture rate, this coupling of breakage and melt was shown to control the rate of sea ice reduction and this synergy cannot be ignored. Another relevant aspect, was the application of the melt rate to update sea ice thickness over time, which has been shown to be critical for breakage, via a critical value (Bateson et al., 2022; Ford et al., 2021).

1.5 Research Opportunities for LS-DEM, LS-ICE and BPM

For this work we want to emphasize several novel aspects not yet fully explored:

1. So far only polygonal, disk or disk-cluster-based sea ice floes DEM has been simulated. However, with LS-DEM we can directly convert satellite images into unique arbitrary shapes, that can be compared more directly with their physical equivalents in the observations. Factor such as kinematics, contacts, surface area and breakage are all affected by particle shape (Kawamoto et al., 2018). Therefore, we would expect using more realistic shapes to represent the system with better accuracy with LS-ICE. This is also directly tied to the evolution of the FSD.

2. At the same time, since we are using level sets to store shape information,

we can also use temperature ODEs to handle the evolution of level sets via changes in temperature with respect to the melting point. Sea ice kinematics will be affected as ice loses mass through basal, surface and lateral melt. This combination of melt and break processes have not been applied for arbitrary shapes as the ones presented.

3. By controlling basal and surface melt with respect to ocean temperature diffusion, spatial distribution of thickness can also be obtained for floes, rather than a single value for the whole block of sea ice. This will offer more specific information for sea ice fracture. More importantly, for sea ice sheets, being able to manipulate thickness through spatially variable melt will result in the formation of weak area that can trigger fracture at only certain parts of the sheet.

4. By dealing with floes at an individual level, we can fully extract all melt and breakage statistic, including mass and number of floe exchange for a FSD set of bins. This will allows us to explore the relative melt to breakage dominance, the main source of melt and even a threshold size for which melt and breakage, respectively, have a stronger impact on sea ice floes.

5. So far most of the sea ice sheet modeling has not applied ocean currents with arbitrary and realistic eddying regimes, instead only simple and idealized wind forcing. Here we propose to introduce ocean currents from a comprehensive 3D oceanographic model that includes temperature, salinity, ocean mixed layer variations, Coriolis forces, etc. and use them as forcing fields to induce fracture in fast ice. The resulting breakage development and FSD characteristic of these ocean currents can then be found.

6. Part of the simulation philosophy is the necessity to compare our results with experiments. While full scale sea ice experimental data is unavailable, we want to focus on using satellite data as a replacement. Fortunately, MODIS images have a daily temporal resolution, which facilitates the observation and comparison of simulations that have significant evolution of their properties. In other words, we want to use remote sensing as a means to aid computational mechanics simulations in a granular material.

7. As using a full finite element-discrete element method might be computationally prohibitive for large scale models, we propose dealing with breakage by using a bonded particle method combined with LS-DEM (LS-DEM-BPM).

Hence, we can couple bond strength with temperature, thickness changes, ocean currents, ice-ocean momentum damping and damage if required.

8. With all of these opportunities well-explored, the idea is to achieve better sea ice modeling and, ultimately, enhanced sea ice predictions in properties, concentration and floe size distribution.

1.6 Structure of the Thesis

Our thesis will emphasize the dissolution of sea ice mosaics, during the spring to summer transition and will not dwell on the fall to winter recovery or overall winter conditions. Chapters 2 and 3 of this work will focus on the MIZ distinct floe to open ocean transitions, as it is here where DEM is the most advantageous and FSD has drastic changes that are insightful to record.

Chapter 2 will present the development of the LS-ICE method based on LS-DEM. Its main mechanical and full thermodynamic formulation will be described. Considerations for floe representation into coarse (DEM objects) and fines (average quantity) and use of re-analysis data and satellite images as initial and forcing conditions will be explained. Then, the model will be validated and results for its application on concentration decline will be evaluated.

Once the tool for floe systems is set up and its reliability showcased, Chapter 3 will use LS-ICE for FSD analysis, attempting to go beyond the widely used average-based methods. Sensitivity analysis conditions will be established and concentration, mass and FSD metrics will be introduced. These metrics will be used to measure the relative dominance or contribution of melt and breakage processes, for a couple of sample years. With a high level of detail of FSD bin exchanges, we will even uncover the relationship between lateral and vertical melt.

For Chapter 4 we will travel back in time, or towards inland, to the decay of sea ice from a fully solid, intact landfast sheet into a mosaic of distinct floes at the MIZ, essentially ending on the initial conditions of Chapter 2 and 3 or even progressing to the open ocean regime altogether. For this, we switch from LS-ICE to a more conventional LS-DEM-BPM using bonded disks for efficiency, but using satellite images for initialization and evaluation of fast ice area reduction and FSD changes. A study of the properties of horizontal ocean currents is presented, assessing the effects of wavelength and wave propagation speed of simple pulses and how this can result in different FSD and overall breakage. Finally, these findings are extended to arbitrary eddying regimes that especially highlight the impact of ocean current wavelength. Chapter 5 will contain the main conclusions of this thesis and present future potential work that can be expanded on.

Chapter 2

LEVEL DISCRETE ELEMENT METHOD FOR SEA ICE: LS-ICE

Moncada, R., Gupta, M., Thompson, A., & Andrade, J. (2023a). Level set discrete element method for modeling sea ice floes. *Computer Methods in Applied Mechanics and Engineering*, *406*, 115891. https://doi.org/10.1016/j.cma.2023.115891

2.1 Outline

In this chapter we introduce a new DEM-based model of sea-ice, named 'Level Set Discrete Element Method for Sea Ice' (LS-ICE) that leverages the 'Level Set Discrete Element Method' (LS-DEM) borrowed from the field of granular and solid mechanics to model stress interactions between discrete grains, and predict localized failure in granular materials without the use of plasticity continuum constitutive models (Kawamoto et al., 2016, 2018). We have adapted the model to represent sea ice floes of arbitrary shapes using level set functions, which define the boundary of a floe and can be used to efficiently detect contact between floes. The floes are allowed to break into smaller convex or non-convex shapes, and carry resolved information such as thickness, damage due to collisions and temperature, on a localized grid. The model is also capable of computing internal stresses within floes and severing the ice floe according to specified breakage criteria (Harmon et al., 2020).

For LS-ICE we couple LS-DEM with an ocean thermodynamic model, to test the sea ice model's behavior in summer Arctic-like conditions. This involves the evolution of a relatively packed field of sea ice floes (~ 80 % concentration) into a domain almost devoid of ice, within 1-2 months. This represents a set of conditions that have not been tackled by previous DEMs, which have tended to focus on more highly concentrated and monolithic sea ice regions. Capturing this summer melt transition involves an appropriate representation of feedback between ocean temperature, surface albedo, sea ice breakage and melt. We validate our model's behavior by using a sequence of co-located satellite imagery from the NASA Moderate Resolution Imaging Spectroradiometer (MODIS) dataset during June-August in Baffin Bay, to the west of Greenland (Figure 2.1). By tuning only a small number of parameters related to sea ice melt and breakage, we find that the model can reproduce statistical bulk sea ice properties from field data, like the evolution of sea ice concentration, mean thickness, floe size distribution and surface ocean temperature.

The chapter is structured as follows: Section 2.2 presents the LS-ICE model, including the initialization of floe shapes from satellite imagery, floe dynamics and breakage, and thermal interactions with with a simple ocean model. Section 2.3 presents the satellite images and reanalysis datasets used to configure and validate the model, parameter tuning and performance metrics. Section 2.4 shows the results for a representative case study used to benchmark the model, and Section 2.5 concludes with a discussion and final remarks.

2.2 Model Formulation

LS-ICE: LS-DEM for sea ice

The Level Set Discrete Element Method is an approach that uses level set functions (Kawamoto et al., 2016; Osher & Fedkiw, 2001), along with the geometrical information from arbitrarily-shaped objects, to efficiently detect contact between different objects. Level set functions measure the signed distance from the interface (or boundary) of a given object to any other point in space, such that zero values define the border of the object, negative values are inner points, and positive values are points outside of the object (See Figure 2.1). These level set functions can be defined exactly from analytical expressions, though in this study they are approximated onto a discrete grid. The level set method allows the representation of precise, non-convex, irregular and arbitrary geometries, rather than the disks or polygons otherwise commonly used for sea-ice DEMs. The level set representation also allows an easy implementation of flexible boundaries that can expand, contract, morph or break in response to external forcings.

We applied a procedure for contact detection and calculation of inter-granular forces for a single contact that is explained in detail in (Kawamoto et al., 2016), and briefly summarized here. We consider the contact forces arising on a 'leader' floe, due to its contact with a 'follower' floe. We discretize the leader floe's boundary with a finite number of points (white dots in the level set boundary of Figure 2.1), which we refer to as a floe's point list. To determine contact, we find the intersection of the leader's point list with the follower's level set function ϕ, stored as a uniform 2D grid. We seek for an overlap of every point $\mathbf{p}$ of the leader floe to determine the resultant forces and moments of floe kinematics. For the force calculation, we first find penetration distance and contact normal by determining the value of the level set function $\phi(\mathbf{p})$ and its gradient $\nabla\phi(\mathbf{p})$, at every point $\mathbf{p}$. Given a point at arbitrary coordinates $x = a$ and $y = b$, we define $\phi(\mathbf{p}_{ab}) = \phi_{ab}$. The level set value $\phi(\mathbf{p})$ and its gradient $\nabla\phi(\mathbf{p})$ are then given by:

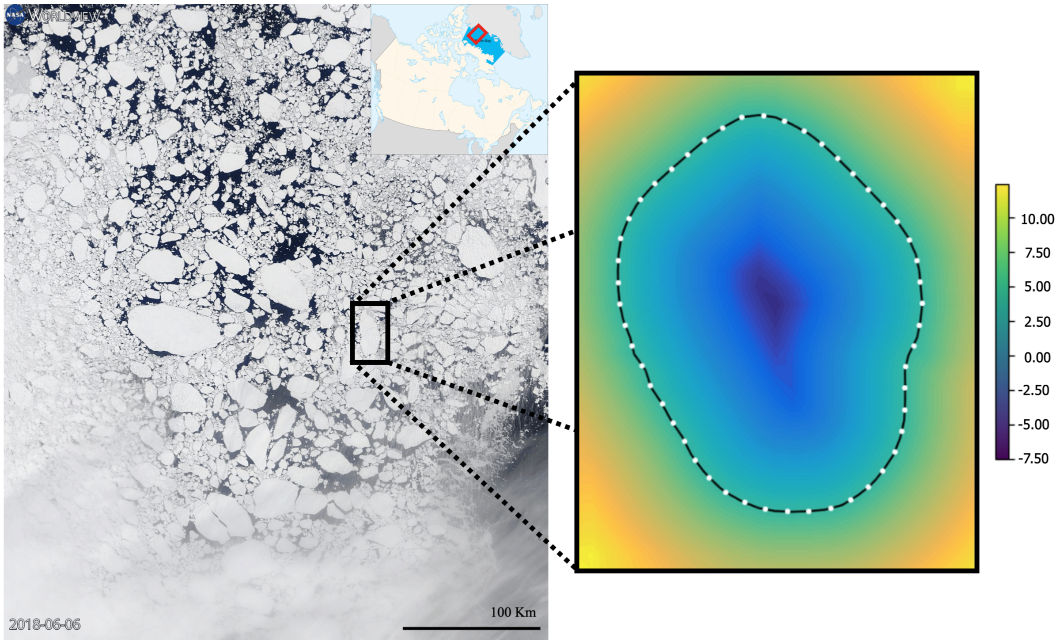

Figure 2.1: MODIS Image Example of Baffin Bay on June 6, 2018, which contains the domain used for the main case analyzed in this work. Reference distance for scale is included at the bottom right corner and location of domain is defined in the upper right corner red box. Floes from the MODIS image can be processed into level sets as the example shown with its boundary points. The floe boundary is defined as the zero level set value (shown in the black line) while the points (in white) represent the discretization of the boundary used for contact detection. Cells inside the floe have negative values and cells outside have positive values.

$$\phi(\mathbf{p}) = \sum_{a=0}^{1}\sum_{b=0}^{1} \phi_{ab}[(1-a)(1-x)+ax][(1-b)(1-y)+by] \tag{2.1}$$

$$\nabla\phi(\mathbf{p}) = \left(\sum_{a=0}^{1}\sum_{b=0}^{1} \phi_{ab}(2a-1)[(1-b)(1-y)+by], \sum_{a=0}^{1}\sum_{b=0}^{1} \phi_{ab}[(1-a)(1-x)+ax](2b-1)\right). \tag{2.2}$$

Using Eq. (2.1) and Eq. (2.2) we obtain the penetration distance of the point $\mathbf{m}_a^i$ of floe i on the level set of floe j :

$$d_a^{j,i} = \phi^j(\mathbf{m}_a^i). \tag{2.3}$$

The contact normal vector is given by:

$$\hat{\mathbf{n}}_a^{j,i} = \frac{\nabla \phi^j(\mathbf{m}_a^i)}{||\nabla \phi^j(\mathbf{m}_a^i)||}, \tag{2.4}$$

where $d_a^{j,i}$ is the contact penetration distance, $\hat{\mathbf{n}}_a^{j,i}$ is the outward contact normal between floes "i" and "j" and $\mathbf{m}_a^i$ is the contact node (see Figure 2.2) from floe i, with a being a particular node from the total of number of A nodes in this floe's point list. Using the results of Eq. (2.3) and Eq. (2.4) we obtain the normal contact forces, the action force on the follower and the reaction force on the leader, as follows:

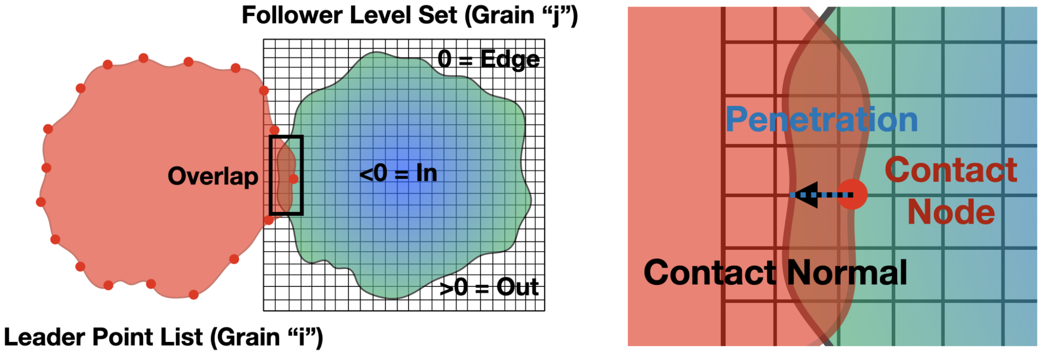

a.

b.

Figure 2.2: Schematic illustrating the penetration distance and contact normal between a leader and follower floe pair overlapping over a region containing a single point. a. The leader point list must overlap negative level set values of the follower floe for the objects to be considered in contact with each other. b. Detail of where the penetration distance and contact normal are calculated with respect to the floe overlap.

$$\mathbf{F}_{n,a}^i = -k_n d_a^{j,i} \hat{\mathbf{n}}_a^{j,i} \tag{2.5}$$

$$\mathbf{F}_{n,a}^j = -\mathbf{F}_{n,a}^i, \tag{2.6}$$

where $\mathbf{F}_{n,a}^i$ is the normal contact force exerted on the leader, $\mathbf{F}_{n,a}^j$ is the contact force on the follower (if penetration is positive or zero, forces are considered zero) and k_n is normal contact stiffness. Similarly, shear forces $\mathbf{F}_{s,a}^i$ and $\mathbf{F}_{s,a}^j$ are obtained using a Coulomb friction model with a slip scheme (friction only, no cohesion) described also in (Kawamoto et al., 2016), where relative grain velocity between leader and follower is used to find incremental shear displacements and slippage.

The calculation of normal and shear forces is repeated for all points of the leader in contact with the follower, adding up the net forces and moments for each floe contact pair. The total force acting on a floe is calculated as follows:

$$\mathbf{F}^{i}_{tot} = \sum_{a=1}^{A_c} \left(\mathbf{F}^{i}_{n,a} + \mathbf{F}^{i}_{s,a}\right) \tag{2.7}$$

$$\mathbf{F}^{j}_{tot} = -\mathbf{F}^{i}_{tot}, \tag{2.8}$$

where A_c is the total number of intersecting contact nodes between floes i and j.

The moments (or torques) are then obtained from:

$$\mathbf{M}^{i}_{tot} = \sum_{a=1}^{A_c} \left((\mathbf{m}^{i}_{a} - \mathbf{c}^{i}) \times \mathbf{F}^{i}_{n,a} + (\mathbf{m}^{i}_{a} - \mathbf{c}^{i}) \times \mathbf{F}^{i}_{s,a}\right) \tag{2.9}$$

$$\mathbf{M}^{j}_{tot} = \sum_{a=1}^{A_c} \left((\mathbf{m}^{i}_{a} - \mathbf{c}^{j}) \times \mathbf{F}^{j}_{n,a} + (\mathbf{m}^{i}_{a} - \mathbf{c}^{j}) \times \mathbf{F}^{j}_{s,a}\right), \tag{2.10}$$

where $\mathbf{c}_i$ and $\mathbf{c}_j$ are the centroids of both floes. Subsequently, more forces and moments can be accumulated on a floe from additional contacts with other floes. In this approach, both leader and follower floes are assumed to be perfectly rigid when calculating contact. The numerical scheme calculates contact between each floe "i," defined as a leader, and floes "$i + 1$" to "N_{floes}," evaluated as potential followers (Kawamoto et al., 2016, 2018). After the contact detection and force calculation is completed for all floes, the DEM contact model is time stepped forward (see Section 2.2).

Floe shape extraction and oceanic momentum forcing from satellite imagery

To extract realistic shapes for the LS-ICE floe model, we use a sequence of images from the visible spectrum, obtained from the NASA MODIS dataset (see Section 2.3). We process the images to identify individual floes using the a segmentation method similar to that detailed in (Lopez-Acosta et al., 2019), as illustrated in Figure 2.3. The image is first binarized into sea ice and ocean, from which the total sea ice concentration is defined. For setting up the binary image, gray-scale brightness values from 155 to 255 are used to define sea ice pixels. These pixels have a spatial resolution between 750 m to 1 km, depending on the image selected. To identify individual floes, we perform image segmentation using the erode, dilation, watershed and labeling functions from the Python scikit-image package (Van der Walt et al., 2014). Images are further processed with additional watershed functions to generate a group of level set objects, with grid resolution obtained from the labeled image (Vlahinić et al., 2016). A higher image resolution results in finer, but more memory-intensive, level sets and better resolved floes.

We define resolved objects as 'coarse' floes that are explicitly modelled as level set objects. The remaining sea ice is instead modelled statistically, and defined as 'fine' floes. The threshold length scale for this coarse to fine floe transition is set at 2 km, which is close to the MODIS image pixel resolution. Resolved (coarse) objects from the first image in the sequence are used to generate the initial geometry of the LS-ICE simulation (see Figure 2.3), while the remainder of the sequences is used to validate the simulation results, with respect to the evolution of coarse and fine sea ice concentration, as well as floe size distribution.

From satellite data, we also infer an ocean momentum forcing that acts to displace and collide the sea-ice floes. In the absence of ocean current data at sufficient spatial resolution, we simply aim to reproduce the motion of the mean centroid position averaged over all the resolved floes. The momentum coupling is one-way, from ocean to floes, such that the ice does not affect the ocean velocity. Inspired by (Lopez-Acosta et al., 2019), we estimate the mean centroid velocity $\mathbf{V}_{ave_k}$ at time k from the displacement of the mean centroid position between each satellite image. We then calculate a reference force magnitude $\bar{F}_{ref}$, based on the first two values of $\mathbf{V}_{ave_k}$, as follows:

$$\bar{F}_{ref} = m_{LF} * \frac{\bar{V}_{ave_2} - \bar{V}_{ave_1}}{\Delta t}, \tag{2.11}$$

where m_{LF} is the mass of the largest floe, $\bar{V}_{ave_2}$ and $\bar{V}_{ave_1}$ are the final and initial average centroid speeds, respectively, and Δt is the time elapsed between snapshots 1 and 2. At each time step k, the force applied to the floes $\mathbf{F}_{ocean_k}$ is obtained by scaling $\bar{F}_{ref}$ by the quotient of the magnitude of the current velocity ($\bar{V}_{ave_k}$) and the average of all centroid velocity magnitudes ($\bar{V}_{ave_M}$), with a direction θ_k that comes from the change in velocity angle with respect to the prior snapshot:

$$\mathbf{F}_{ocean_k} = \bar{F}_{ref} * \frac{\bar{V}_{ave_k}}{\bar{V}_{ave_M}}(\cos(\theta_k), \sin(\theta_k)). \tag{2.12}$$

This force emulates oceanic currents and induces reasonable floe velocities without explicitly modeling fluid kinematics. The forcing is applied uniformly over the domain, such that all the floes are forced in the same direction. However, differences in floe mass lead to different velocity magnitudes between floes, inducing collisions that affect floe trajectories and may also induce floe rotation. The boundary conditions for floe motion are doubly-periodic, such that no ice is lost at the boundaries. This tends to reflect the conditions in the selected validation region over Baffin Bay, where most of the resolved floes remain within the domain during the time period of interest. The motion of floes generally helps them access warmer waters and facilitates their melt, as the ocean tends to be colder underneath the ice, which has a high albedo and insulates underlying waters from solar heating (Gupta & Thompson, 2022b).

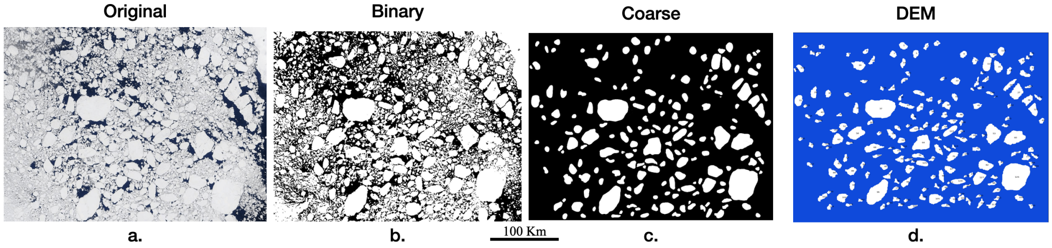

Figure 2.3: Procedure employed for processing the satellite images used to initialize the LS-ICE. a. Original RGB image, b. Binary image separating sea ice and ocean pixels, c. Coarse Grain Segmentation and d. LS-ICE Discrete Element Generation. Example region analyzed between 78.1°W and 61.2°W and 67.9°N and 80.1°N for June 4, 2020 (first day of the simulation for 2020)

.

Floe breakage

Sea ice floes often undergo breakage, due to floe-floe collisions, wave-induced flexural stresses, or shear due to ocean currents and atmospheric winds (Boutin et al., 2020; Dempsey et al., 1994; Herman, 2018). Existing theory cannot account for all these different breakage mechanisms, particularly in the marginal ice zone. For simplicity, we therefore represent breakage as a random stochastic process, which uniquely depends on a parameter dubbed the ‘breakage frequency’ B. Future model development will attempt to develop more physically-based breakage criteria.

At each time instant $1/B$, we break a single random coarse floe into two pieces. We select a breakage point within this floe, defined as a random distance in the X and Y directions, from the floe centroid up to 80 % of its mean caliper radius.

If the breakage point falls outside the floe, which is not uncommon for elongated floes, the process is repeated until the breakage point is chosen within its bounds. The object is then split by a straight line extending from the breakage point with a random angular direction. The two points at the intersection of this breakage line and the floe borders are defined as the split points, where the floe is separated as two new objects (see Figure 2.4). This straight line split is repeated at the breakage frequency B and may occur for any resolved floe.

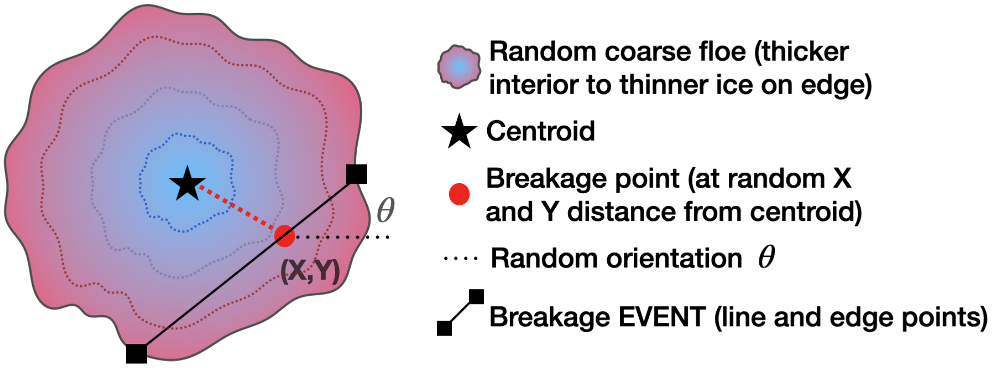

Figure 2.4: Schematic of breakage event, as implemented in the LS-ICE model. A random point is chosen inside the coarse floe (red dot), along with a random angle θ, which defined the breakage line (black line). This breakage line splits the floe into two pieces, conserving the total mass of ice, as well as the thickness distributions over each of the pieces (blue for thicker ice and red for thinner ice). In our current implementation, these breakage events are constrained to occur at the breakage frequency B, for a single random floe at a time. The objective of the breakage parameter is to condense intra-floe stress uncertainty.

Interactions with ocean model: global and local grids

In this work, we implement a two-way thermal coupling and one-way mechanical coupling between sea ice floes and a highly-idealized ocean model, which supplies boundary conditions to the ice. The ocean is not affected in its kinematics by the overlaying ice floes. The ocean's temperature changes in response to sea ice melt and solar forcing are described in Section 2.2. The domain's ocean temperature is carried by a square 2D 'global' ocean grid of 400 km extent composed of square cells with 1 km resolution and double periodic boundary conditions. The 'global' grid represents the complete coordinate extent of the domain, in contrast to individual or local floe coordinates. To transfer properties (namely ocean temperature) from the ocean model to the ice floes, we use a 'local grid' for each ice floe, which contains quantities that may be modified by the oceanic forcing. These local grids have equal or finer resolution to the global grid (a few hundred to a few tens of meters), which varies according to the floe boundary's roughness, its shape and size; floes with more complex shapes have a more refined grid. In this work, we only carry the sea ice floe thickness on this local grid, though it is also possible to keep track of internal stress and strain fields, as well as cumulative damage to the ice, in order to implement more complex breakage criteria. Here, the floe thickness at each local grid point evolves according to the ocean temperature interpolated onto this local grid (section 2.2), using the nearest values from the global ocean grid (see Figure 2.5). This local grid framework allows LS-ICE the capability to force the motion of sea ice floes from arbitrary oceanic currents and atmospheric winds over time and space, by again interpolating these fields from a global grid to the local floe grid. However, for this work, the focus is on statistical sea ice changes due to melt and breakage so only a homogeneous oceanic forcing was implemented (Section 2.2).

Thermodynamic modeling

The thermodynamic model is largely based on summer sea ice melting dynamics described by (Thorndike, 1992) and (Gupta & Thompson, 2022b), where we assume that the sea ice remains at the freezing temperature at all times. This is equivalent to assuming that the vertical temperature profile within the ice is flat, which is characteristic of thin ice during the summer season. The heat provided by solar and atmospheric forcings is therefore entirely consumed by the ice as latent energy for melt.

When ice floats upon relatively warm ocean, it extracts heat from these waters, and in turn cools them down. The ocean model consists of a single slab layer with two-way thermodynamic coupling to the sea ice floes. The thickness of this slab represents the 'mixed layer' of the ocean, a surface layer that is typically 10–50 m deep, where properties are assumed to be well-mixed in the vertical direction due to fine scale turbulence, notably induced by winds. Here, these vertical mixing processes are not explicitly modelled, but are assumed to occur on faster time scales than horizontal mixing and transfer of properties below the mixed layer. We distinguish the thermodynamic melt treatment of coarse (resolved) versus fine (unresolved) floes. Coarse floes have an explicit location in space, and their thickness is evolved according to the local ocean temperature they encounter along their path. On the other hand, fine floes are assumed to be uniformly distributed among the global grid cells that are not occupied by the coarse floes. Below we detail the thermodynamic representation of both coarse and fine floes.

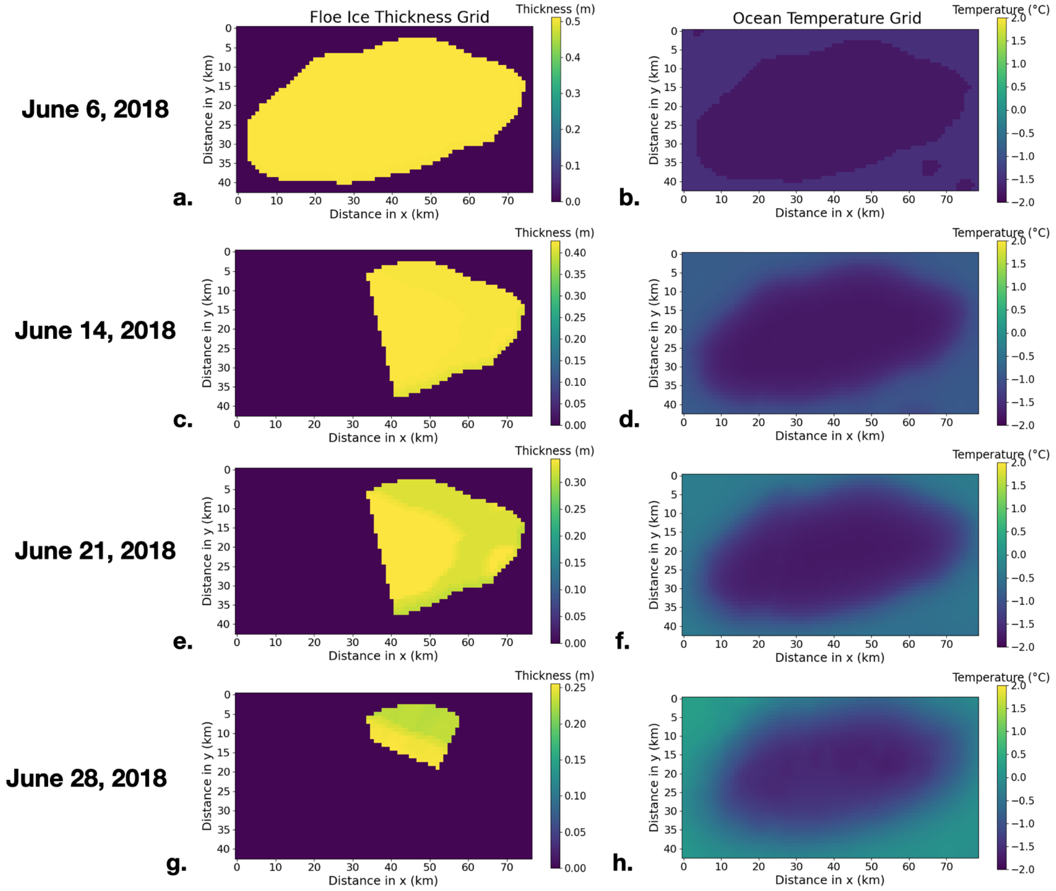

Figure 2.5: LS-ICE grid examples. a., c., e., and g. Floe thickness on local grid for a chosen floe. b., d., f., and h. Surface ocean temperature on local grid, interpolated from the global grid. Floe edges will tend to have a smaller thickness than the center of the floe (depending on breakage and kinematics), given the exposure of borders to higher temperatures that melt ice from the bottom at a faster rate. On the other hand, given ice albedo, water under floes tends to remain cooler than its surroundings. Solar-induced melt at the top of the floe is assumed to be uniform across the entire floe. June 6 is the first day of simulation for 2018.

Coarse Floes

The thickness distribution of a coarse floe is evolved according the following equation, as in (Gupta & Thompson, 2022b):

$$\rho_i L_f \frac{\partial h_c}{\partial t} = q_v(T_{melt} - T) - S(1 - a_i) + (A_s + B_s T_{melt}), \tag{2.13}$$

where $h_c = h_c(x, y, t)$ is the thickness of coarse floes defined on each cell of each local floe grid, and $T = T(x, y, t)$ is the ocean temperature defined on the global grid, and interpolated onto the floe grid (see Figure 2.5). The definition of constants employed in Eq. (2.13) are summarized in Table 2.1. The terms on the right hand side of Eq. (2.13) represent: heat from the underlying warm ocean, downwelling solar shortwave heat flux, and upwelling longwave heat flux. The effects of latent and sensible heat fluxes are subsumed into the longwave heat flux term.

The ocean temperature underlying coarse floes is evolved by:

$$\rho_0 c_p H \frac{\partial T}{\partial t} = \rho_0 c_p H k \nabla^2 T - q_v (T - T_{melt}), \tag{2.14}$$

where terms on the left of the expression are defined on Table 2.1. The first term on the right hand side of Eq. (2.14) represents the lateral diffusion of ocean heat with a constant diffusivity k, while the second term is vertical ocean and ice heat exchange. Ice is assumed to be entirely insulating to solar heat fluxes, such that there are no atmospheric heat flux terms in Eq. (2.14).

As illustrated in Figure 2.5 the insulating effect of sea ice, along with its higher albedo, tends to maintain colder temperatures underneath the floe. This effect is counteracted by the lateral diffusion of heat, which helps bring warmer waters in contact with the floe. The horizontal motion of sea ice floes also leads to floes encountering different temperatures, and generally encourages melt as floes are decoupled from their cold underlying water lens. The combined effect of these processes results in colder waters underneath the center of the floe, as compared to near its edges, resulting in floes that are generally thinner at their edges. When the thickness of these edge cells reaches zero, the shape of the floe is modified or shrinks through its level set function.

Moreover, the implementation of non-uniform melt may modify the thickness distribution within floes. For simplicity, we calculate the moment of inertia using the average floe thickness rather than taking account of individual thickness values on the local floe grid. This approximation does not significantly affect floe rotation rates, since the non-uniformities in thickness are only on the order of 15–20%.

Fine floes

Fine floes represent the concentration of ice that could not be modeled explicitly with the level set method, due to its sub-grid scale. We assume that these fine floes only interact thermodynamically with the underlying ocean, and that they they do not exchange any momentum with the coarse floes. This may be justified for summer melt conditions, where low concentration and finely broken up sea ice is typically

Table 2.1: Thermodynamic Model Constants and Parameters

Variable	**Meaning**	**Value**	**Units**
CONSTANTS:			
ρ_o	Ocean density	1030	kg m^{-3}
c_p	Ocean specific heat capacity	3991	J kg^{-1} °C^{-1}
H	Mixed layer depth	25	m
k	Ocean horizontal diffusivity	20	m^{2} s^{-1}
a_i	Ice albedo	0.7	None
a_o	Ocean albedo	0.3	None
A_s	Atmospheric heat flux linear term	70	W m^{-2}
B_s	Atmospheric heat flux linear term (slope)	10	W m^{-2} °C^{-1}
T_{melt}	Fusion temperature of sea ice	-1.8	°C^{-1}
n_{cells}	Total number of cells in domain	160,000	None
A_{cell}	Area of global temperature grid cell	1	km^{2}
A_T	Total area of domain	160,000	km^{2}
ρ_i	Ice density	910	kg m^{-3}
L_f	Latent fusion heat of ice	330,000	J kg^{-1}
PARAMETERS:			
S	Solar shortwave heat flux	240 – 320	W m^{-2}
q_v	Rate of vertical ice melt	5 – 45	W m^{-2} °C^{-1}
B	Breakage Frequency	1.44 – 18	h^{-1}

thought of just being advected as a surface tracer, closely following ocean currents (Fenty & Heimbach, 2013). We further assume that the fine floe concentration is uniformly distributed over all global grid cells that are not occupied by the coarse floes. This ensures the conservation of total sea ice mass, without having to track an explicit tracer across the domain. Future work may involve mechanical contact laws between resolved and subgrid floes.

Fine floes are assumed to undergo basal melt, according to the mean underlying ocean temperature of the entire domain. This implicitly assumes that temperature is well-mixed at the subgrid scale, and allows these fine floes to be in contact with relatively warm, open-ocean temperatures at all times.

We represent the concentration of fine floes as a binned distribution or matrix, where each bin or element of the matrix represents an amount of sea ice area, with a thickness that varies in time due to melt (see Figure 2.6). The concentration of fine floes c_f within all open ocean cells (i.e., not covered by coarse floes) is given by:

$$c_f = \frac{\sum_{i=1}^{n_f} A_{fi}}{n_f A_{cell}}, \tag{2.15}$$

where n_f is the number of bins or elements, A_{fi} is the fine floe sea ice area associated with an element i, n_f is the total number of open-ocean cells, and A_{cell} is the grid cell area.

The global net albedo within open-ocean cells is assumed to be a weighted average between the ice and ocean albedos, regulated by the global fine concentration c_f:

$$a_{net} = c_f a_i + a_o(1 - c_f). \tag{2.16}$$

Similarly, the net ocean surface temperature T_{net} of a specific global ocean cell, used for outgoing longwave radiation, is also assumed to be linearly weighted between sea ice melting point and the ocean temperature:

$$T_{net} = c_f T_{melt} + T(1 - c_f). \tag{2.17}$$

The ice thickness of each fine floe element h_f evolves according to the following equation:

$$\rho_i L_f \frac{\partial h_f}{\partial t} = q_v(T_{melt} - \overline{T}_f) - S(1 - a_{net}) + (A_s + B_s \overline{T}_{net}), \tag{2.18}$$

where $\overline{T}_f$ is the ocean temperature T averaged over n_f open ocean grid cells and $\overline{T}_{net}$ is the average of T_{net} values over all n_f cells. Fine floe thickness evolution only depends on spatially-averaged values since the location of fine floes is not tracked.

The equation evolving for ocean temperature within open ocean cells is given by:

$$\rho_0 c_p H \frac{\partial T}{\partial t} = \rho_0 c_p H k \nabla^2 T + S\,(1 - a_{net}) - (A_s + B_s T_{net}) - q_v(\overline{T}_f - T_{melt}). \tag{2.19}$$

Unlike the case corresponding to ocean grid cells underneath coarse floes (Eq. (2.14)), open ocean cells receive the effect of atmospheric radiative fluxes and account for the net fraction of fine floes through a_{net} and T_{net}.

Fine floes are handled as a matrix that tracks area and thickness. The initial concentration of fine floes is split into 100 elements with equal area and a Gaussian distribution in thickness, such that the mean initial thickness matches the observed value from reanalysis data averaged over the domain (green bars in Figure 2.6). This initial distribution has a standard deviation and a minimum thickness of 0.1 m. As the simulation progresses, thickness of fine floes decreases due to melt from ocean and atmosphere heating. When thickness of a given element reaches zero, it is removed, which leads to a reduction in fine floe concentration equal to that element's area. Additionally, as coarse floes break or decay into pieces that are too small to track, their concentration and thickness are added as new elements to the fine floes matrix (red bars in Figure 2.6), such that the total sea ice mass is conserved during breakage processes.

Simulation time-stepping and looping

After the initial setup, the simulation time stepping is initiated (Figure 2.7), looping over the main features of the model: force update, thickness and geometry update, breakage, melt, temperature update and kinematics. We use Verlet time-stepping for position and velocity, translational and rotational (Cundall & Strack, 1979b; Duriez & Bonelli, 2021; Kawamoto et al., 2016), as it is common for the calculation of particle trajectories in a variety of DEM applications. LS-ICE produces a first order error in the constant time step size dt. For our simulations we used a time step of 1 second. This approach also provides good numerical stability if the time steps are sufficiently small, as well as time reversibility, at no significant additional computational cost over the basic Euler method. Forces and moments are obtained from floe contacts, then they are used to update velocities in a forward stepping scheme and these velocities are utilized to update floe positions and rotations.

2.3 Model Data and Evaluation

Datasets

As introduced in Section 2.2, we use NASA MODIS images from the visible spectrum (MODIS Science Team, 2017) to initialize the shapes of coarse floes, and the concentration of fine floes in our model. Our study region is Baffin Bay, between 78.1°W and 61.2°W and 67.2°N and 80.1°N, in the summer time for years 2018 and 2020 (see Figure 2.1). During this period, MODIS images show a sharp decline in sea ice concentration, from about 80% to close to ice-free, over about 50 days for 2018. We choose this particular region because large floes tend to remain within the domain over several weeks, rather than being advected southward, as in Fram or Nares Strait.

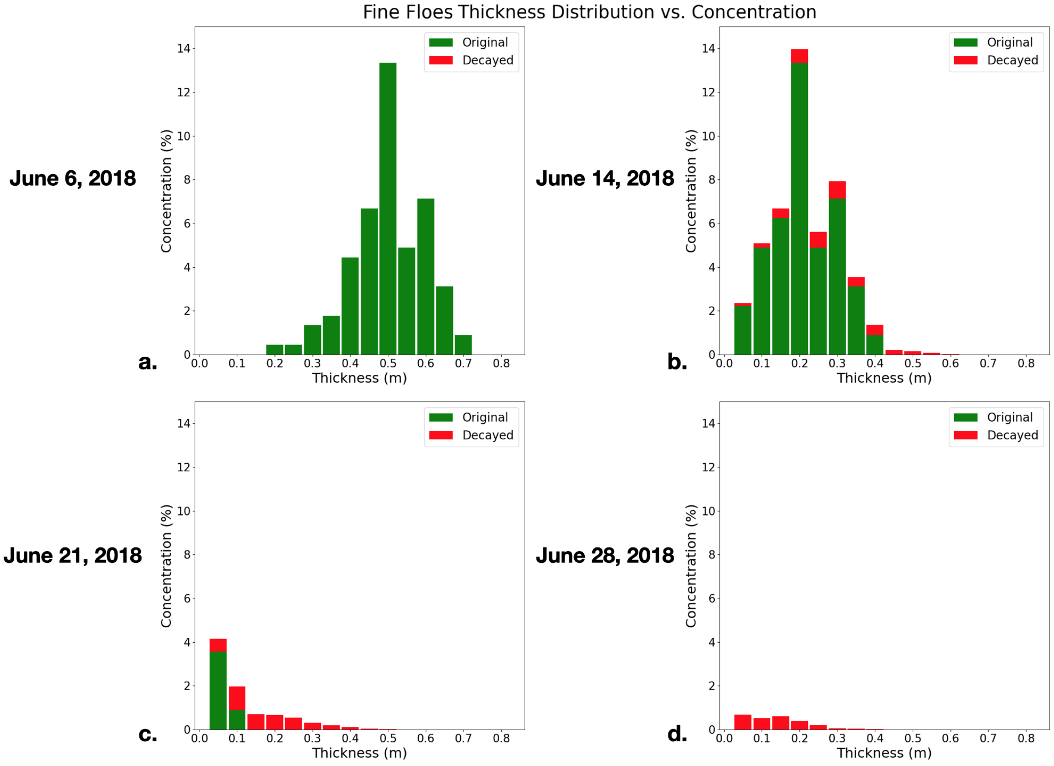

Figure 2.6: Floe thickness distribution versus concentration for fine floes, where concentration equals fine floe area of each thickness bin divided by total simulation area. Snapshots of: a. the start of the simulation, b. as melt and breakage initiate, c. as melt and breakage develop and almost eliminate all original fine floes and d. after significant sea ice decay, with only decayed coarse floes remaining. Green bars represent original fine floes. As the simulation evolves, the thickness of these fine floes reduces due to melt, but their area is assumed to remain constant until thickness reaches zero and they are lost. Additionally, as coarse floes break into pieces that are smaller than the coarse/fine length scale threshold (2 km), they are converted to fine floes, represented by the red bars, as decayed coarse floes. Note how the thickness distribution shifts to the left (thinner floes) and down (reduced concentration) for fine floes and how decayed coarse floes prolong the presence of fine floes in the simulation.

Satellite images have a daily time resolution, but some images are not used, due to cloud cover preventing the accurate distinction of sea ice floes. We manually select images where cloud coverage is low enough to reliably segment the floes, and where the identification of fine floes is not notable distorted by clouds. This produces 17 snapshots for year 2018 and 12 for year 2020. From these selected images, we extract sea ice concentration for both coarse and fine floes, as well as floe size distribution, based on the mean caliper diameter. The mean caliper diameter refers to the diameter of a floe if it were converted to a circular floe with

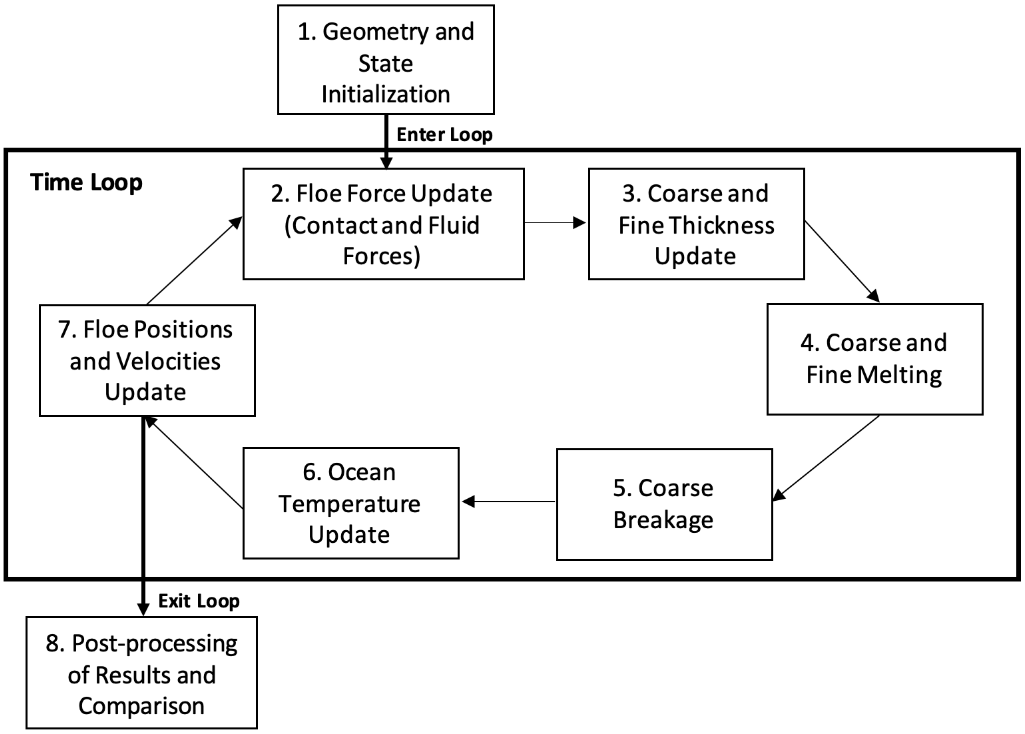

Figure 2.7: Main steps in the LS-ICE simulation. After initial conditions are defined and parameters chosen in Step 1, a loop for kinematics, thermodynamic and breakage processes is developed for the duration of the period studied (looping Steps 2–7). Output, in Step 8, has the same temporal resolution of satellite snapshots for comparison.

the same surface area (Montiel & Squire, 2017). Beyond satellite imagery, we also inform our model with reanalysis of surface ocean temperature, area-averaged sea ice thickness and mixed layer depth, obtained from the Copernicus Marine Database (Mercator Ocean International, 2015). The surface ocean temperature derived from this database combines meteorological station, satellite sensor data and the TOPAZ4 Arctic Ocean assimilation system, to provide data with a spatial resolution of 12.5 km. The ice thickness is similarly obtained as a gridded reanalysis product with data originating from the CryoSat-2 sensor. This sensor averages varying thickness as a continuum value for each cell in the domain grid, regardless of whether the ice is a whole or broken apart within the cell. The mixed layer depth is obtained from TOPAZ4 and HYCOM (Hybrid Coordinated Ocean Model).

Parameter tuning and performance evaluation

We tune the model to reproduce the evolution of key statistical quantities, namely the concentration of coarse and fine floes, the mean sea ice thickness and the mean surface temperature over the domain. We seek to minimize the root mean square error for these quantities, calculated as follows:

$$RMSE = \sqrt{\frac{\sum_{i=1}^{N}(x_i - \hat{x}_i)^2}{N}}, \tag{2.20}$$

where N is number of observations or satellite snapshots, x_i is a simulation data point and $\hat{x}_i$ is a field data point. To evaluate this RMSE, we use all the satellite snapshots available within the simulation time frame (with low cloud cover and feasible floe segmentation) as they allow to identify sub-optimal tuning with more ease.

Finding the optimal value for each of the parameters in Table 2.1 would be a difficult endeavor, so we focus the tuning procedure on the following three salient parameters, which have a strong influence on the breakage and melting dynamics of the model: (1) the breakage frequency B, (2) the ice/ocean vertical heat exchange parameter q_v, and (3) the solar forcing magnitude S. All other parameters are set to standard values commonly used in climate models.

We vary q_v and S over typical ranges used in the literature, and explore variations in B over a broad range, while eliminating extreme values that result in large RMSE (see last three rows of Table 2.1). To define a range for S values we consider its strong influence on ocean temperature evolution, and smaller impact on other model outputs. We run more than 800 simulations for different combinations of the ranges in Table 2.1 over a 3D parameter space. When there is competition between minimizing RMSE for each of the model outputs, we prioritize them in the following order: coarse floe concentration, fine floe concentration, mean ocean temperature (both RMSE and closeness to final temperature value) and mean sea ice thickness. We place the most emphasis on the coarse floe concentration as its observed evolution is less likely to be impacted by cloud cover and noise introduced by image processing than fine floes.

We apply this tuning method to the data corresponding to year 2018. The lowest RMSE for the concentration of coarse floes is 2.1% for the following parameter values: S = 310 Wm^{-2}, B = 3.6 h^{-1} and q_v = 25 Wm^{-2} °C^{-1} (Figure 2.9 a). These parameters correspond to the results shown in the next section. We also test the robustness of this tuning to the randomness in the floe breakage process, by executing 10 additional simulations with the same model parameters and a different random seed. We find that the overall standard deviation in coarse floe concentration for these additional runs is 0.026 %, and the deviation in other model results is similarly weak. We therefore infer that the random nature of the breakage mechanism does not significantly affect the model's behavior and performance for the statistical quantities of interest in this analysis.

2.4 Model Validation Results

We will first describe model validation results for the year 2018, and subsequently test whether the same model parameters produce adequate results for year 2020. The intent is not to exactly reproduce the changes to each individual ice floe in the simulation, but rather capture the evolution of statistical properties, including fine and coarse floe concentrations, mean ice thickness, and domain-averaged ocean temperature. These results pertain to the simulation that produces the smallest overall RMSE values for the output described in the prior section while prioritizing the reduction in coarse floe concentration error, obtained by selecting the parameter values summarized in Table 2.1.

The sequence of satellite imagery shows the breakage and weakening of coarse floes between June–July 2018 (Figure 2.8 a–d, which also compares some basic properties of the system between satellite data and simulations). Visual inspection of the model output at the corresponding dates shows a similar behavior between field data and simulation, with coarse (tracked) floes from LS-ICE fracturing into smaller pieces with arbitrary shapes, and gradually disappearing from the domain. The quantitative evolution of coarse floe concentration in our model matches closely with the satellite processed data, yielding an RMSE of 2.1% (Figure 2.9 a). The general evolution of the fine floe concentration captures the decline trend, though it tends to overestimate its initial decline rate over the first 10 days and partly underestimate it during the last 35 days, producing an overall RMSE of 13.1% (Figure 2.9 b).

The evolution of coarse floe concentration is affected by mechanical breakage as well as thermodynamic melt. As these large floes break into pieces that are too small to track, their mass is added to fine floes, which are only affected by basal melt. The contribution of lateral melt to the reduction of coarse floe concentration and mass is relatively small but this might be different for fine floes, consistent with results from previous studies (Smith et al., 2022; Toyota et al., 2006), further research will elaborate on this. The balance between lateral and basal melt, as well as the impact of breakage in the overall evolution of sea ice during these conditions will be explored further in future work.

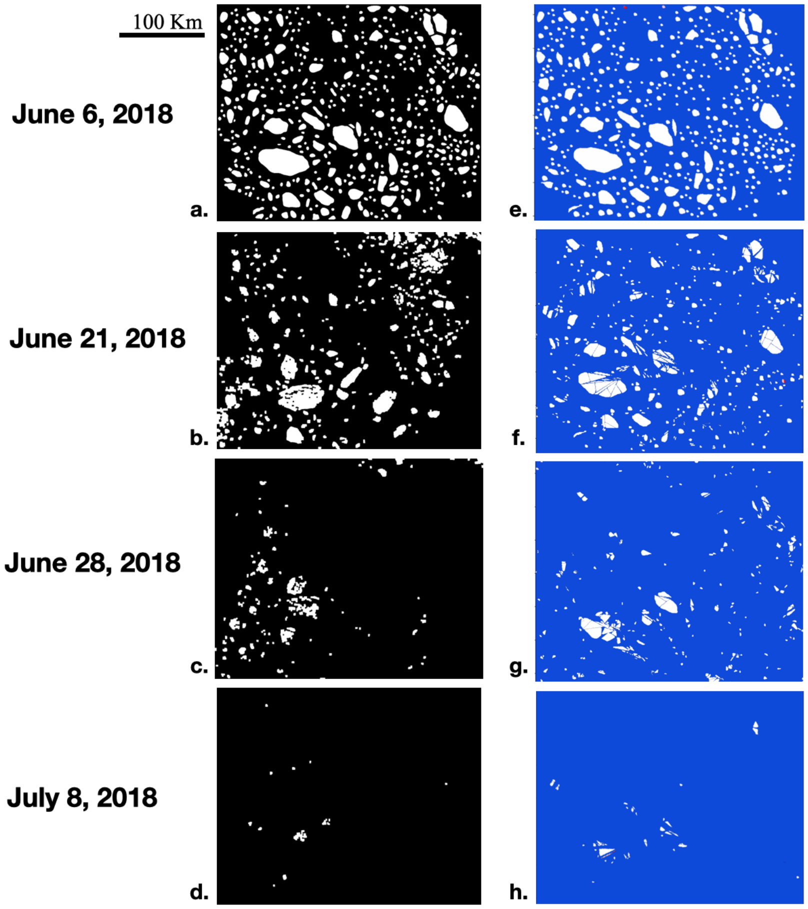

Quantity	Data	Sim.
# of Floes	493	493
Coarse Con.	18.49	18.49
Fine Con.	46.24	46.24
Ave. Thick	0.53	0.51
Mean Diam.	6.36	6.36
Ave. Temp.	-1.55	-1.54

Quantity	Data	Sim.
# of Floes	271	506
Coarse Con.	11.60	10.75
Fine Con.	25.34	8.87
Ave. Thick	0.44	0.22
Mean Diam.	6.78	4.63
Ave. Temp.	-1.25	-0.44

Quantity	Data	Sim.
# of Floes	96	288
Coarse Con.	2.92	5.81
Fine Con.	11.40	3.12
Ave. Thick	0.36	0.20
Mean Diam.	5.68	4.49
Ave. Temp.	-1.16	0.13

Quantity	Data	Sim.
# of Floes	13	10
Coarse Con.	0.32	0.08
Fine Con.	4.69	0.31
Ave. Thick	0.33	0.10
Mean Diam.	5.20	2.89
Ave. Temp.	-1.09	0.81

Figure 2.8: Evolution of coarse floes from MODIS imagery (left column) and from the LS-ICE simulation (center column), at four characteristic snapshots taken between June–July 2018. For each snapshot a small table (right column) summarizes and compares satellite data and simulation main results. Units for concentration are in %; thickness is in meters; mean diameter is in km; and average temperature is in °C.

We next compare the observed versus simulated floe size distribution at specific snapshots at the start and during significant concentration reduction events (Figure 2.10), corresponding to the same snapshots as in Figures 2.5 and 2.6. The simulation emulates the FSD from observations relatively closely, particularly over the first 15 days. By halfway of the simulation, due to the simplified breakage mode and differences in image resolution, it does not always capture the largest diameters

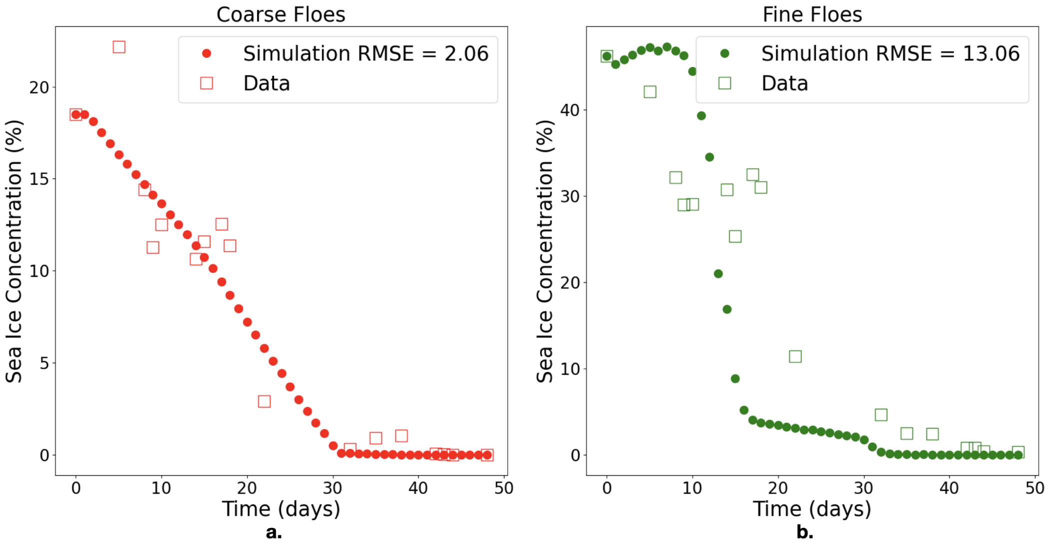

Figure 2.9: Time evolution of a. coarse and b. fine floe concentrations for the year 2018 (Day 0 is June 6, 2018). Hollow squares represent observational data obtained from imagery, while circles represent simulation data. Parameter values of the model for the lowest coarse RMSE error are: $S = 310$ Wm^{-2}, $B = 3.6$ h^{-1} and $q_v = 25$ Wm^{-2} °C^{-1}.

from the field, leading to a notable increase in the error. Introduction of physically-based breakage events could correct the absence of larger floes at the end of the simulation, since random breakage currently generates a relatively uniform FSD, while satellite images suggest that larger floes tend to persist for longer. Interestingly for this period, the shapes of both the observed and simulated FSD curves remain relatively uniform throughout the course of the season, perhaps hinting at self-similar processes governing the spring to summer transition.

The thermodynamic ocean model is able to represent the overall rise and decline, respectively, in domain-mean temperature and ice thickness (Figure 2.11). For temperature, the model yields an RMSE of 0.37 °C and a final value that is relatively close to observations (0.4 °C difference). Discrepancies between the model and field measurements may be due to external heat sources in the field (ocean currents and wind), which are not accurately represented by our model. The total thickness simulated by LS-ICE follows the general trend of the reanalysis data, with an RMSE of 0.062 m. Differences are potentially caused by the use of a continuum processing of observed reanalysis data, rather than the discrete approach used by the LS-ICE model, and due to breakage differences that may induce thickness reduction in the center of floes earlier for the simulation when calculating average weighted values.

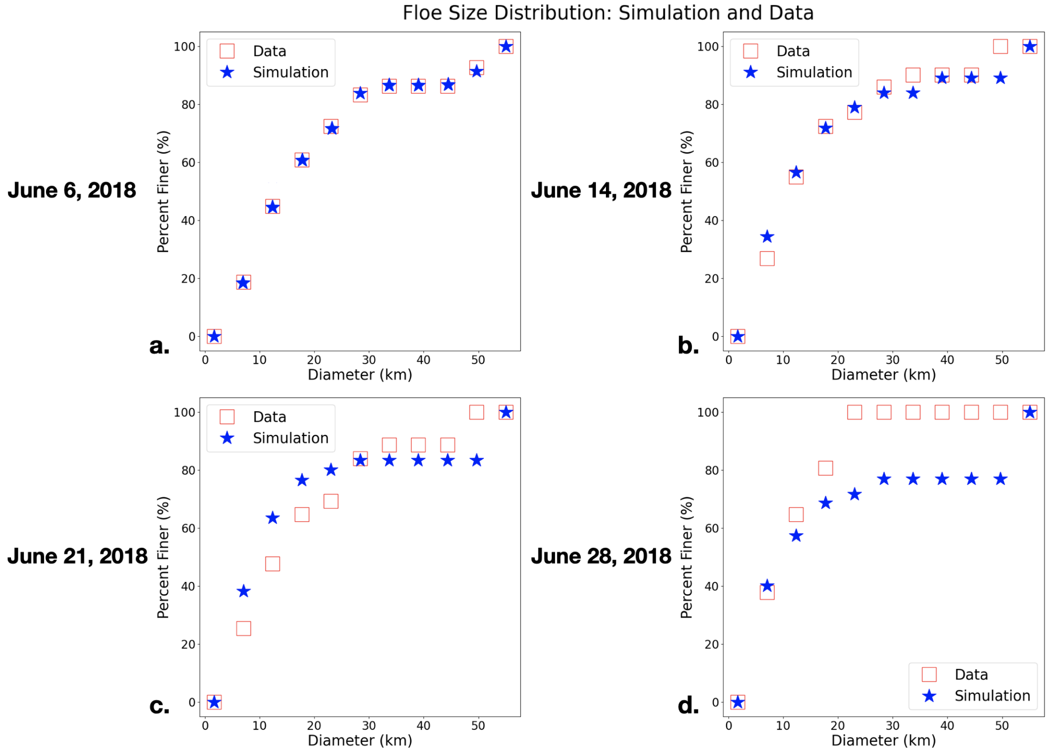

Figure 2.10: Cumulative floe size distribution (FSD) evaluated for the simulation (blue stars) and the MODIS imagery (red squares) at characteristic snapshots for June 2018, namely a. the initial state, b. at the initiation of melt, c. during the development of melt, and d. the effect of random breakage on larger floe presence. Floes are binned according to their mean caliper diameter (x-axis), with a bin size of about 5 km. The y-axis represents the percentage of total coarse floes that have a diameter equal or smaller than the corresponding bin.

Due to the strongly coupled nature of the ice/ocean system, we find that appropriately capturing the evolution of sea ice thickness and ocean temperature are an important prerequisite for obtaining the correct evolution of sea ice concentration. Conversely, sea ice concentration plays a vital role in regulating ocean temperature, such that if the ice melts too early, the ocean temperature can rise significantly faster, due to its small albedo value.

After calibrating the model with data from year 2018, we test its performance over year 2020, for which the sea ice decline occurs in a shorter period. We only modify the initial conditions for temperature, floe geometry and thickness, according to the corresponding field data in year 2020, without any additional fitting. The model forecasts the evolution of coarse floe concentration with an error of 3.2% and fine floe concentration with an error of 10.9% (Figure 2.12). As in year 2018, the

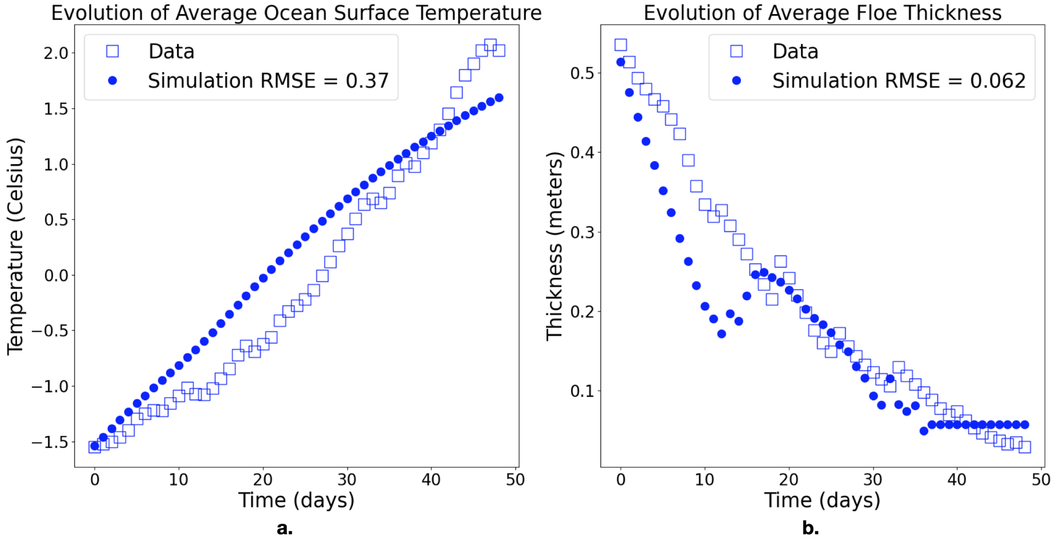

Figure 2.11: Time evolution of the a. surface ocean temperature and b. sea ice thickness, averaged over the domain of interest during (June–July 2018) for the field data (blue hollow squares) and the simulation (blue circles).

performance for coarse floes is superior, as the representation of fine floe in our model is relatively idealized. The simulated thickness and temperature evolution are also similar to field data, but with a slightly lower error for temperature (0.22 °C) and a similar error for thickness (0.062 m) compared to year 2018. Particularly, both 2018 and 2020 coarse results predict the amount of time for sea ice to approach zero concentration. These results suggest that it is purely the initial conditions that drive the differences in melt rates between years 2018 and 2020. The starting average sea ice thickness is about 0.5 meters for 2018, while only 0.3 meters for 2020. The initial average ocean temperature is -1.5 °C for 2018 and -1.37 °C for 2020. Hence, the year 2018 is less susceptible to concentration decrease and sea ice is removed at a slower rate, since it starts with thicker floes and a colder ocean temperature than year 2020.

2.5 Discussion

This study presents a new discrete-element model of sea ice (‘LS-ICE’) designed to emulate the behavior of individual sea ice floes as they collide with each other, fracture, and melt in response to ocean and atmosphere forcings. The model is based on analytical level-set functions, which are used to represent the advection, rotation, breakage and melt of arbitrarily-shaped sea ice floes, coupled to ocean and atmospheric fields. Here, we test the LS-ICE’s behavior in the Arctic summer melt

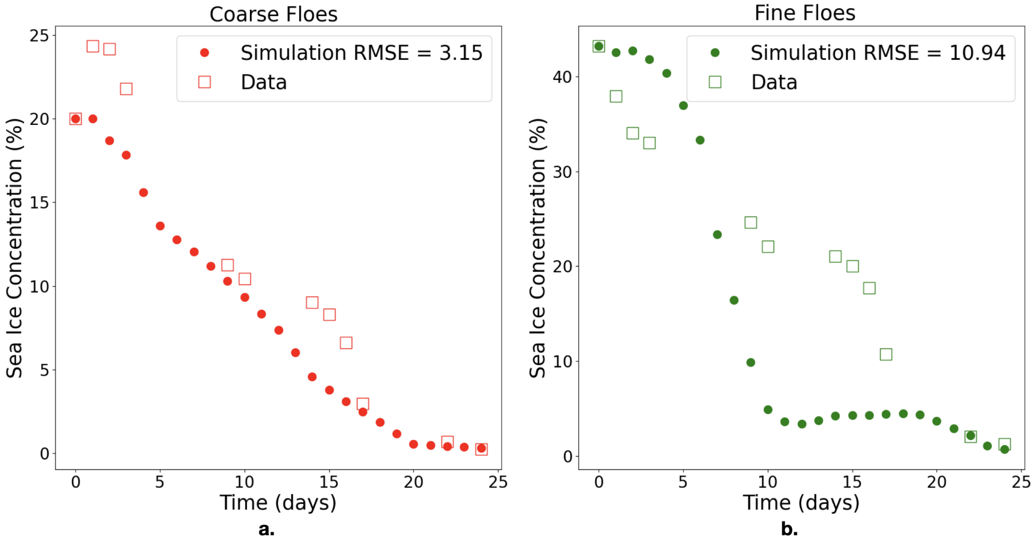

Figure 2.12: Time evolution of a. coarse and b. fine floe concentrations for the year 2020 (Day 0 is June 4, 2020). Hollow squares represent observational data obtained from imagery, while circles represent simulation data.

season over Baffin Bay, where sea ice transitions from approximately 80% concentration to ice-free conditions between the months of June and July. This process is dominated by floe-scale dynamics, which are typically not well represented by continuum-based sea ice models. Our tuning procedure prioritizes the emulation of resolved floes over other output variables, as it is likely the most reliable quantity obtained from observations. We tune the model according to data in year 2018, finding appropriate parameters affecting melt and breakage. Without further tuning, the model also captures the statistical evolution of sea ice in year 2020, when the decline of sea ice concentration is approximately 1.5 times faster than in 2018.

LS-ICE belongs to a family of sea ice DEMs, which have taken variety of approaches to improve and understand the floe-scale behavior of sea ice. Bonded particle methods opt for modeling of a large number of simple particles, which have scales that are smaller than typical floes, and are joined together by breakable bonds to form floes or sheets of ice (Dansereau et al., 2017; West et al., 2021). These bonded particles can form arbitrary shapes, as in LS-ICE, but have to explicitly represent a large number of particles, with commensurate computational demands. On the other hand, sea ice may be represented as a collection of polygons like in (Manucharyan & Montemuro, 2022), which represent observable floes, as in the LS-ICE. This considerably reduces the number of elements that have to be explicitly modelled, but increases the complexity of their self interactions.

The use of LS-ICE to represent summer-like melt conditions is distinct from most of the past work in this field, which has tended to focus on more highly concentrated sea ice regions (Dansereau et al., 2017; Manucharyan & Montemuro, 2022; West et al., 2021). Furthermore, one of the distinguishing features of the LS-ICE is its ability to model arbitrary (e.g., convex/non-convex, sharp/smooth) shapes extracted directly from satellite imagery, with minimal geometrical simplifications. These more realistic shapes expand on previous work using disk-shaped DEMs (Damsgaard et al., 2018; Gupta & Thompson, 2022b; Herman, 2013, 2017) and circular floe breakage models (Montiel & Squire, 2017). Our elements can also morph (melt) and split (fracture) in response to external forcings from ocean and atmospheric models, set on a continuous grid. This ability, along with a resolved thickness distribution within each floe, is important for capturing the essential physical mechanisms and feedbacks at play during these summer sea ice conditions. Here, both the melt and breakage models are purposefully kept simple, to avoid tuning an excessive number of model parameters. Despite this simplicity, the methodology is effective in emulating the observed evolution from satellite data of statistical quantities in the domain for moderate to low sea ice concentrations (20 - 80%).

Moreover, LS-ICE (just as its parent, LS-DEM) has the capability of resolving internal stresses and calculating breakage based on both DEM contact forces and finite element methods applied on individual floes, though these tools were not exploited in this study. These more advanced capabilities of the LS-DEM framework come at a non-negligible computational cost, as the method's computation time is 1–2 orders of magnitude higher than more traditional DEMs. Nevertheless, these more precise representations of floe-scale processes may help improve the parameterization of floe breakage for other DEMs and continuum models, particularly as parallelization over graphical processing units (GPU) could allow significant optimization (up to 20 times faster for a 3D DEM using the OpenMP framework according to (Duriez & Bonelli, 2021)).

Beyond simulating floe-to-floe collision and melt and breakage processes, LS-ICE provides the framework to study the interaction of ships and marine structures with sea ice floes. Marine vessels and infrastructure can undergo variable spatial and temporal loads due to sea-ice floe contact (Lubbad & Løset, 2011), which will depend notably on sea ice concentration, floe geometry, ocean currents and winds, and ship speed and power. LS-ICE may be used to study the forces on ships and structures due to individual floes in both compact and broken sea ice configurations

(Jou et al., 2019). This model may also be effective in predicting ice breakage due to the passage of ships into the pack, and optimizing Arctic shipping routes.

Future work involves applying the model at different locations, periods and scales with higher resolution field data. The fractal nature of sea ice (Key & McLaren, 1991; Rampal et al., 2019) makes it possible to implement the discrete element approach for different scales or even use it as an input for multi-scale modeling. A critical aspect to consider for future research is accounting for different mechanisms of floe breakage, which better capture physically-based criteria. In our framework, level sets can also be used to calculate surface tractions and critical breakage stress and location for fracture. This capability to define breakage, like in (Harmon et al., 2020), could then be coupled to morphing floes. Floe collision, ocean and wind currents, inter-floe forces, thermal expansion differences, melt pond hydrofracture and wave flexural loading can all combine in different ways to break floes in mixed fracture modes. Introduction of breakage criteria can result in better coupling with ocean surface velocity, wave height and wave period from data repositories and in-situ buoys. This information can provide better predictive capacities, as storms and other significant wave events might affect breakage frequency. This is particularly relevant because satellite images imply that floe breakage rate is not constant, but happens in an episodic manner. Further improvements include extending the framework to different sea ice regimes, where other processes, such as freezing, ridging and rafting become important.

Additionally, we can emphasize the opportunities of utilizing the LS-ICE methodology beyond sea ice, applied to any granular medium composed of breakable and morphing particles. Research in granular materials undergoing a combination of comminution, chipping, dissolution, erosion, wear, volumetric thermal variations, agglomeration, sintering or other changes in shape could be greatly benefited by this method.

Chapter 3

SEA ICE BREAKAGE AND MELT EFFECT ON CONCENTRATION AND FSD: APPLICATION OF LS-ICE

Moncada, R., Gupta, M., Thompson, A., & Andrade, J. E. (2023). Role of breakage, melt and floe size distribution on sea ice summer transition. *Geophysical Research Letters. In Review.*

3.1 Outline

This chapter explores the spring-to-summer transition of sea ice over Baffin Bay, a region west of Greenland characterized by easily distinguishable floes. We leverage the LS-ICE DEM introduced in the last chapter (Moncada, Gupta, Thompson, & Andrade, 2023a), along with satellite imagery, to diagnose the relative contributions of breakage and melt in governing the evolution of sea ice concentration and FSD between June and July 2018. We conduct a range of simulations exploring the sensitivity of these metrics to breakage and melt rate parameters in the model, and decompose the FSD trend to quantify their contributions over floes with diameters ranging between 2 - 50 km. The parameter regime with the best fit to observations suggests that breakage and melt play comparably important roles in governing the summertime sea ice decline, with breakage being particularly important for the decay of floes larger than 10 km. We also include a comparison with a different year, 2020 for reference, to observe how the relative importance of breakage and melt is affected by initial and forcing conditions and how it affects FSD and concentration results.

Table 3.1 has a summary of the parameters tuned for the sensitivity analysis. Note that both breakage and melt impact the FSD, but also initial characteristics of the FSD influence how breakage and melt affect the system. Hence, a feedback loop among all these conditions starts forming and systems are highly dependent on initial conditions. For example, a highly uniform sea ice mosaic has already high surface area for melt to remove mass faster. This results in accelerated concentration decline until all sea ice is removed. On the other hands, a more well-graded sea ice system, with many large floes, will require first for breakage to increase the system uniformity. Then, melt will accelerate the feedback loop, just like with the uniform system. This loop will be disrupted once all sea ice is removed from a region.

Table 3.1: Parameters Tuned for Melt, Breakage and FSD Sensitivity Analysis

Variable	Meaning	Value	Units
S	Solar shortwave heat flux (Solar Melt)	240 – 360	W m^{-2}
q_v	Rate of vertical ice melt (Oceanic Melt)	5 - 200	W m^{-2} °C^{-1}
B	Breakage Frequency	1.44 – 250	h^{-1}
α	FSD power exponent (CNFD slope)	2 – 3	km^{-1}

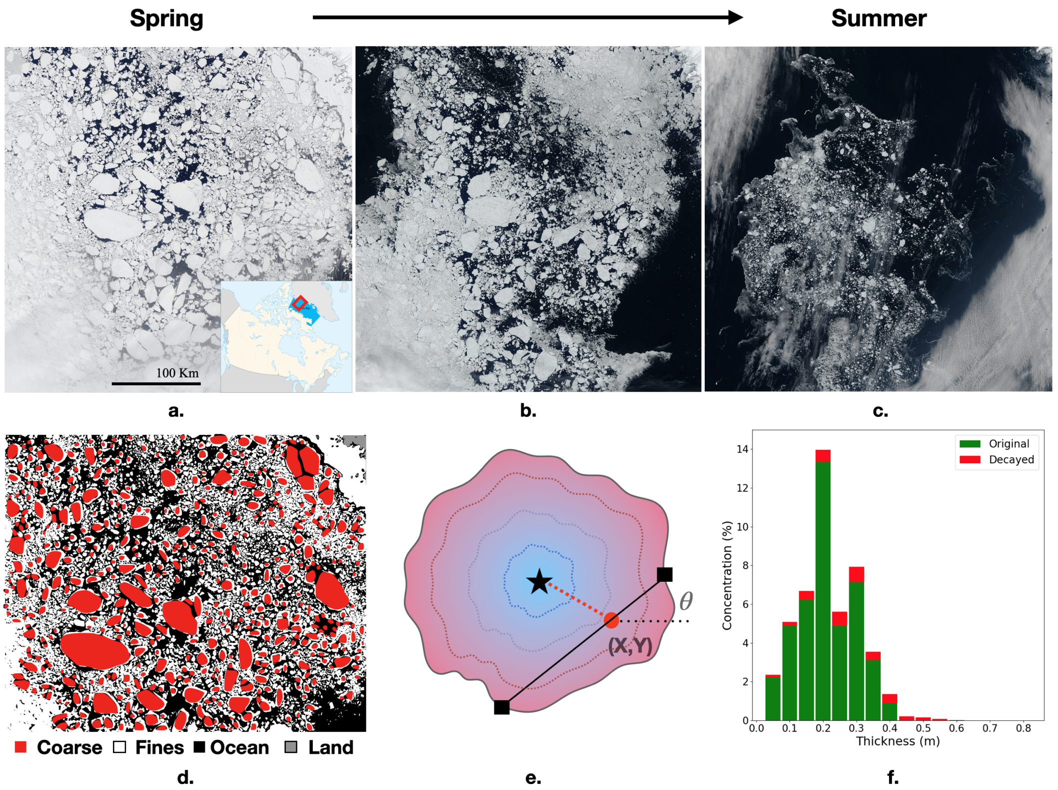

Figure 3.1: Snapshots of NASA MODIS imagery taken within Baffin Bay on a. June 6, 2018, b. June 28, 2018, and c. July 24, 2018, illustrating rapid loss of sea ice during the melt season (from > 60% concentration to almost ice-free) for location 78.1°W and 61.2°W and 67.9°N and 80.1°N. The inset in panel a. indicates the location of this domain. Coarse and fine comparison: d. Characteristic segmentation of the image into coarse floes (red) and fine floes (white), with ocean (black) and land (gray). e. Level-set representation of coarse floes by the LS-ICE model. Each coarse floe carries its own thickness distribution grid. Breakage of coarse floes is idealized as a straight line (black curve) with random orientation (θ) and random location (X,Y). f. Statistical representation of fine floe concentration, shown as a distribution over thickness bins. Concentration of original fine floes is shown in green, and contribution from decayed coarse floes, in red.

3.2 Modeling Framework

The LS-ICE model

This work leverages the level set discrete element sea ice model (LS-ICE), introduced in (Moncada, Gupta, Thompson, & Andrade, 2023a) and Chapter 2, to represent the evolution of individual sea ice floes during the spring-to-summer transition in Baffin Bay. Level set functions are used to define the geometry of arbitrarily-shaped (non-convex) floes and simulate their kinematics as they drift and collide due to external forcings (Harmon et al., 2020; Kawamoto et al., 2016, 2018).

Floe shapes are initialized from segmented NASA MODIS satellite imagery obtained at a resolution of 1 km within Baffin Bay on June 6, 2018 (MODIS Science Team, 2017) (Figure 3.1(a)). Areas covered by sea ice are identified via an empirical threshold on pixel brightness and individual floes are detected via watershed segmentation (Lopez-Acosta et al., 2019). Given the image resolution, we only seek to detect and resolve floes with size greater than 2 km. Each floe carries a 2D thickness field, initially uniform, which can represent melt in response to a slab ocean and prescribed atmospheric heat fluxes, as follows (Moncada, Gupta, Thompson, & Andrade, 2023a):

$$\rho_i L_f \frac{\partial h}{\partial t} = q_v(T_f - T) - S(1 - a_i) + (A + BT_f), \tag{3.1}$$

where $h = h(x, y, t)$ is floe thickness, $T = T(x, y, t)$ is the ocean temperature under the ice, q_v is the ice/ocean heat exchange parameter, S is the solar heat flux, T_f = -1.8 °C is the sea ice melting temperature, and other parameters are constants specified in the next section (time-scales) or in (Moncada, Gupta, Thompson, & Andrade, 2023a). There is no explicit parameterization of lateral melt, but we find that floes tend to melt faster at their edges in our simulations due to the presence of warmer waters at these locations.

The ocean temperature below resolved floes evolves following:

$$\rho_0 c_p H \frac{\partial T}{\partial t} = \rho_0 c_p H k \nabla^2 T - q_v(T - T_f), \tag{3.2}$$

where H = 25 m is the uniform mixed layer depth and k = 20 m^2 s^{-1} is a prescribed horizontal diffusivity for a mixed layer eddy. Mixed layer depth value is the average observed during the period studied. Sea ice is assumed to be entirely insulating to solar heat fluxes, such that there are no atmospheric heat flux terms in Eq. (2.14).

Floes are advected in a doubly-periodic domain by a spatially uniform ocean forcing that reproduces mean sea ice drift velocities in the region, estimated from satellite-derived motions (Moncada, Gupta, Thompson, & Andrade, 2023a), though floe velocity sensitivity is low.

For simplicity, fracturing of floes is represented by a prescribed breakage rate B, which defines the frequency at which a floe is broken into two pieces by a straight line with random orientation across a random point within the floe. Large or ‘coarse’ floes with a characteristic diameter greater than 2 km are represented explicitly by LS-ICE, while smaller or ‘fine’ floes are defined by a thickness distribution across bins of constant area, which decay via melt. Coarse floes that break or laterally melt to a size smaller than 2 km are added to the statistical fine floe representation (Figure 3.1(d), (e), (f)).

Model validation

(Moncada, Gupta, Thompson, & Andrade, 2023a) demonstrates the model’s ability to reproduce the observed evolution of sea ice concentration (fine and coarse), sea ice thickness, floe size distribution and ocean temperature, averaged over the chosen domain during the summer of 2018. The datasets used to initialize and validate the model include NASA MODIS satellite images (MODIS Science Team, 2017), and the Copernicus Database (Mercator Ocean International, 2015), which provides sea ice thickness and surface ocean temperature based on reanalysis data from satellite observations, meteorological stations and Arctic numerical models (12.5 km resolution).

The initial conditions for our 2018 simulation were 18% coarse floe concentration, 44% fine concentration, -1.5 °C surface ocean temperature and 0.5 m average ice thickness. The model was compared to observations using coarse floe and total sea ice concentration, surface temperature, and average thickness, in this order of priority, by tuning the B, S, and q_v parameters. The procedure used to obtain the ‘best fit’ simulation to observations is detailed in (Moncada, Gupta, Thompson, & Andrade, 2023a) and in the next section, as well. We find that the observed evolution of temperature constrains S and that the evolution of coarse floe concentration and size distribution are most sensitive to B. We empirically select parameter values that minimize the errors of these various indicators and explore the sensitivity of our choices in the following analysis. We also test our results on year 2020 and draw similar conclusions to 2018. The bulk of this chapter focuses on the behavior of coarse floes (> 2 km), as those are better resolved by our model, but behavior of fine floes is also presented in a more limited fashion.

3.3 Interactions of Breakage and Melt on Mass and Concentration Loss

Sea ice mass loss rate

The main indicator to track sea ice loss is mass loss rate or the amount of mass lost per unit of time. With it, we can explore the losses due to vertical melt rather than only areal concentration reduction or lateral melt. Total coarse mass at a specific time step 'j' is calculated from:

$$m_C^j = \rho_i \Sigma_{k=1}^{N_{floes}} A_k^j h_k^j, \tag{3.3}$$

found by adding up the product of area, thickness and density of all discrete coarse floes. Coarse mass loss rate, normalized by initial coarse mass (hence units of d^{-1}), is obtained by:

$$\frac{dm_C}{dt} = \frac{m_C^f - m_C^0}{t_{loss}\, m_C^0}, \tag{3.4}$$

where m_C^0 stands for initial coarse floe mass, m_C^f is the mass by the end of the simulation and t_{loss} is the time to reach total mass loss, if the simulation removed all coarse mass before being completed, or total simulation total time, if not all coarse mass was removed before the end of the simulation. Units of this rate are in d^{-1}, since we normalized by initial mass to use values between 0 and 1. While mass loss is very insightful and helps separate breakage and melt contributions, in order to do an error analysis and choose the best parameters to fit observations, concentration is a better metric. This is because there is no detailed information about thickness spatial distribution or temporal evolution, beyond the average for the region. Simulations assume irreversible loss of sea ice, hence both mass and concentration values always results in loss over time, hence results are reported as absolute rates for convenience.

Sea ice concentration loss rate

The domain-averaged sea ice concentration

$$C(t) = \frac{A_{ice}(t)}{A_{domain}} * 100\% \tag{3.5}$$

tends to drop in time over the course of our simulations. This decline is not necessarily linear, motivating the need to find a consistent metric to characterize its evolution. We choose to define a mean concentration loss rate by recasting the sea ice decline as a linear drop that conserves the change in concentration between the start and end of the simulation ΔC, as well as time-integral of the original evolution $\int C(t)\ dt$. The equivalent time taken for this linear decline to occur is then:

$$\Delta t_{eq} = \frac{2 \int C(t)\ dt}{\Delta C}, \tag{3.6}$$

based on the area of a triangle with sides Δt_{eq} and ΔC. The mean concentration loss rate then becomes:

$$\overline{\frac{dC}{dt}} = \frac{\Delta C}{\Delta t_{eq}} = \frac{\Delta C^2}{2 \int C(t)\ dt}, \tag{3.7}$$

defined as positive. The loss metric in Eq. (3.7) characterizes the persistence of sea ice within the domain. Simulations incurring a large concentration loss at the start of the simulation are therefore weighted towards a higher loss rate than those incurring loss towards the end of the simulation.

Sea ice mass loss and relative importance

In the spring-to-summer transition, sea ice is lost due to a combination of top, basal and lateral melt, which can be accelerated by individual floes breaking into smaller pieces. The relative importance of these mechanisms in driving mass loss of coarse floes can be examined by considering the following decomposition:

$$\Delta m_C = \Delta m_S + \Delta m_O + \Delta m_B, \tag{3.8}$$

where Δm_S, Δm_O, Δm_B are the coarse floe mass losses due to solar melt, oceanic melt and breakage, respectively. Floes are considered lost due to breakage when they fracture into pieces that are smaller than the coarse/fine threshold (2 km). The simulation with the best fit to observations exhibits the following percentage split: $\Delta m_B : \Delta m_S : \Delta m_O = 0.42{:}0.5{:}0.08$, which suggests that solar melt and breakage play a comparably important role and that oceanic melt is less dominant. We investigate the sensitivity of the coarse floe mass loss rate and the split between each of its contributions in Eq. (3.8) by conducting a suite of simulations varying the breakage rate B, the ice/ocean heat exchange parameter q_v and the solar constant S (Figure 3.2). The resulting scenarios represent different environmental regimes that may occur over the course of a given melt season, in different regions, or as part of inter-annual variability within Baffin Bay. We cast our diagnostics in terms of mass loss rate, but concentration loss rate has similar results.

The relative sensitivity of sea ice mass loss to breakage and melt is investigated by varying B and S for fixed q_v. Increasing S directly accelerates surface melt and can indirectly enhance basal/lateral melt by warming the surrounding ocean. Similarly, increasing B directly accelerates coarse mass floe loss by reducing the size of floes beyond the fine/coarse threshold and can indirectly promote lateral melt by increasing the total perimeter of resolved floes. Near the best fit simulation parameters, B and S both influence loss of floes, but under high breakage regimes (large B), B plays a more dominant role (Figure 3.2(a)). The relative importance of breakage versus melt can be quantified via the following ratio:

$$\mu = \mu_{BM} = \frac{\Delta m_B}{\Delta m_S + \Delta m_O}. \tag{3.9}$$

For reference, $\mu_{BM} = 0.73$ for the best fit simulation, such that melt loss dominates slightly over breakage loss. This is consistent with the characteristic time scales associated with breakage and melt, respectively, explained later in this chapter. Figure 3.2(c) shows that μ_{BM} is strongly controlled by B and varies between a melt-dominated regime ($\mu_{BM} < 1$ at low B) and a breakage-dominated regime ($\mu_{BM} > 1$ at high B). Under high breakage, compared to the best fit, increasing S allows a larger fraction of the coarse floe decline to occur via melt, but does not noticeably change the mass loss rate, which suggests a competition between breakage and melt. Under low breakage, increasing S promotes coarse mass decline, illustrating a regime where breakage and melt work together.

We next investigate interactions between solar and oceanic melt by varying q_v and S for fixed B. The loss of coarse floes is equally sensitive to changes in q_v and S for the entire parameter space explored (Figure 3.2(b)). This suggests that solar and oceanic melt do not strongly compete against each other, but that they independently promote a higher melt rate for coarse floes. The ratio:

$$\mu_{OS} = \frac{\Delta m_O}{\Delta m_S}, \tag{3.10}$$

quantifies the relative contributions of oceanic and solar melt and is $\mu_{OS} = 0.15$ for the best fit simulation. The parameter μ_{OS} is strongly sensitive to q_v near the best fit scenario and equally sensitive to q_v and S at lower S values with respect to best fit (Figure 3.2(d)). This results in a solar-dominated regime at low q_v values, and an ocean-dominated regime for high q_v and low S.

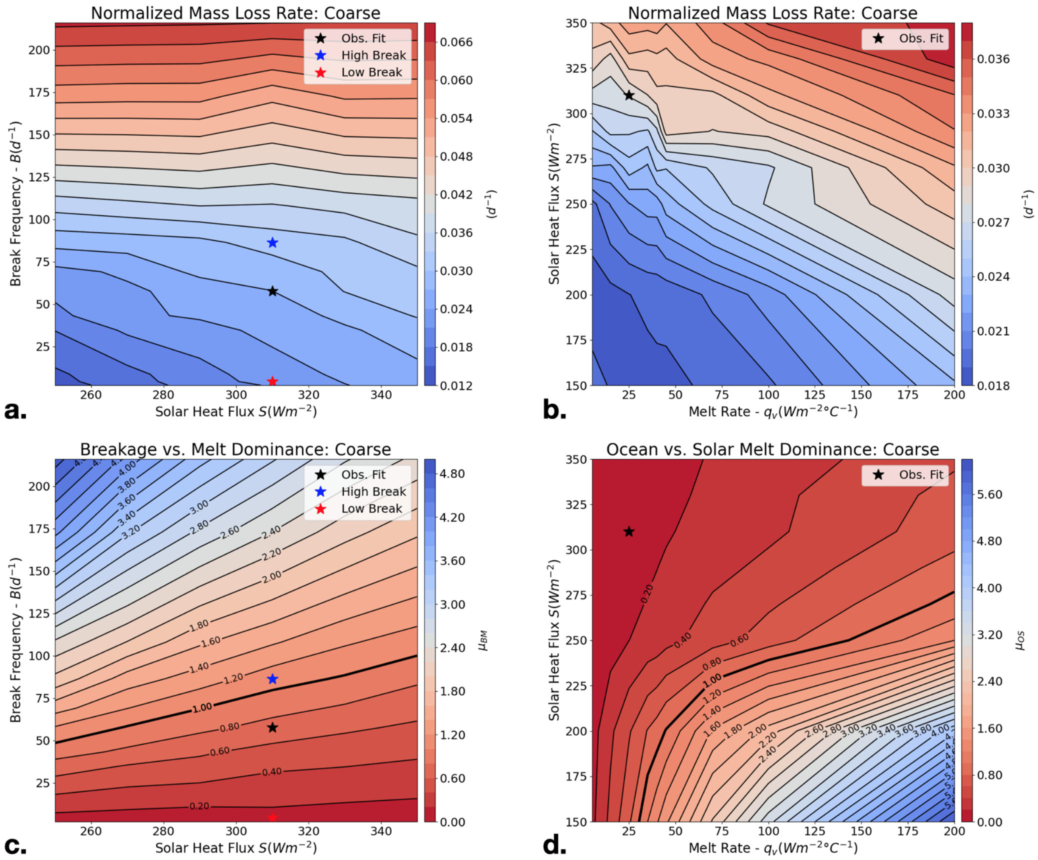

Figure 3.2: Normalized mass and breakage to melt ratio results. a. Sensitivity of the normalized mass loss rate for coarse floes evaluated over the simulation period (48 days), as a function of B and S, with q_v = 25 Wm^{-2}°C^{-1}. b. Same as in a. but for q_v and S, with B = 58 d^{-1}. c. Relative dominance of breakage versus melt in controlling loss of coarse floes, as expressed by μ_{BM} (Eq. (3.9)). The thicker contour with a value of 1.0 represents equal importance of breakage and melt processes. d. Relative importance of ocean versus solar melt in controlling melt loss, as expressed by μ_{OS} (Eq. (3.10)). Simulations for best fit to observations (black star, B = 58 d^{-1}), high break (blue star, B = 86 d^{-1}), and low break (red star, B = 2 d^{-1}) are included for reference, with q_v = 25 Wm^{-2}°C^{-1} and S = 310 Wm^{-2}.

Coarse, fine and total floe concentration losses

The concentration of coarse and fine floes display different behaviors. The coarse concentration loss rate tends to behave similarly to the coarse mass loss rate presented in the prior section, with the breakage rate B being a dominant factor in controlling both their behaviors. By contrast, the concentration of fine floes exhibits distinct sensitivity to q_v and B compared to coarse floes (Figure 3.3(b)). Increasing q_v results in faster loss, suggesting that vertical heat exchange is a significant rate limiting factor for melt at these smaller scales. Increasing B reduces the decline rate of fine floes. If breakage is more aggressive, more coarse floes decay beyond their size threshold and add mass to the fine floe population. The influence of B on fine floe concentration increases for large B and small q_v, and conversely the influence of q_v increases for large q_v and small B. In the vicinity of the best fit to observations, B and q_v have approximately equal impact on the evolution of fine floes. Since coarse floes tend to decay into fine floes, the fine floe concentration loss is inversely proportional to B.

The total sea ice concentration is the sum of coarse and fine floe concentrations, and combines their individual behaviors (Figure 3.3(c)). Increasing B and q_v result in an enhanced loss of total sea ice concentration, reflecting the important roles played by both breakage and melt in governing sea ice decline in the regimes spanned by the parameter sweep.

Selection of the best fit simulation to observations

The procedure employed to validate the performance of the LS-ICE model against observational data is detailed in (Moncada, Gupta, Thompson, & Andrade, 2023a). When appropriately calibrated, the model can emulate the evolution of resolved and unresolved floe concentration, mean sea ice thickness, mean mixed-layer temperature and floe size distribution exponent. We prioritize the fit to the resolved floe concentration loss rate ($\overline{\frac{dC}{dt}}$) and floe size distribution exponent evolution ($\frac{d\alpha}{dt}$), as those metrics are directly computed from satellite imagery, whereas others are derived from ocean reanalysis data or use average values (such as mass loss rate, which uses average thickness from reanalysis). The free parameters in the fitting procedure are the breakage frequency B and the vertical heat exchange coefficient q_v. Other parameters are fixed to standard values obtained from the literature (see (Moncada, Gupta, Thompson, & Andrade, 2023a)) and since S plays a more critical role in calibrating temperature, error was found using best fit $S = 310$ Wm^{-2}, which better captures average domain temperature of reanalysis data.

The sensitivity of $\overline{\frac{dC}{dt}}$ and $\frac{d\alpha}{dt}$ to B and q_v is presented in Figure 3.4. Range of q_v was zoomed in to the areas with the lowest errors. The root mean square error (RMSE) of these quantities with respect to the satellite observations shows a large sensitivity to B and a more minor dependence on q_v. The best fit for $\overline{\frac{dC}{dt}}$ is located at $B = 86$

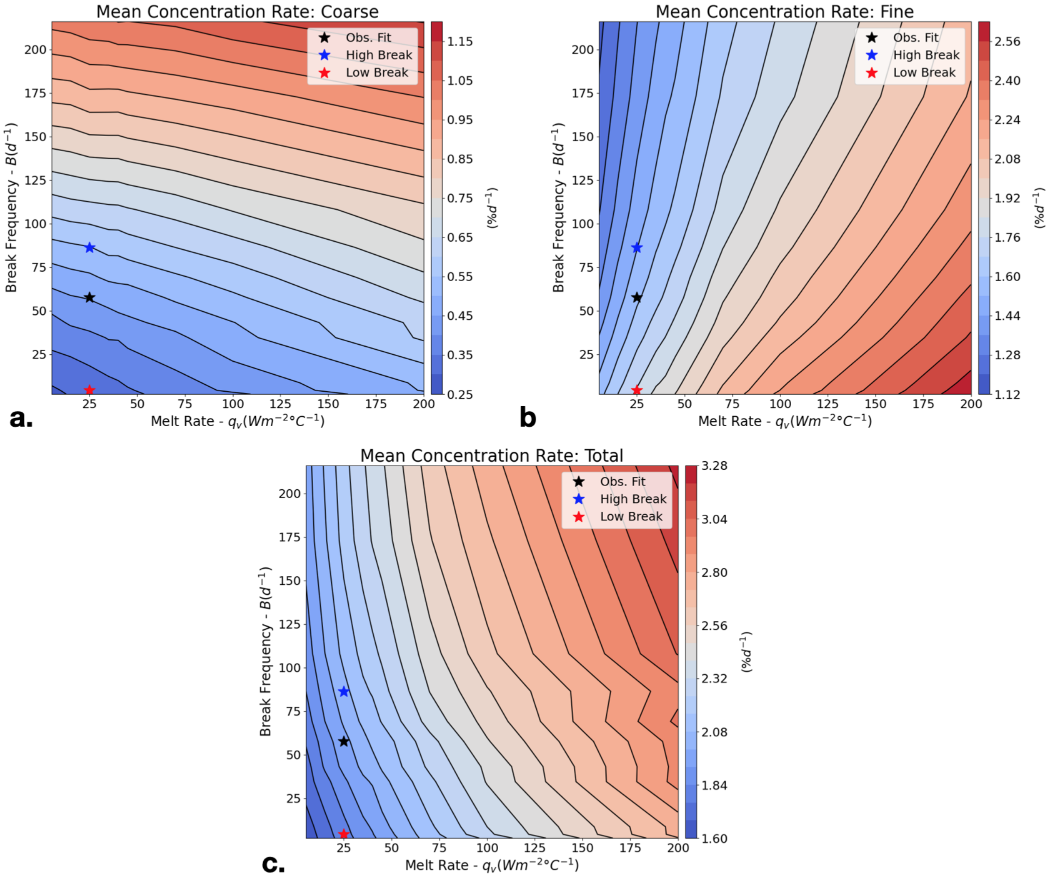

Figure 3.3: Mean rate of change or loss of sea ice concentration within the simulation period (48 days) for a. coarse, b. fine, and c. total floes, as a function of the B (breakage rate) and q_v (vertical heat exchange) parameters. Note how total concentration is the superposition of coarse and fine behavior.

d^{-1}, $q_v = 25$ Wm^{-2}°C^{-1}. For $\frac{d\alpha}{dt}$, there are several local minima, but the closest one to one best fit of $\overline{\frac{dC}{dt}}$ is at $B = 43.2$ d^{-1}, $q_v = 25$ Wm^{-2}°C^{-1}. As a compromise we choose an overall ‘best’ fit at $B = 58$ d^{-1}, $q_v = 25$ Wm^{-2}°C^{-1}, which produces a satisfactory evolution of both the sea ice concentration and FSD. More details on the FSD will be provided in the next sections. Regardless of the best fit choice, based on the error results presented, q_v is not very relevant, while B significantly increases or decreases the error. This suggests that while B is convenient for a sensitivity analysis, use of q_v should be examined more closely.

Comparison between years 2018 and 2020

The analysis presented in this work pertains to the year 2018, as that year has a satisfactory number of satellite images in the region of interest where floes can be

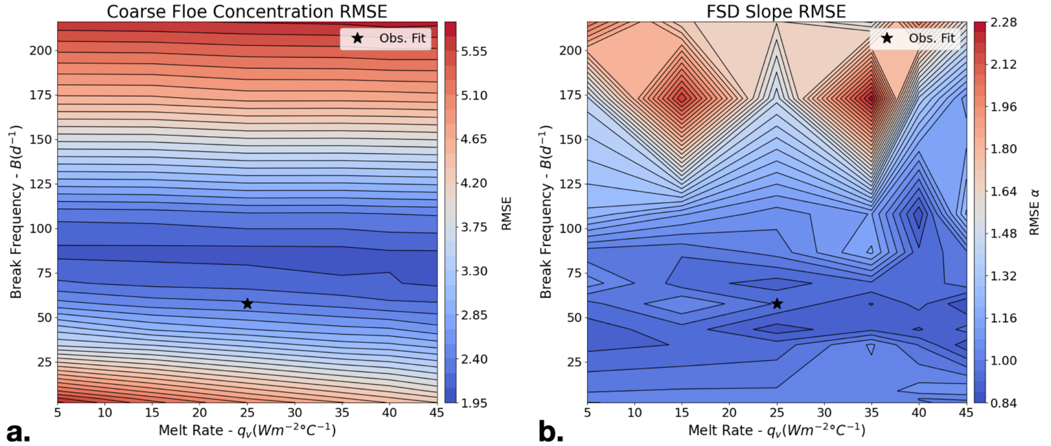

Figure 3.4: Root mean square between satellite observations and simulations for different B and q_v values: a. RMSE contours for Coarse Floe Concentration. b. RMSE contours for FSD Slope. Region shown is delimited to the B and q_v values shown since outside this range, error increases. Also $S = 310$ Wm^{-2}. The optimal value chosen was between the lowest error region of coarse floe concentration and FSD slope.

clearly identified. Here, we investigate the sensitivity of our results to this specific choice by repeating a subsection of the analysis for the year 2020. We select satellite images from a similar seasonal time period, namely June 4 to June 29 of 2020, compared to June 6 to July 24 in 2018. As detailed in (Moncada, Gupta, Thompson, & Andrade, 2023a), the model parameters optimized for the year 2018 can also emulate the year 2020 with reasonable RMSE values of the metrics of interest.

Figure 3.5(a) shows that the domain-mean temperature rises faster in 2020 compared to 2018. For example, in 2020 a temperature of 1 °C is reached in 20 days, while this takes about 35 days for 2018, both starting with very close initial temperatures. Figure 3.5(b) and (c) show that the initial mean sea ice thickness obtained from the observational dataset is thinner in 2020 than in 2018, but both years start with a similar concentration of resolved floes (about 20%). We quantify the relative importance of breakage versus melt through the parameter μ_{BM}. For both years, we find that both breakage and melt are active in the decline of the resolved floe mass, though melt plays a more dominant role in 2020 ($\mu_{BM} = 0.73$ in 2018 and $\mu_{BM} = 0.50$ in 2020, Figure 3.6). This larger importance of melt in 2020 is likely due to the faster ocean temperature rise that year, along with the the smaller initial sea ice thickness, which provides less opportunity for breakage processes to occur, before floes are either completely melted or unresolved by our model. Additionally, mixed layer depth was in average larger for 2018 than for 2020. We thus conclude that the initial environmental conditions have a strong influence on the behavior of the model and the relative importance of breakage and melt for sea ice decline; as faster temperature rise, inferior initial thickness and smaller mixed layer depth all contributed for 2020 to remove sea ice faster than 2018 via melt.

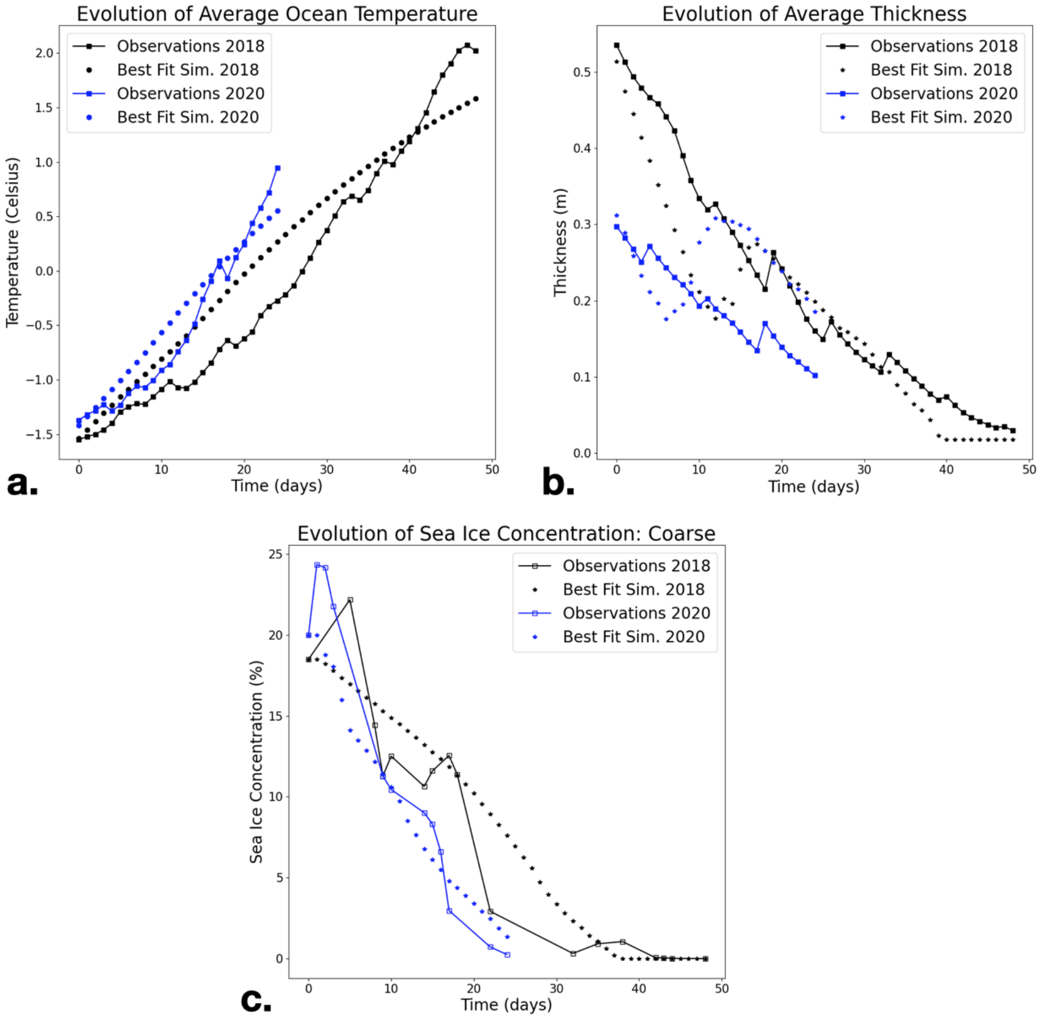

Figure 3.5: Comparison of 2018 and 2020 temperature, thickness and coarse concentration evolution. a. Mean temperature from observations and simulation results for 2018 and 2020. b. Mean thickness from observations and simulation results for 2018 and 2020. c. Coarse concentration from satellite observations and simulations for 2018 and 2020. Note the difference in number of days and initial temperature, thickness and concentrations between both years.

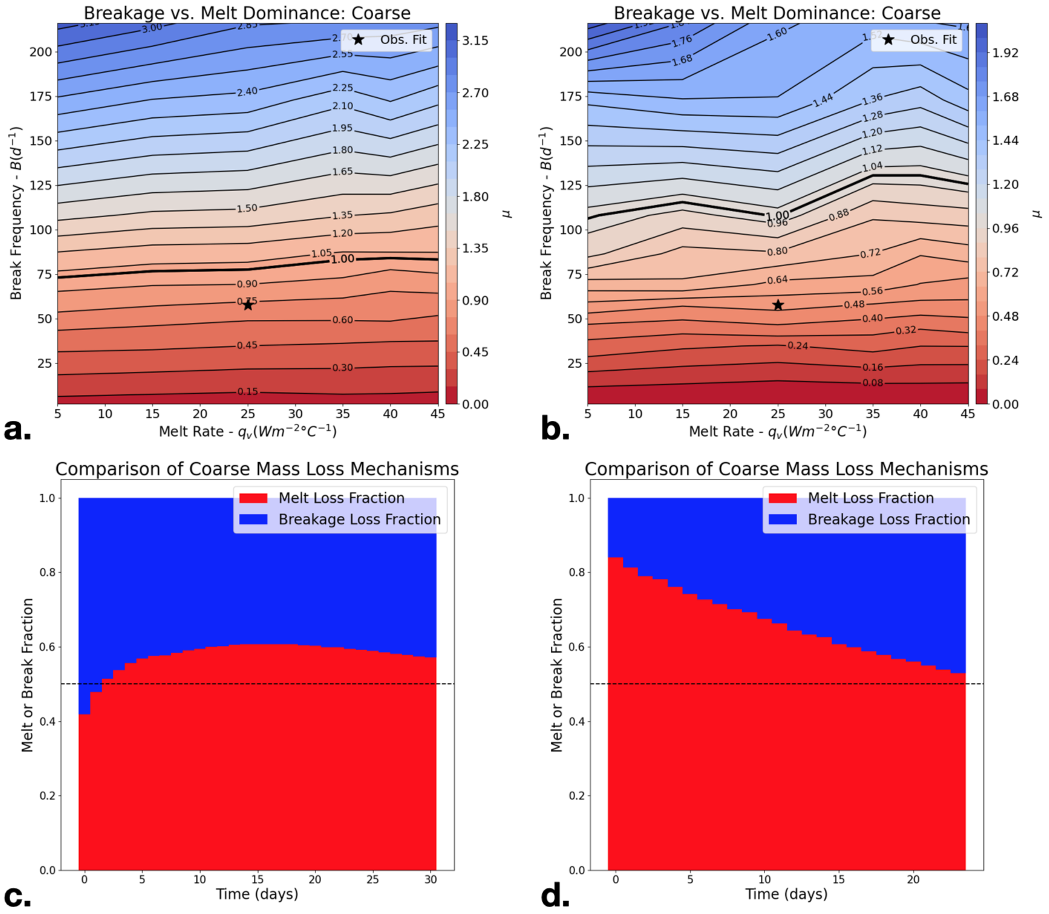

Figure 3.6: Comparison of 2018 and 2020 for μ_{BM} or break / melt ratio for coarse mass removal a. μ_{BM} results for 2018 with $\mu_{BM} = 0.73$ for best fit. b. μ_{BM} results for 2020 with $\mu_{BM} = 0.50$ for best fit. c. Melt loss versus breakage removal fraction relative dominance for 2018 for best fit results. d. Melt loss versus breakage removal fraction relative dominance for 2020 for best fit results.

Time scales for breakage and melt

To compare B, q_v and S using the same units, we define a time scale (in days) for breakage, oceanic melt and solar melt. We propose idealized mechanisms to estimate these time scales. To calculate an approximate time scale of ocean and solar melt we use q_v and S with respect to the thickness component, given that total thickness removal indicates complete floe melt. For oceanic melt:

$$\tau_{ocean} = \frac{\rho_i L_f \Delta h}{|\Delta T q_v|}, \tag{3.11}$$

where ρ_i is the density of sea ice, L_f its latent fusion heat, Δh is the average floe thickness and ΔT is the average difference between ice fusion temperature and ocean temperature. For solar melt:

$$\tau_{solar} = \frac{\rho_i L_f \Delta h}{|-S(1-a_i) + (A + BT_f)|}, \tag{3.12}$$

where a_i is a constant value of albedo for sea ice, T_f is the melting temperature of sea ice and A and B are atmospheric heat flux terms from (Moncada, Gupta, Thompson, & Andrade, 2023a). While breakage does not eliminate mass in itself, it does induce coarse floes to transition into fines, when reaching minimum coarse resolution. To calculate the time scale of breakage for this, we use the following formula:

$$\tau_{break} = \tau_{freq} N_s N_{floes}, \tag{3.13}$$

where $\tau_{freq} = \frac{1}{B}$, N_{floes} is the total number of floes and N_s is the estimated number of times a floe needs to split to reach the minimum threshold size assuming it always splits in half:

$$N_s = \frac{\ln(D_{mean}^2/D_{min}^2)}{\ln(2)}. \tag{3.14}$$

Values used to calculate ocean and solar melt time scales are ρ_i = 910 kgm^{-3}, L_f = 330000 Jkg^{-1}, Δh = 0.5 m, ΔT = 1.55 °C (assuming a mean ocean temperature of -0.25 °C and a sea ice melting point of T_f = -1.8 °C), a_i = 0.7, A = 70 Wm^{-2}, B = 10 Wm^{-2}, and S = 310 Wm^{-2} and q_v = 25 Wm^{-2}°C^{-1} from best fit. Values used for break time scale are: B = 58 d^{-1}, N_{floes} = 493, D_{mean} = 17.5 km and D_{min} = 2 km. Using these values, τ_{ocean} = 44.8 days, τ_{solar} = 42.4 days, while τ_{break} = 53.6 days, showing that both melt components and breakage occur at a similar order of magnitude. As a result, we can conclude that breakage and melt have similar time scales and the values used in this work are reasonable for comparing their sensitivity to sea ice loss.

3.4 Interactions of Breakage and Melt on the Floe Size Distribution

Floe size distribution indicators

We evaluate the floe size distribution (FSD) at a given time step as the number distribution of floes within the domain binned over characteristic sizes (Leppäranta, 2011). We define the size of a floe with arbitrary shape as the diameter of an equivalent disk with the same area as the original floe (Hwang et al., 2017; Montiel & Squire, 2017). We then characterize the floe size distribution using the cumulative number distribution of floes binned over their equivalent diameter. We fit a best line to this cumulative distribution expressed in log-log space (Figure 3.7), and extract its absolute value slope or exponential coefficient:

$$\beta = \frac{|\log N_{max} - \log N_{min}|}{|\log D_{max} - \log D_{min}|}, \tag{3.15}$$

where D_{max} is the size of the largest floe bin with floe number N_{max} and D_{min} is the size of the smallest floe bin with floe number N_{min}. As the largest floes are removed from the domain, we clip D_{max} to the largest bin size with $N_{max} > 1$, such that the flat parts of the cumulative floe number distribution is not included in the calculation of β. Following (Hwang et al., 2017), given that we are using cumulative floe number data, we then estimate the floe size distribution exponent as:

$$\alpha = \beta - 1 = \frac{|\log N_{max} - \log N_{min}|}{|\log D_{max} - \log D_{min}|} - 1. \tag{3.16}$$

Here, a higher value of α implies a bigger fraction of small floes compared to larger ones. This definition of FSD slope α will be the same applied in the next chapter of this thesis as well.

The primary importance of breakage for the loss of large sea ice floes and its interactions with melt can be further detailed by examining the evolution of the FSD throughout the summer. We evaluate the ‘log-log’ slope of the FSD (α); larger values of α represent a greater proportion of smaller floes.

The observed α from snapshots of satellite imagery shows a slight decline for the first 20 days of the data collection period, followed by a steep increase between days 20 and 30, and a final sharp decline between days 30 and 50, until all coarse floes have disappeared from the domain (Figure 3.8). The best fit model run (B = 58 d^{-1}) displays a comparable FSD evolution to observations, with weak changes in the first 30 days, a sharp increase between days 30 and 40, followed by a steep fall over the last days of the simulation. A ‘high breakage’ scenario (B = 86 d^{-1}) shows a steady and large increase in α during the first 35 days of the simulation, illustrating the effect of breakage in steepening the FSD profile. In contrast, a ‘low breakage’ case (B = 2 d^{-1}) displays a steady decline in α, which highlights the effect of melt in shoaling the FSD slope.

Additional sensitivity experiments varying the initial FSD reveal that model configurations starting with a greater fraction of large floes (small α) tend to be susceptible

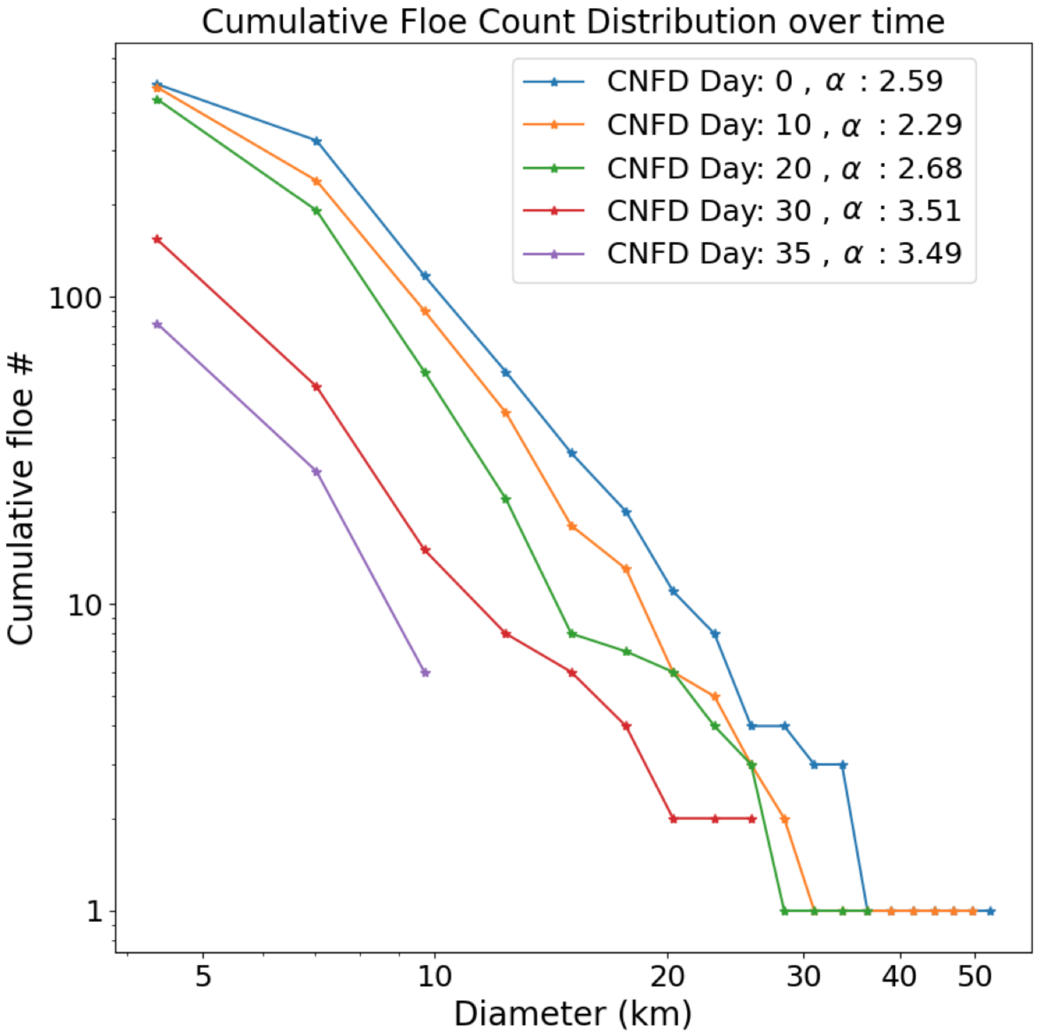

Figure 3.7: Cumulative Floe Number Distribution (CNFD) change over time and evolution of FSD slope α, for $B = 58$ d^{-1} and $q_v = 25$ Wm^{-2}°C^{-1}. Note how the cumulative floe number plot gets more steep or vertical as slope α increases.

to breakage and lead to sharp increases in α (Figure 3.9) as large floes split into smaller floes. This behavior is consistent with the removal of large floes depending heavily on breakage, as oceanic melt of large floes is limited by restricted access to warm waters. Repeating our analysis for the year 2020 reveals a stronger dominance of melt relative to 2018 (Figure 3.6), which is caused by thinner sea ice at the start of summer. We infer that the interplay between FSD, melt and breakage can evolve on inter-annual time scales and invites further investigation.

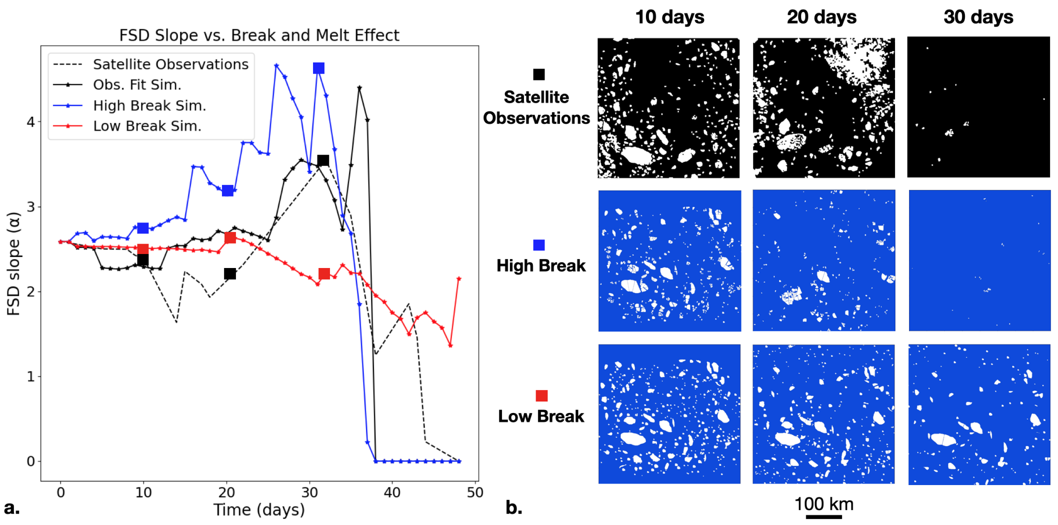

Figure 3.8: Effect on FSD: a. Evolution of the FSD coefficient α for the same best fit, high break and low break scenarios of Figure 3.2. The observed evolution of α is the dotted black line. b. Snapshots of coarse floes in processed images (top row), high break simulation (middle row) and low break simulation (bottom row).

Impact of the initial FSD Slope α

We explore the sensitivity of our results to the initial FSD by varying α at the start of the simulation, while keeping the same mean floe diameter and sea ice concentration (Figure 3.9 and 3.10). We find that the mean concentration loss rate of resolved floes increases (faster loss) with increasing α (larger fraction of small floes). This is because smaller floes are more susceptible to melt given their larger perimeter. Small floes also break beyond the 2 km threshold faster, which facilitates loss of resolved floes. This loss also explains how larger values of the initial α favors a larger μ_{BM} ratio (Figure 3.10), which reflects a greater importance of breakage versus melt when the initial sea ice state is composed of smaller floes. We thus conclude that the floe size distribution at the start of summer can play an important role in determining the time scale over which the pack melts. In essence, a higher α or more uniform distribution results in higher sea ice loss rates and melt dominance.

Floe net loss decomposition

Decomposing the floe count flux across spatial scales into melt and breakage components provides quantitative FSD insight, we can express count flux as:

$$\frac{df(D)}{dt} = M_G(D) - M_L(D) + B_G(D) - B_L(D), \tag{3.17}$$

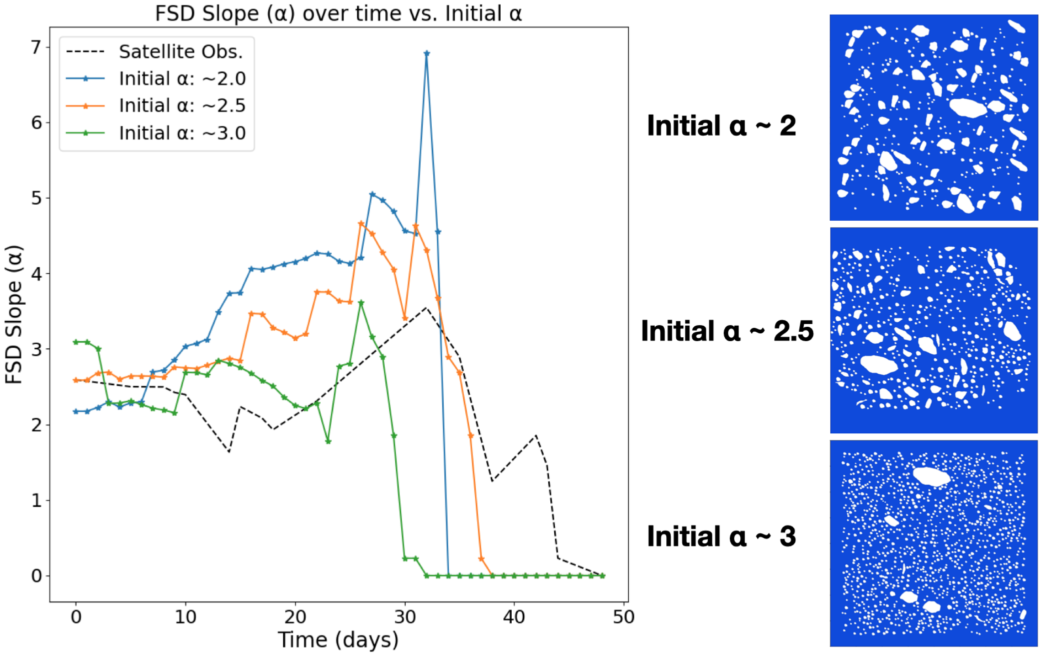

Figure 3.9: Effect of Initial α on FSD Slope change over time, snapshots of initial floe mosaics included for reference. Fixed forcing conditions are B = 86 d^{-1} and $q_v = 25\ \mathrm{Wm}^{-2}{}^{\circ}\mathrm{C}^{-1}$.

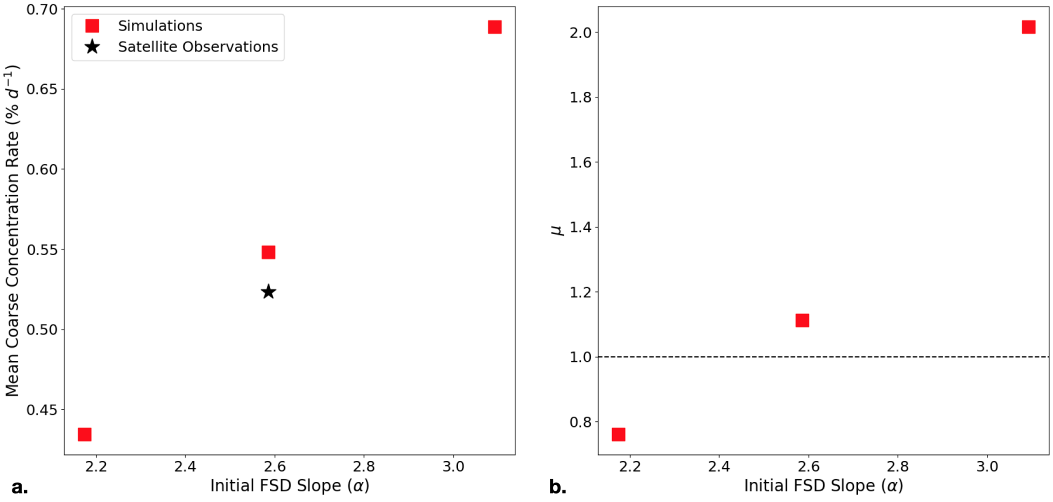

Figure 3.10: Effect of Initial α on a. Mean Concentration Loss Rate of Coarse floes and b. μ_{BM}. A higher initial α for the floe mosaic results in faster concentration loss for the same forcing conditions. It also results in breakage becoming the dominant loss mode for coarse floes instead of melt.

where $M_G(D)$ is the number of floes gained by a length scale (diameter D) associated with a specific bin size, $M_L(D)$ is the melt loss, $B_G(D)$ is breakage gain and $B_L(D)$ is breakage loss. We ignore floe formation processes due to freezing and collision merging as those are not represented in our simulations and are unlikely to be important during summer. The diagnosis of the terms in Eq. (3.17) are carried out online, such that processes acting to change lateral size of floes are parsed into the relevant terms. If a floe breaks into a piece whose size is smaller than the fine/coarse threshold (2 km), the original bin records a breakage loss, and the piece is discarded from the coarse FSD. As shown in Figure 3.11 d., FSD changes due to melt are mostly lateral rather than basal, since large floes (> 2 km) rarely melt in a spatially uniform manner.

Lateral versus basal melt effect on FSD

We estimate lateral versus basal melt contributions to the FSD trend (Eq. (3.17)), by assuming that the melt gain at a given bin size is equal to the lateral melt loss contribution from the bin that is immediately larger. Lateral melt occurs due to partial sections of floes reaching zero thickness and reducing floe area, while basal melt occurs due to the entire section of the floe reaching zero and eliminating the floe entirely. For floe count evolution, we find that lateral melt plays a dominant role over most floe sizes, while basal melt has a more limited effect in reducing floe count (Figure 3.11(d)). This matches the fact that larger floes tend to remain cooler in their center due to the reduction of albedo they induce, while only their edges reach higher temperature and undergo lateral melt. As basal melt requires the complete removal of the floe, this only happens for relatively smaller bins or for bins that were randomly assigned a lower thickness within the Gaussian initialization for thickness in the simulation.

When averaging the FSD decomposition terms between the days 3-40 of the best fit simulation (Figure 3.12(a)), we find a transition diameter d_{bm}=13.6 km: for scales larger than d_{bm} net breakage loss $(B_L(D) - B_G(D))$ dominates over net melt loss $(M_L(D) - M_G(D))$, and vice versa. This is consistent with our expectation that the largest floes are less affected by oceanic melt, as their under-ice temperature is often close to freezing.

The transition scale d_{bm} tends to increase as B decreases and as q_v increase. Both changes favor a faster breakage time scale relative to the melt time scale. Increasing B beyond $\approx 150\,\mathrm{d}^{-1}$ no longer modifies d_{bm}, which plateaus at approximately 10 km. The presence of this plateau is due to solar forcing, which plays a first order role in the melt of small floes, even for large breakage rates. The effect of solar melt can be negated by conducting simulations with low S values, which show that d_{bm}

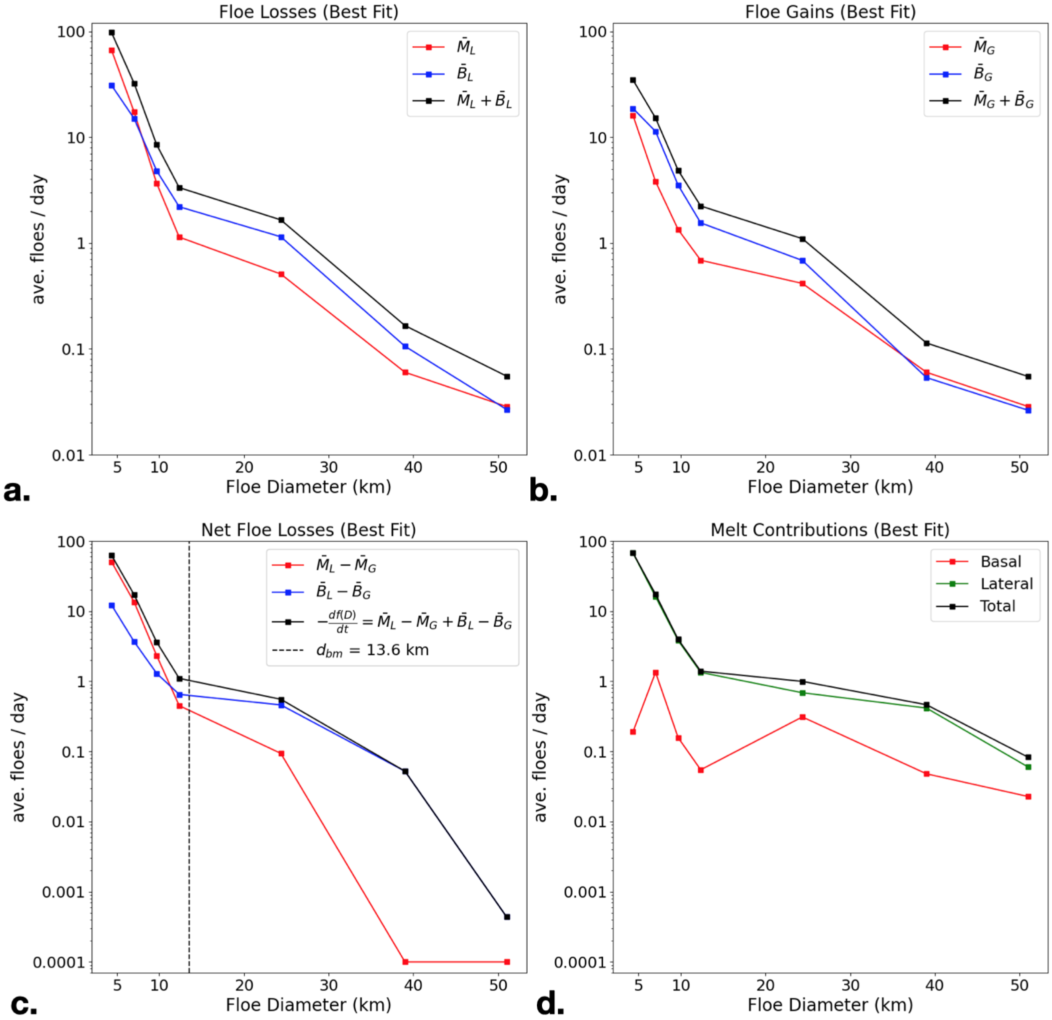

Figure 3.11: Decomposition of the FSD evolution expressed in Eq. (3.17) for the simulation with best fit to observations. Average contributions of the FSD evolution from a. loss terms, b. gain terms, c. net loss terms, and d. lateral versus basal melt contributions to loss. Calculations are carried over 7 bins between 2 to 50 km and time averaged between days 3 and 40.

decreases down to the fine/coarse floe threshold (2 km) for sufficiently large *B* (Figure 3.12(b)).

3.5 Discussion

This study leverages a discrete element model of sea ice floes (LS-ICE) to investigate processes controlling the spring-to-summer decline of sea ice in Baffin Bay in 2018. The model reproduces the statistical evolution of the pack (concentration, thickness, FSD and drift speeds), as observed from satellite imagery and reanalysis data (Moncada, Gupta, Thompson, & Andrade, 2023a). The parameter regime that

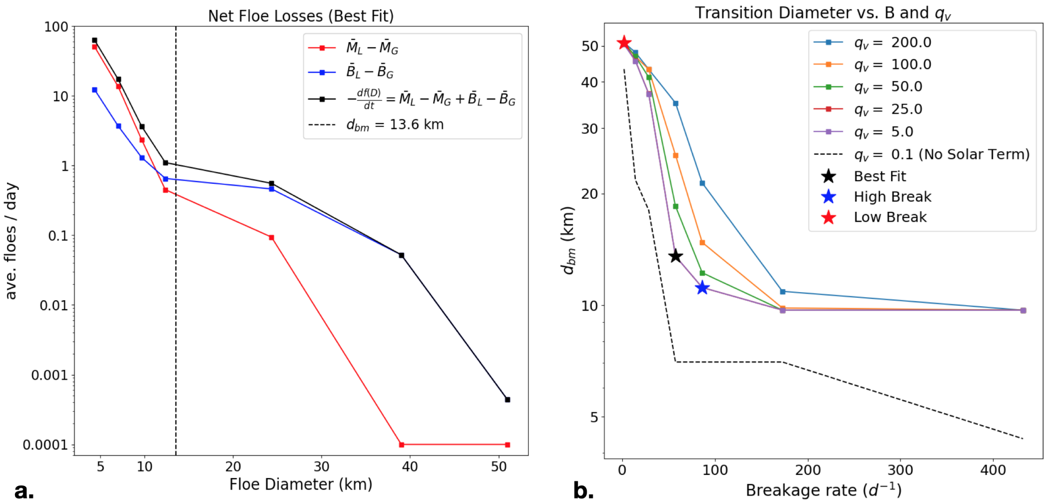

Figure 3.12: Information on transition diameter: a. FSD decomposition averaged over days 3–40, as expressed in Eq. (3.17), for best fit simulation. Calculations are carried over 7 bins ranging between 2 to 50 km, and are averaged over an ensemble of 20 members having random breakage sequences. For clarity, terms are clipped to a minimum value of 0.0001 floes/day. The dashed line indicates the transition diameter d_{bm} separating sizes controlled by breakage on the right and melt on the left. b. Sensitivity of d_{bm} to B and q_v, with all other parameters kept the same. The black dotted line represents simulations with no solar forcing. Lower d_{bm} indicates a stronger effect of breakage across sizes.

best fits the observed ice evolution reveals that breakage and melt play a comparably important role in governing the decline of resolved sea ice floes (> 2 km), with solar melt being more dominant than oceanic melt. Large floes are highly sensitive to the breakage rate B, but less sensitive to the heating parameters, solar forcing S and ice/ocean heat exchange coefficient q_v. Under certain regimes, breakage and melt compete for the fraction of sea ice loss they induce, while in all explored parameter regimes, solar and oceanic forcings have complementary effects on the decay of resolved floes (Figure 3.2).

Signatures of the distinctive impacts of breakage and melt are evident in the time evolution of the FSD slope, which steepens due to breakage at the end of May to early-mid June, and shoals due to melt towards the end of June, consistent with previous work (Denton & Timmermans, 2022; Hwang & Wang, 2022; Stern, Schweiger, Zhang, et al., 2018). A decomposition of the FSD trend for the best-fit simulation reveals that the number loss of floes with sizes above a threshold d_{bm} = 13.6 km is dominated by breakage, while it is regulated by lateral melt for floes smaller than d_{bm}. The inferred influence of lateral melt on kilometer-scale floes is aided by lateral transport of oceanic heat toward the center of individual floes (Gupta & Thompson, 2022a; Horvat et al., 2016), achieved by sea ice drift or ocean turbulence represented here by a constant eddy thermal diffusivity. The transition diameter d_{bm}, marking a regime shift between breakage and melt-dominated number loss, decreases with higher breakage rate, but does not decrease below 10 km in our simulations, due to the strong influence of solar melt.

More realistic representations of sea ice fragmentation, along with wave, ocean eddy and wind forcings, may better constrain the breakage and melt rate parameters prescribed in this study. The ocean's lateral diffusivity depends on eddy characteristics, which may vary with sea ice properties like floe size (Gupta & Thompson, 2022a) and concentration (Shrestha & Manucharyan, 2022). Breakage is also linked to thermodynamic melt, since thinner floes tend to fracture more readily. Understanding the effect of these coupled interactions on the sea ice decay regimes identified here will be a useful next step in refining parameterized representations of the FSD evolution for application to continuum models (Horvat & Tziperman, 2015; Roach et al., 2019). Our inferred balances between breakage and melt should also be tested in different regions, notably those with strong drift or bathymetric constraints, in both Arctic and Antarctic contexts. Elucidating these floe-scale mechanisms will provide better constraints and predictability on the future evolution of the sea ice pack, as environmental conditions continue changing.

Chapter 4

IMPACT OF OCEAN CURRENTS ON LANDFAST SEA ICE FRACTURE: BONDED DEM ANALYSIS

Moncada, R., Ulloa, J., Gupta, M., Thompson, A., & Andrade, J. (2024). Impact of ocean currents on landfast sea ice fracture: Bonded discrete element method analysis. *Computer Methods in Applied Mechanics and Engineering. In Preparation.*

4.1 Outline

Reproducing the fracture behavior of sea ice due to fluid forces is essential to simulate sea ice yearly cycle, as it determines when a particular floe or ice region breaks and the specific location and shape of the fractures. For example, at certain locations and periods, fast ice sheets split into larger, clean-cut floes, while in other regimes, they break down into several small floes, some close to a slurry (see Figure 4.1). As this breakage affects the geometry of the smaller floes that will then be split again and expose priorly isolated sea ice, this is a history-dependent process for which initial conditions critically affect the behavior of the system. In addition to the temporal and spatial evolution of geometry for future mechanical processes, geometry is also coupled to changing thermodynamic conditions affecting sea ice. For example, a region of fast ice breaking into fine and uniform fragments (see Figure 4.1 b.) will lose more mass by melt than one that breaks into larger and well-graded blocks (see Figure 4.1 a.). In turn, changes in sea ice geometry affect atmospheric and oceanic currents (Watkins et al., 2023; Willmes et al., 2023). Other factors that may combine with this effect of currents on different breakage FSDs are material properties and sea ice thickness. Figure 4.1 d. also shows the location of the complete sea ice sheet analyzed in the eddying currents Results section.

Eddies within the marginal ice zone play a critical role in fast ice breakage (Johannessen et al., 1987). However, these eddies can be very complex to describe and relate to breakage events. To simplify ocean currents, we initially propose using a single non-propagating (fixed) 1D idealized sinusoidal pulse for representation of horizontal ocean velocities, with a square ice sheet geometry. When using the term pulse we are referring to zones where horizontal ocean current velocities are stronger than its surroundings, with a unidirectional spatial variation resulting in tension. We use these pulse simulations to isolate the main aspects of breakage

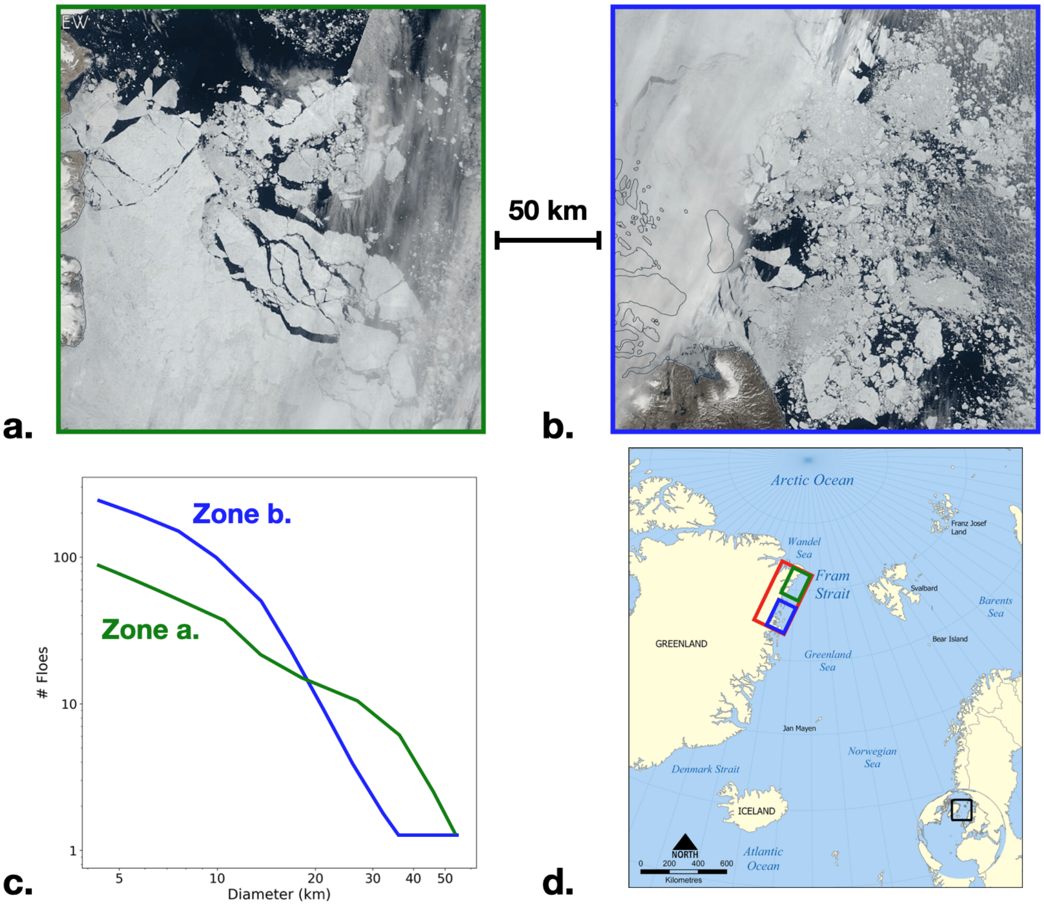

Figure 4.1: Different types of fast ice breakage regimes: a. Zone with larger, intact floes, b. Zone with small, severely degraded floes and slurry. The images are obtained from NASA MODIS snapshots of August 1, 2023, at Fram Strait. c. We show the cumulative floe count number distribution log-log plot FSD for both zones. Note how the FSD plot with more floes has a steeper curve, with many small sizes and very few large sizes, and the one with sharper cuts has less floes in total but more abundant larger objects. d. Location of both breakage zones in green and blue boxes, respectively, and location of the complete sea ice sheet (red box) with respect to Fram Strait analyzed using eddying currents (Einstein, 2023).

related to force wavelength and fracture time. We can then use single or multiple propagating pulses of horizontal velocity distributions to isolate the effects of pulse or perturbation propagation speed. That way, when we utilize more realistic eddying currents, the effects of wavelength, in particular, and other properties will be very straightforward to relate to breakage impact. For the pulse and eddying currents we choose to use an exposed fast ice sheet, only anchored at one of its extremes, as it would be the most appropriate for our objectives. Moreover, we use an arbitrary shape of Fram Strait for the eddying regimes, qualitatively replicating its breakdown.

Eddy size and velocity are suspected to play a dominant role in the FSD slope and size evolution of broken floes from the ice sheet (as seen in Figure 4.1).

This chapter will be organized as follows. An explanation of the rationale and tools used to simulate fast ice and its breakage is detailed in the 'Methods' section. After this, we present a section on the 'Analysis' of ocean currents and breakage length and time scales, taking advantage of idealized pulse currents. Then, in the 'Results' section, we include both setup and results of idealized pulse simulations, observational inferences (MODIS satellite image and reanalysis databases) and eddying current simulations that showcase the relationship between ocean current wavelength and sea ice sheet fracture. Finally, a 'Discussion' section regarding a comparison with observations, analysis of breakage, FSD relation to currents, and future work is presented.

4.2 Methods

Bonded particle method for sea ice fracture

Our bonded particle method (BPM) is based on a combination of LS-DEM (Kawamoto et al., 2016) with the BPM for LS-DEM of (Harmon et al., 2021). While our method has the capability of using arbitrarily shaped particles, for achieving computational tractability, we will employ circular disks in a hexagonal packing and fit this array within the bounds of a desired ice sheet geometry (Figure 4.2 b.). Bonds will be created among floes given a cohesive distance, using one bond for each applicable floe pair within that cohesive distance. Bonds are considered to behave as short beams undergoing tension, shear, and bending forces induced by inter-particle contacts and fluid currents. As inter-particle forces are further elaborated in (Harmon et al., 2021), we will concentrate on the effect of fluid currents inducing drag forces. For this chapter, we will assume our fluid forces are induced by ocean currents just underneath sea ice.

Figure 4.2 a. shows an arbitrary isolated pair of grains or floes under skin drag forces only. In this simple scenario, we can develop expressions relating the bond force $\mathbf{F}^{\text{bond}}$ to ocean currents in floes 1 and 2, denoted by $\mathbf{U}_1$ and $\mathbf{U}_2$, ocean skin drag forces denoted by $\mathbf{F}_1^{\text{drag}}$ and $\mathbf{F}_2^{\text{drag}}$, and the critical breakage force F^{cr}. To keep the analysis simple, we assume that bending moments do not exert significant bond forces and that the spaces left within the hexagon packing in Figure 4.2 b. are sufficiently small. The critical normal force on a bond is given in terms of a critical normal stress σ^{cr} and bond area $A^{\text{bond}} = 2\pi r^{\text{bond}} h$ by:

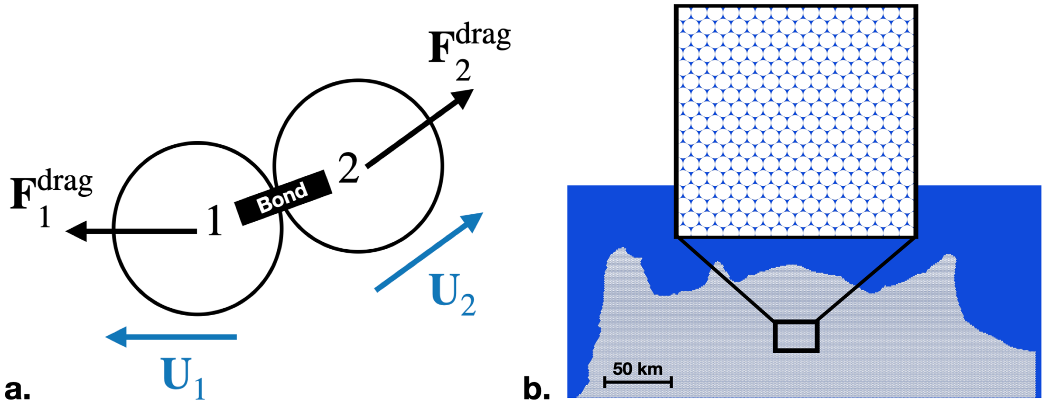

Figure 4.2: Application of BPM: a. Pair of floes joined by a bond. Relationship between the ocean currents $\mathbf{U}_1$ and $\mathbf{U}_2$ acting at each floe and respective drag forces at the floes. b. Example of arbitrary bonded floe sheet from Fram Strait, note hexagonal floe packing in the detail. Naturally, the large-scale behavior becomes more complex than in a single pair.

$$F^{\text{cr}} = \sigma^{\text{cr}} A^{\text{bond}}. \tag{4.1}$$

This critical force can be exceeded and the bond broken, if floe velocities $\mathbf{v}_1$ and $\mathbf{v}_2$ induce a relative velocity for which $|\mathbf{F}^{\text{bond}}| > F^{\text{cr}}$:

$$\mathbf{v}^{\text{rel}} = \mathbf{v}_1 - \mathbf{v}_2. \tag{4.2}$$

This relative velocity is necessary to find the relative displacement $\mathbf{v}^{\text{rel}}\Delta t$ used in the calculation of bond force incremental change (for contact bonding according to Harmon et. al 2021):

$$\Delta\mathbf{F}^{\text{bond}} = K^{\text{bond}}\mathbf{v}^{\text{rel}}\Delta t, \tag{4.3}$$

where $K^{\text{bond}} = \frac{EA^{\text{bond}}}{d^{\text{c}}}$ for which d^{c} is the cohesive length. We may use the increment in force to find the current force at time $t = t_{k+1}$:

$$\mathbf{F}_{k+1}^{\text{bond}} = \mathbf{F}_k^{\text{bond}} + \Delta\mathbf{F}^{\text{bond}} = \mathbf{F}_k^{\text{bond}} + K^{\text{bond}}\mathbf{v}^{\text{rel}}\Delta t. \tag{4.4}$$

Following (Herman, 2013) and other prior sea ice DEMs, the ocean drag force on a floe i for a constant unidirectional drag velocity $\mathbf{U}_i$ is defined by:

$$\mathbf{F}^{\text{drag}} = \rho^{\text{w}} A^{\text{floe}} C^{\text{hw}} |\mathbf{U}_i - \mathbf{v}_i| (\mathbf{U}_i - \mathbf{v}_i). \tag{4.5}$$

Assuming that $\beta = \rho^{\text{w}} A^{\text{floe}} C^{\text{hw}}$ is constant for all floes and that ocean drag velocity is much larger than floe velocity ($|\mathbf{U}_i| \gg |\mathbf{v}_i|$):

$$\mathbf{F}^{\text{drag}} \approx \beta |\mathbf{U}_i| (\mathbf{U}_i). \tag{4.6}$$

The time stepping of velocity based on the ocean current drag force reads

$$\mathbf{v}_{i,k+1} = \mathbf{v}_{i,k} + \frac{\mathbf{F}^{\text{drag}}}{m} \Delta t, \tag{4.7}$$

where global damping and other forces have been omitted. We may then express the velocity at time step $t = t_{k+1}$ as:

$$\mathbf{v}_{i,k+1} = \mathbf{v}_{i,k} + \frac{\beta |\mathbf{U}_i| (\mathbf{U}_i)}{m} \Delta t, \tag{4.8}$$

and the corresponding relative velocity as:

$$\mathbf{v}^{\text{rel}} = \mathbf{v}_{1,k} - \mathbf{v}_{2,k} + \beta \frac{|\mathbf{U}_1|(\mathbf{U}_1) - |\mathbf{U}_2|(\mathbf{U}_2)}{m} \Delta t. \tag{4.9}$$

Now, we can express the bond force in terms of the ocean currents acting at both floes, such that the relative velocity is dependent on ocean currents:

$$\mathbf{F}^{\text{bond}}_{k+1} = \mathbf{F}^{\text{bond}}_{k} + K^{\text{bond}} \mathbf{v}^{\text{rel}}(\mathbf{U}_1, \mathbf{U}_2) \Delta t. \tag{4.10}$$

Our condition for bond breakage will be the following:

$$|\mathbf{F}^{\text{bond}}_{k}| + K^{\text{bond}} |\mathbf{v}^{\text{rel}}(\mathbf{U}_1, \mathbf{U}_2)| \Delta t^2 - F^{\text{cr}} \leq 0, \tag{4.11}$$

or:

$$|\mathbf{F}^{\text{bond}}_{k}| + K^{\text{bond}} \Delta t^2 \left(|\mathbf{v}_{1,k} - \mathbf{v}_{2,k}| + \beta \frac{|(|\mathbf{U}_1|(\mathbf{U}_1) - |\mathbf{U}_2|(\mathbf{U}_2))|}{m} \right) - F^{\text{cr}} \leq 0. \tag{4.12}$$

For a more complete formulation, we can add global damping to these expressions. Global damping is often used in discrete element models to account for dissipative energy processes in the system, such as inelastic collisions, solid-fluid momentum exchange or inelastic deformations in bonds, all which remove energy from the system in ways not accounted by particle or bond elastic stresses. If global damping is defined as η and implemented in LS-DEM as in (Kawamoto et al., 2016), the equation for velocity update is the following (a more general form of Eq. (4.7)):

$$\mathbf{v}_{i,k+1} = \frac{1}{1 + 0.5\eta\Delta t}\left((1 - 0.5\eta\Delta t)\mathbf{v}_{i,k} + \frac{\mathbf{F}^{\text{drag}}}{m}\Delta t\right). \tag{4.13}$$

We can simplify this expression, as done above, by assuming a zero initial velocity and arrive at:

$$\mathbf{v}_{i,k+1} = \frac{2}{2 + \eta\Delta t}\left(\frac{\mathbf{F}^{\text{drag}}}{m}\Delta t\right). \tag{4.14}$$

With this expression for velocity, we can modify our equation for bond force, assuming an initial zero force:

$$F^{\text{bond}} = \frac{2}{2 + \eta\Delta t}K^{\text{bond}}\Delta t^2\left(\beta\frac{|(|\mathbf{U}_1|(\mathbf{U}_1) - |\mathbf{U}_2|(\mathbf{U}_2))|}{m}\right). \tag{4.15}$$

For sea ice sheet breakage the most relevant mechanical forcings will come from the conditions of ocean currents generating skin drag. Thus, the next section will present a relationship between breakage and ocean currents, that we can then examine in the Results section.

4.3 Analysis of Unidirectional Ocean Currents and Breakage

Ocean Velocity and Bond Forces

In this section we aim to establish a direct relation between ocean current characteristics and bond breakage, that we can then use for more realistic currents. For this purpose, we consider the following assumptions: initial floe velocities are close to zero, forces exist only in the x-direction, there is no damping, and there is a symmetric tension regime (see Figure 4.3). We will also simplify expression (4.12) by setting $(|\mathbf{U}_1|(\mathbf{U}_1) - |\mathbf{U}_2|(\mathbf{U}_2)) = \bar{\mathbf{U}}_{1-2}$, defining $\bar{\mathbf{x}} = |\mathbf{x}|\mathbf{x} = x^2$ (in velocity ^{2} units), to arrive at an expression for bond failure:

$$|\mathbf{F}_k^{\text{bond}}| + K^{\text{bond}}\Delta t^2\left(\beta\frac{|\bar{\mathbf{U}}_{1-2}|}{m}\right) - F^{\text{cr}} \leq 0, \tag{4.16}$$

and solve for a critical ocean current difference:

$$|\bar{\mathbf{U}}_{1-2}^{\text{cr}}| = \frac{F^{\text{cr}}m}{K^{\text{bond}}\Delta t^2\beta}. \tag{4.17}$$

If no prior bond force is involved ($|\mathbf{F}_k^{\text{bond}}| = 0$), the magnitude of bond force in terms of this ocean current difference is:

$$F^{\text{bond}} = K^{\text{bond}} \Delta t^2 \left(\beta \frac{|\bar{\mathbf{U}}_{1-2}|}{m} \right), \tag{4.18}$$

or, alternatively:

$$F^{\text{cr}} = K^{\text{bond}} \Delta t^2 \left(\beta \frac{|\bar{\mathbf{U}}_{1-2}^{\text{cr}}|}{m} \right). \tag{4.19}$$

For the simplest case where $\mathbf{U}_1 = (-\mathbf{U}, 0)$ and $\mathbf{U}_2 = (\mathbf{U}, 0)$:

$$F^{\text{bond}} = 2K^{\text{bond}} \Delta t^2 \left(\beta \frac{U^2}{m} \right). \tag{4.20}$$

However, to consider the potential effect of ocean current wavelength and period, which we can relate to breakage length and time scales, we introduce an idealized 1D distribution or sinusoidal pulse for oceanic currents with base magnitude or amplitude U_{o}:

$$\mathbf{U}(x) = (U_{\text{o}} \sin kx, 0), \tag{4.21}$$

where k is the wave number or inverse wavelength (λ) and for which:

$$|\bar{\mathbf{U}}_{1-2}| = U_{\text{o}}^2 (\sin^2 kx_1 - \sin^2 kx_2). \tag{4.22}$$

Then, we can express the bond force in terms of this sinusoidal current change over space:

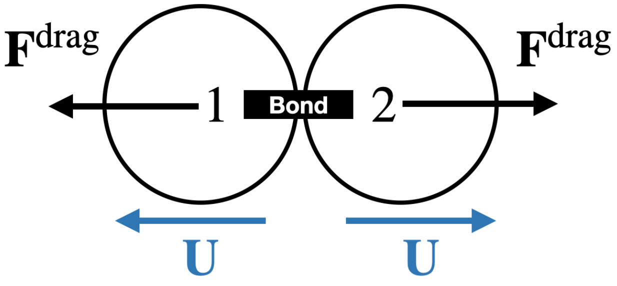

Figure 4.3: Simplified ocean current conditions on a floe pair.

$$F^{\mathrm{bond}} = K^{\mathrm{bond}} \Delta t^2 \left(\beta U_{\mathrm{o}}^2 \frac{(\sin^2 kx_1 - \sin^2 kx_2)}{m} \right). \tag{4.23}$$

Figure 4.4 shows an example of how bond forces can be affected by the shape of the ocean drag function, proportional to its corresponding $|\bar{\mathbf{U}}_{1-2}|$ for a fixed sinusoidal pulse (see first Results section). Then, if we assume $r^{\mathrm{bond}} = 1$ km, we can use the difference $\sin^2 kx_1 - \sin^2 kx_2$ as the finite-difference or gradient of the ocean current velocity (across r^{bond}). If we also suppose that the bonded floe distance is sufficiently small with respect to the total area of the sea ice sheet, we can gain insight into the shape of $|\bar{\mathbf{U}}_{1-2}|$ by using:

$$|\bar{\mathbf{U}}_{1-2}| \approx \frac{d\mathbf{U}(x)}{dx} = \frac{d(U_{\mathrm{o}}^2 \sin^2 kx)}{dx} = 2U_{\mathrm{o}}^2 k \sin kx \cos kx = U_{\mathrm{o}}^2 k \sin 2kx, \tag{4.24}$$

which is convenient, since the maximum difference of velocities among floes will develop at the locations of the maximum ocean current velocity gradient.

Breakage length scale

With the prior results and expressions, we can use the tension zones from the idealized velocity distributions to detect breakage regions or a breakage length scale l^{br}, across which all bonds will break or sea ice will fracture. To attain this, if we know the value of $|\bar{\mathbf{U}}_{1-2}^{\mathrm{cr}}|$, we can find the location where the critical ocean velocity difference results in breakage by solving for x^{cr} in Eq. (4.24):

$$x^{\mathrm{cr}} = \frac{1}{2k} \arcsin\left(\frac{|\bar{\mathbf{U}}_{1-2}^{\mathrm{cr}}|}{U_{\mathrm{o}}^2 k} \right). \tag{4.25}$$

To ensure a tension condition, it is necessary that x^{cr} is a point of positive slope for $|\bar{\mathbf{U}}_{1-2}|$. We can then define an expression for the breakage length scale by finding where the maximum value of $|\bar{\mathbf{U}}_{1-2}|$ is located, which will be at $x = \frac{n\pi}{4k}$ (for n = 1, 5, 9, . . .), and considering the symmetry with respect to this maximum value:

$$l^{\mathrm{br}} = 2\left(\frac{n\pi}{4k} - x^{\mathrm{cr}} \right) = 2\left(n\frac{\lambda}{8} - x^{\mathrm{cr}} \right). \tag{4.26}$$

Similarly, we can use $|\bar{\mathbf{U}}_{1-2}|$ to calculate F^{bond}, and comparing it to a constant F^{cr}, get the size and location of the region at which bonds will fail or where

$F^{\text{bond}}(x) > F^{\text{cr}}$ (refer to Figure 4.4 again), which converges to Eq. (4.26) when $r^{\text{bond}} \longrightarrow 0$. Furthermore, we can relate l^{br} and λ more explicitly using Eqs. (4.17), (4.25), and (4.26), in terms of material properties:

$$l^{\text{br}} = 2\left(n\frac{\lambda}{8} - \left[\frac{\lambda}{4\pi}\arcsin\left(\frac{\lambda F^{\text{cr}} m}{2\pi U_{\text{o}}^{2} K^{\text{bond}} \Delta t^{2} \beta}\right)\right]\right). \tag{4.27}$$

Figure 4.5 shows how the failure zone length l^{br} varies with λ and U_o for this expression for $n = 1$.

From the last two expressions above, it would appear that a pulse with a longer wavelength generates a larger region over which sea ice is able to break. This would result in short and very more concentrated pulses breaking absolutely all the ice in limited regions; while more spread and longer wavelength pulses will induce fracture over wider areas, perhaps breaking several, but not all bonds. Figure 4.5 shows this trend initially, and the Results section will elaborate more on these two different regimes. However, we need to emphasize that the expressions for the breakage length scale l^{br} are not monotonically increasing for all conditions, as there is a negative term involved. Indeed, we observe a cutoff length scale such that if the ocean velocity is weak enough and the wavelength is long enough, and in response to bond properties, breakage will be arrested, as Eq. (4.27) will start decreasing until it reaches zero again (see Figure 4.5). For Eq. (4.27) we can define $n = 1$ and $l_{br} = 0$, where $\lambda \neq 0$, to obtain a cutoff wavelength defined by:

$$\lambda_{\text{cut}} = \frac{2\pi U_{\text{o}}^{2} K^{\text{bond}} \Delta t^{2} \beta}{F^{\text{cr}} m}. \tag{4.28}$$

More importantly, the physical implication is that this cutoff length λ_{cut} will happen when an ocean current becomes too thinly spread over space. As a result, it will not generate sufficiently strong differential velocities or forces among the material and ice will not be fractured. In that sense Figure 4.5 and Figure 4.6 show how stronger current amplitudes delay this cutoff wavelength effect. A higher amplitude allows for failure to be more extensive thus, breaking a larger area of ice. Since the pulse is fixed, only its wavelength and amplitude influence its breakage length scale.

Breakage time scale

In addition to detecting the length scale of a region that will develop sea ice fracture, it is also convenient to understand how oceanic forcing may be related to initial breakage time. This is a way to a factor in aspects such as the wave speed or

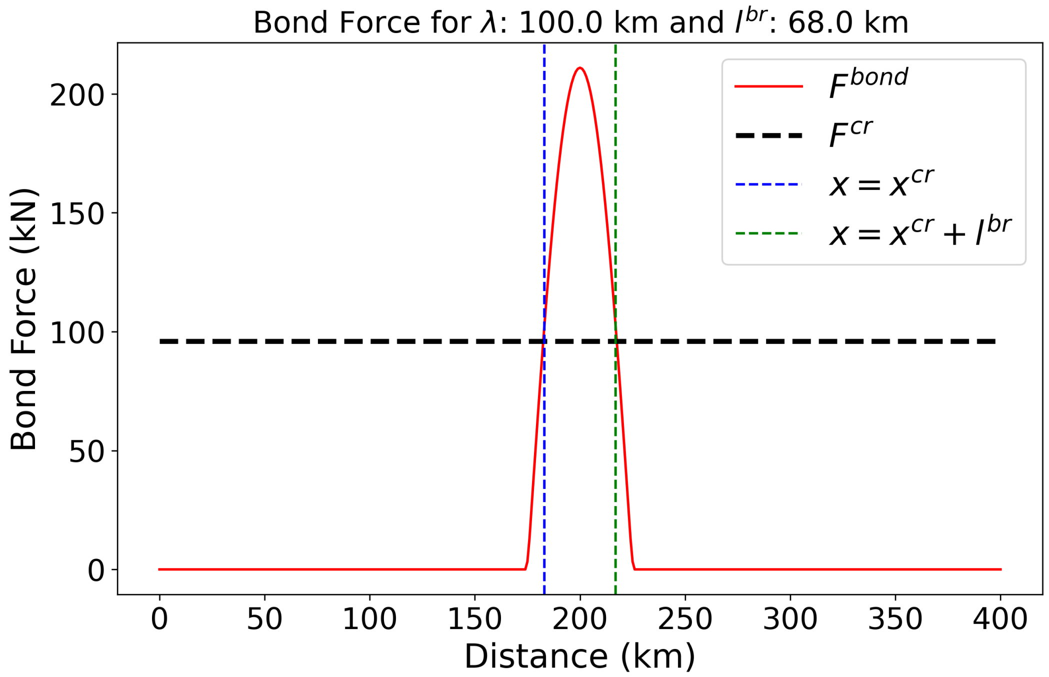

Figure 4.4: Example of bond force versus critical failure force for a single sinusoidal pulse of ocean velocity for $U_o = 0.03$ m/s. Material properties imported from Table 4.1.

propagation rate of perturbations evolving over time and also a method to measure the relative magnitude of ocean forces versus sea ice material properties. A direct manner to explore breakage time is by using expressions (4.18) and (4.20) for two floes, united by a single bond. We then proceed to solve for Δt as a critical time t^{cr}, by replacing F^{bond} with the critical bond force F^{cr}, for a fixed arbitrary regime:

$$t^{\text{cr}} = \Delta t = \sqrt{\frac{F^{\text{cr}} m}{K^{\text{bond}} \beta |\bar{\mathbf{U}}_{1-2}|}}, \tag{4.29}$$

and for a fixed infinitely sharp pulse located exactly at the contact between both floes:

$$t^{\text{cr}} = \Delta t = \sqrt{\frac{F^{\text{cr}} m}{2K^{\text{bond}} \beta U^2}}. \tag{4.30}$$

In both cases, the critical time is inversely proportional to the ocean current magnitude; stronger forces with respect to bond strength will result in faster breakage of bonds, while persistence of intact sea ice will indicate stronger material properties or weaker currents that need more time to accelerate floes up to the needed relative velocity. It is worth emphasizing that these equations apply only for fixed pulses in

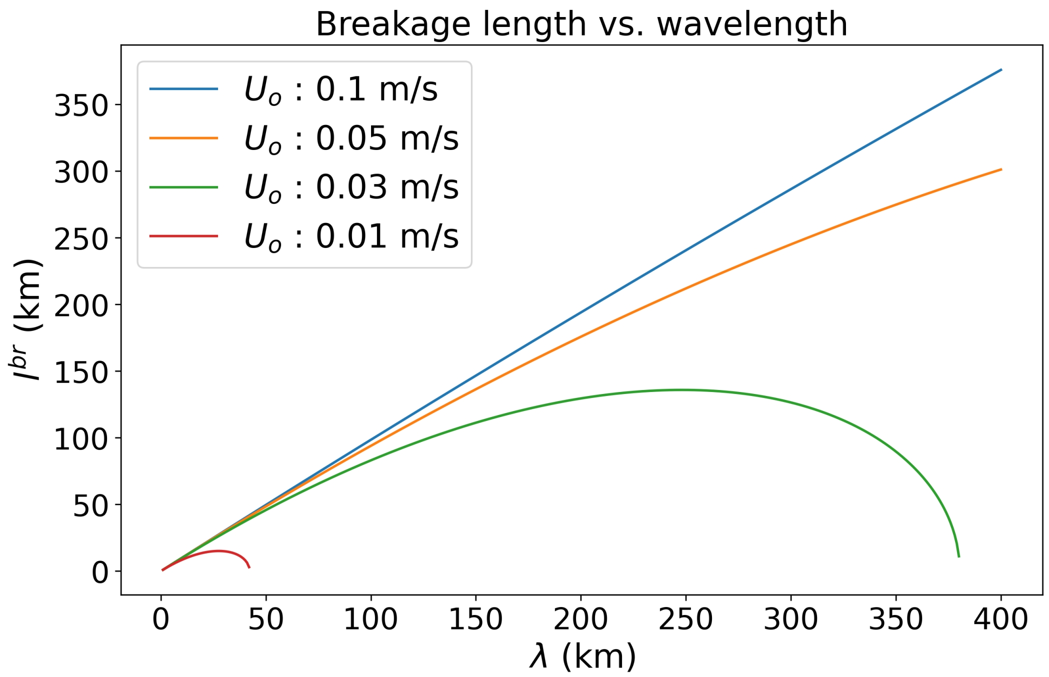

Figure 4.5: Plot of Eq. (4.27) of ocean velocity wavelength versus critical failure length. As the pulse becomes more diffuse or has a higher λ, the breakable length l_{br} tends to decay for a constant amplitude (in m/s). This implies that while sharper pulses have a small fail zone, very diffuse pulses will also be more limited in length than an optimal wavelength. Material properties imported from Table 4.1.

space and time (see results in Figure 4.9 b.). Propagating currents will be affected by additional factors and are not considered in this subsection.

We may also consider the effect of damping in the critical breakage time for the two-floe, single-bond system. Using the damping Eq. (4.15), replacing F^{bond} with F^{cr}, and numerically solving the non-linear equation, we obtain:

$$\frac{t^{\text{cr}}}{2/t^{\text{cr}} + \eta} = \frac{F^{\text{cr}} m}{2K^{\text{bond}} \beta |\bar{\mathbf{U}}_{1-2}|} \,. \tag{4.31}$$

The interplay between the critical breakage time, damping and multi-body effects will be crucial to explain the differences observed in breakage times in Figure 4.9 of the following section and the theoretical expressions above.

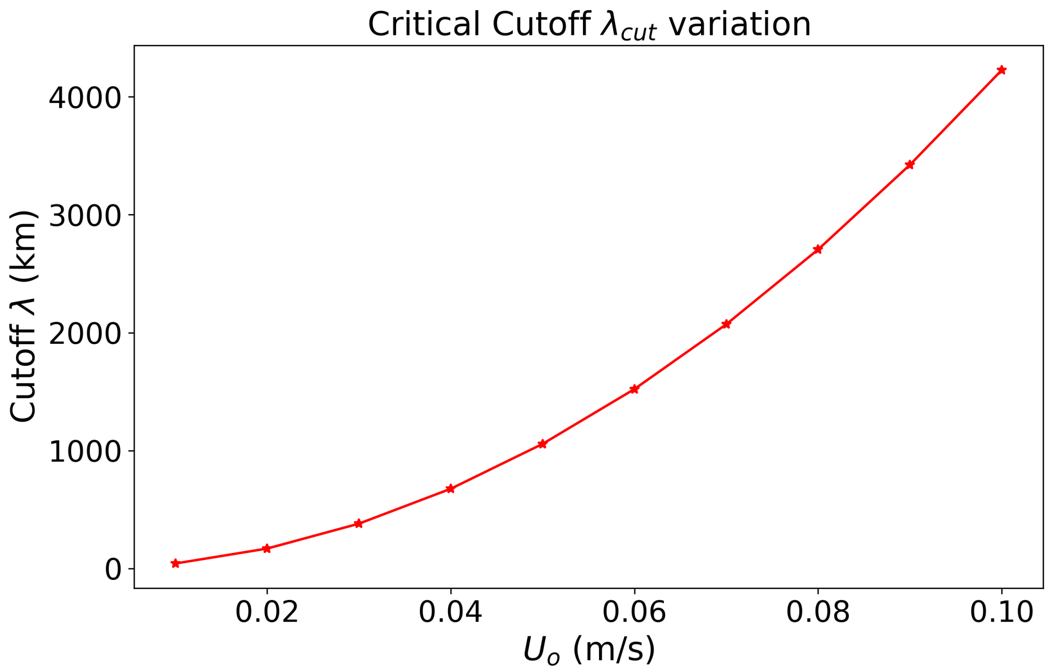

Figure 4.6: Variation of cutoff wavelength break scale in terms of the velocity amplitude by plotting Eq. 4.28.

4.4 Pulse Simulations

Setup of Pulse Simulations

We will start with simple-pulse, idealized conditions, with a 1-D variation in space, parallel to the principal axis of the sea ice sheet geometry. We choose the x coordinate as the longitudinal axis and the direction of spatial variation and propagation of these simple currents (all y values will be the same for a specific x value). The results obtained will be used to extract the fundamentals of ocean currents and the response of the sea ice sheet system.

Pulse currents will be described as variations of the expression (using a base speed amplitude U_o):

$$\mathbf{U}(x,t) = (U_\mathrm{o} \sin(kx - \omega t), 0), \tag{4.32}$$

with the values for k (wave number) ranging over $\frac{2\pi}{L}[1, 2, 4, 8, 16]$ km^{-1} for a reference length of $L = 400$ km. Wave number can also be expressed as an equivalent wavelength $\lambda = \frac{2\pi}{k}$ and the corresponding range of wavelengths is [400, 200, 100, 50, 25] km. We will define frequency ω in the range of $\frac{10\pi}{T}[1, 2, 4, 8, 16, 32]$ day^{-1}, for a reference time of $T = 50$ days.

The considered pulse scenarios (see Figure 4.7 for reference) include the following, where x^{ice} is the center of the ice sheet, $x^{\text{cen}}(t)$ is the shifting location of the center of symmetry of a propagating pulse or its y-intersect, and x^{λ} is one fourth of the total wavelength λ:

- Single fixed pulse:

$$\mathbf{U}(x,t) = \begin{cases} (U_o, 0) & \text{if } x < x^{\text{ice}} - x^{\lambda} \\ (U_o \sin k(x - x^{\text{ice}}), 0) & \text{if } x^{\text{ice}} - x^{\lambda} \leq x \leq x^{\text{ice}} + x^{\lambda} \\ (U_o, 0) & \text{if } x > x^{\text{ice}} + x^{\lambda} \end{cases} \tag{4.33}$$

- Single propagating pulse:

$$\mathbf{U}(x,t) = \begin{cases} (U_o, 0) & \text{if } x < x^{\text{cen}}(t) - x^{\lambda} \\ (U_o \sin k(x - x^{\text{cen}}(t)), 0) & \text{if } x^{\text{cen}}(t) - x^{\lambda} \leq x \leq x^{\text{cen}}(t) + x^{\lambda} \\ (U_o, 0) & \text{if } x > x^{\text{cen}}(t) + x^{\lambda} \end{cases} \tag{4.34}$$

- Multiple propagating pulses:

$$\mathbf{U}(x,t) = (U_o \sin(kx - \omega t), 0). \tag{4.35}$$

Table 4.1 presents the parameters chosen for these pulses. These parameters were tuned to allow computational times to be reasonable within a 16 multi-thread parallelization and results in the use of ‘synthetic’ 50 days. For single fixed and propagating pulse scenarios, a packet of ocean disturbance that generates tension within the ice sheet is exerted at a fixed location or shifted from left to right, respectively, on a 100 x 100 km square sheet. Multiple propagating pulses are applied to a 300 x 100 km rectangular sheet (Figure 4.7).

Results for Single Fixed Pulse

We first conduct a study using a single fixed pulse, which provides a convenient way to isolate the changes in breakage length in response to different forcing conditions, focusing on the effect of varying wavelengths. Figure 4.8 shows qualitatively the relation between wavelength and distribution of broken bonds for a single fixed pulse with amplitude $U_o = 0.05$ m/s. More diffuse pulses induce breakage over wider regions, while shorter pulses are concentrated in a more limited zone, almost as a perfect line. To qualitatively assess these observations, we also track the bond

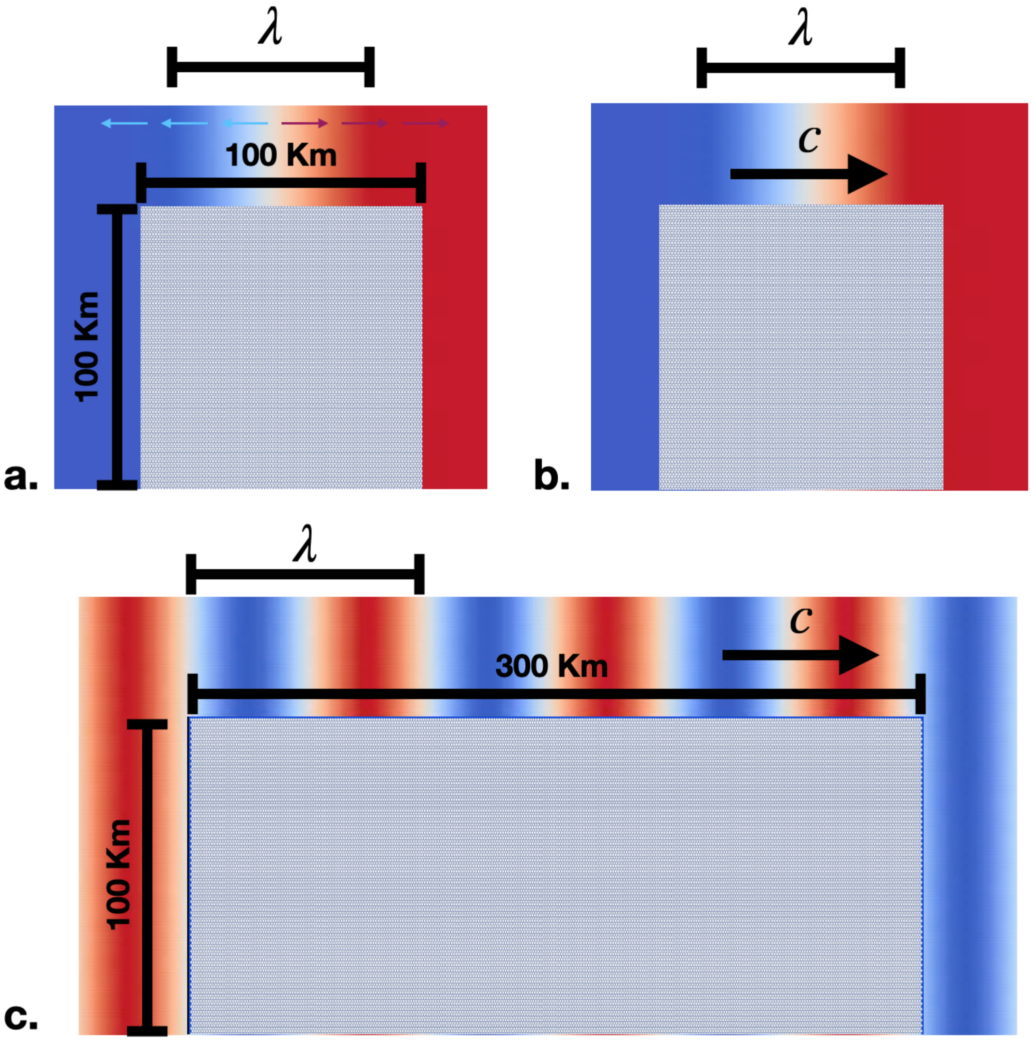

Figure 4.7: Example of pulse cases with a sinusoidal variation of ocean velocity: a. Single fixed pulse on a square ice sheet, b. Single propagating pulse on a square ice sheet of the same size as the fixed pulse, and c. Multiple propagating pulses on a rectangular ice sheet.

breakage evolution (Figure 4.9 a.) and analyze how it responds to wavelength. For a sharp fixed pulse, the regions under critical stresses are very small. Once breakage has developed in a narrow band, often in relatively short time, the remaining sheet remains fractured, as suggested by Eq. (4.27). In contrast, longer wavelength pulses produce fracture later, but given sufficient time, they have the capacity to break more floes than sharper pulses, as suggested in the Analysis section. Based on the results for 0.05 m/s in Figures 4.5 and 4.8, a wavelength of 25 km broke a similarly-sized band of 25 kilometers. On the other hand, a wavelength of 200 km resulted in widespread breakage of the whole 100 km wide square, but not with clean and

Table 4.1: Parameters for Numerical Simulations for Idealized Pulses

Variable	**Meaning**	**Value**	**Units**
K^{bond}	Bond Stiffness	6e9	N m^{-1}
σ^{cr}	Bond critical normal strength	240e6	Pa
η	Global damping	2	Ns m^{-1}
Δt	Time step size	1e-4	s
n^{steps}	Number of time steps	4,320,000	None
r^{floe}	Floe radius	0.5	km
d^{coh}	Cohesive distance	0.1	km
D^{s}	Ice tuning constant	Infinite	km
N^{floes}	Number of floes	Sq. 11,385 – Rec. 34,385	None
N^{bonds}	Number of bonds	Sq. 34,155 – Rec. 103,155	None
h^{ice}	Sea ice thickness	1.0	m

uninterrupted cuts as with a sharp pulse. Note that this value agrees reasonably with the $\approx$ 150 km fracture zone obtained from the λ vs. l^{br} plot in Figure 4.5.

Let us now address the possible existence of an optimal wavelength that produces a maximum number of broken bonds for a certain window of time (Figure 4.9 a.), similar to how some of the plots of Figure 4.5 reach a global maximum. If the wavelength is too sharp, it quickly makes a clean cut in a limited area and stops there. On the other hand, if the wavelength is too long, the region requires more time to develop fractures, implied by the effect of weaker relative velocities on Eq. (4.29). Stresses are then distributed more diffusely and, for extremely long wavelengths, fracture does not happen at all, which coincides with the findings of the Analysis section. Specifically, the energy of the pulse falls below a certain threshold and does not exceed the critical bond force (consider, for instance, an extremely flat pulse in Figure 4.4). Figure 4.9 a. shows this behavior for $\lambda = 400$ km, where breakage is entirely absent. This phenomenon also happens for propagating pulses but becomes more nuanced due to pulse propagation speed.

Concerning breakage time scales, Figure 4.9 a. shows that sharper pulses or smaller wavelengths induce breakage earlier in the material, until reaching a limit at $\lambda \approx 0$; also, increasing ocean current velocity amplitude will keep reducing breakage time (Figure 4.9 b.). We define this simulation breakage time as the simulation snapshot at which we identify the first bond breakage. Simulation breakage times are higher than our theoretical estimates, even when considering the effects of damping (Figure

4.9 b.). Including the damping term, the time for reaching critical stress or force can increase by about 10 - 15 % for moderate damping (≤ 2), but for a two-floe, single-bond system. If we compound the damping effect with a multi-floe and multi-bond system, this time is expected to increase even more when compared to the estimate from Eq. (4.29) and match simulation results.

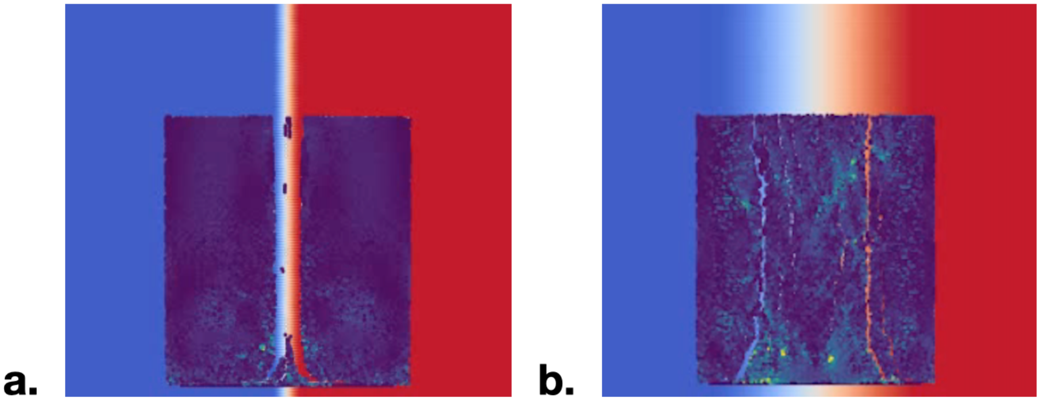

Figure 4.8: Effect of wavelength of a single fixed pulse for a. λ = 25 km and b. λ = 200 km. Observe the very different types of breakage regimes induced by pulse dispersion. A sharper pulse breaks in a focused area, but not beyond it, resulting in larger, clear-cut floes. A more diffuse pulse breaks ice across a more extensive region, sometimes partially, leading to many degraded floes and, often, a larger broken area.

Results for Single Propagating Pulse

For propagating pulses, similar to the fixed case, we can obtain breakage indicators such as the number of broken bonds or, conversely, the number of remaining bonds for an average period in the simulation, which we can normalize over the initial number of bonds to quantify a percent of remaining non-broken sea ice. We can also obtain the average diameter of floes (D_{mean}) or the power coefficient or slope α of the CFND of the sea ice sheet floe size distribution as it breaks into distinct floes. Lower values of mean diameter or percent of remaining bonds and higher values of α indicate a system that is more fractured or deteriorated.

For a single propagating pulse, Figure 4.10 shows the interplay between wavelength and wave propagation speed defined as $c = \frac{\omega}{k} = \omega\lambda$ and their impact on ice sheet properties averaged over the last 20 days of simulation. Based on variations found for mean diameter and remaining bonds in this $c - \lambda$ space, we find out that while wavelength can result in some local maxima conditions for breakage just like with

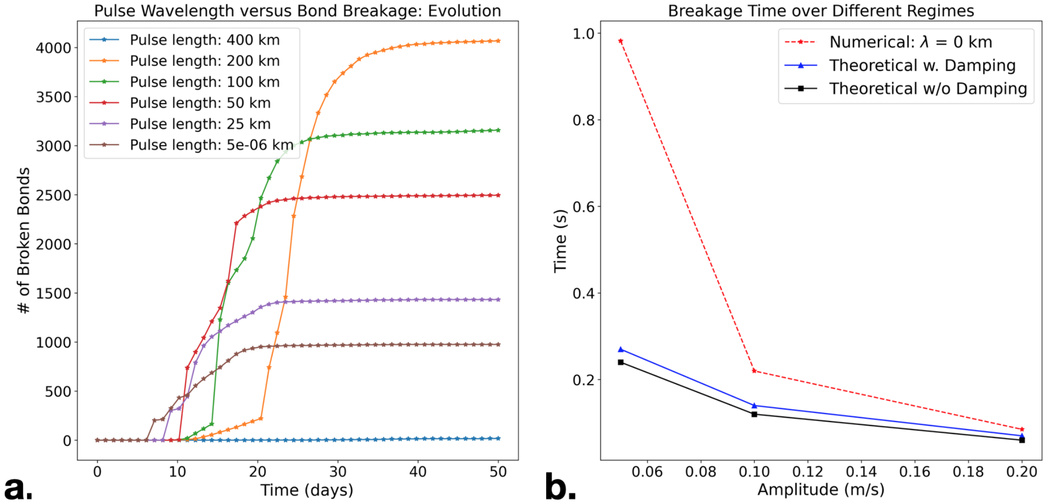

Figure 4.9: Bond breakage as a function of single fixed pulse wavelength: a. Evolution of Bond Breakage over time for different wavelengths. Note how bond breakage takes longer to start as wavelength increases, but ultimately leads to more broken bonds at the end of the simulation. This applies until a cutoff wavelength (in this case around 400 km) disperses force so much that no breakage occurs. b. Comparison of breakage time in response to pulse amplitude before reaching initial failure for both numerical and theoretical results, with and without global damping.

the fixed pulse scenario, there is an even more evident response for wave propagation speed.

Both Figure 4.10 a. (in particular) and b. display a wave speed band that maximizes the breakage of the sea ice bonded sheet and for which higher or lower values in the wave velocity axis would result in less intense fracturing. This vertical band, across wave speeds of 10 – 30 km/day for mean diameter and 30 – 50 km/day for percent of remaining bonds, suggests the existence of an optimal propagation speed for breakage. If the velocity is too slow, the pulse cannot propagate fast enough to affect a sufficiently large area of ice. If the velocity is too fast, the material does not have enough time to respond to the perturbation induced, and the tension forcing regime is not developed within the material. This is a result of the time that must elapse before failure occurs in fixed pulses as seen in the curves of Figure 4.9 a. and b. If the pulse is removed before this time elapses, the system cannot generate sufficient drag forces, since there is a delay to accelerate the sea ice mass as the ocean transfers its momentum. Therefore, an intermediate speed is what results in more broken sea ice.

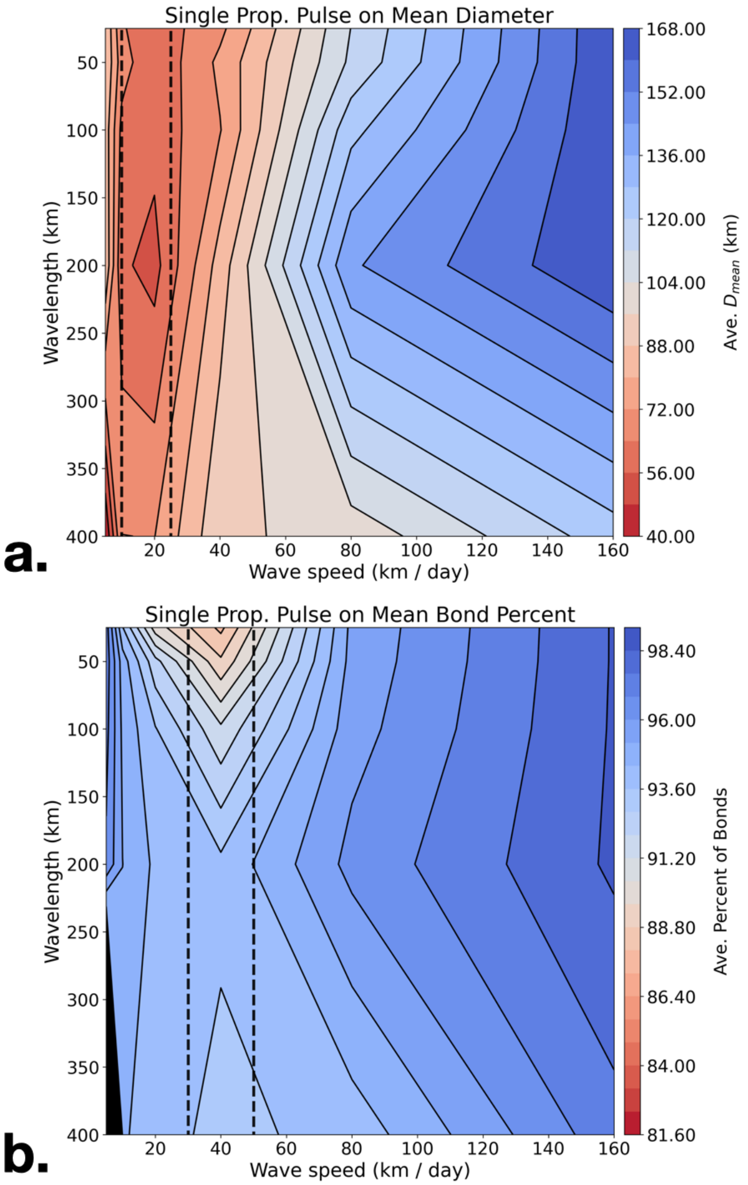

Figure 4.10: Phase space of wavelength (λ) vs. wave speed (c) for: a. Average mean diameter and b. Average percent of remaining bonds, with respect to initial number of bonds, for a single propagating pulse in a square. Note how minimum values of both sea ice metrics are reached along a particular wave propagation speed c range between 10 – 30 km/day for D_{mean} and 30 – 50 km/day for percent of remaining bonds, shown as a vertical band, bounded by dashed lines.

Results for Multiple Propagating Pulses

We consider an additional scenario to approach more realistic currents, using multiple propagating pulses that follow the ocean current distribution specified in Eq. (4.35). Interference among these pulses can lead to additional and faster breakage, but also to results that are more difficult to interpret. Thus, we will use the same parameters and FSD indicators as with the simple propagating pulse and explore how they are related in comparison. One modification that is required, though, is to switch from a wave speed vs. wavelength plot to a frequency vs. wave number ($\omega - k$) phase space instead, as shown in Figure 4.11, as this plotting space better displays minima for mean diameter and number of remaining bonds. With this change, we only need to convert the observed quantities into wave speed and wavelength units for a one-to-one comparison to the prior section. For multiple pulses, when reaching a particular range of wavelengths between 100 - 300 km, not too different from results of the single propagating pulse, breakage is maximized. This again shows that optimal wavelengths are present for both fixed and propagating scenarios. We will continue observing the influence of wavelength in the final Results section, as well. Nonetheless, the maximum breakage zones also respond to variations in frequency. We can apply the expression of $c = \frac{\omega}{k}$ and find out that propagation speeds of about 10 – 30 km / day roughly contain the inclined red areas observed in Figure 4.11 a. (more strongly) and b. These values are close to the observed behavior for the single propagating pulse. Therefore, while results are more complex, due to the presence of multiple pulses, and constructive interference might result in more intense breakage regions, we can identify certain ranges of wavelength and wave speeds that optimize breakage for multiple pulses too. This provides support that we can use similar FSD indicators for more realistic currents.

4.5 Observational Inferences

Observational Processing: MODIS and Reanalysis

Before presenting the eddying simulations on irregular sea ice sheets, we will present processing results from MODIS and re-analysis data necessary to understand in situ behavior better and to initialize this more realistic geometry. A region in Fram Strait, east of Greenland, was chosen as an example to extract an arbitrary fast ice shape, aiming to replicate its evolution in terms of area and FSD conditions. This section was observed for 2023, between the time sunlight is first available during winter for visualization of satellite images in this region, until ice sheet recovery was observed to begin at the beginning of fall. This is because we intend to study the breakdown process only, not refreezing. Precisely, this interval is between March 8, 2023, to September 25, 2023. Coordinates for the area are northwest: N 81.3127°, W 17.2138°; northeast: N 79.5774°, W 2.4093°; southwest: N 77.5627°, W 26.0052°; and southeast: N 76.3035°, W 14.0849°. For comparing more closely

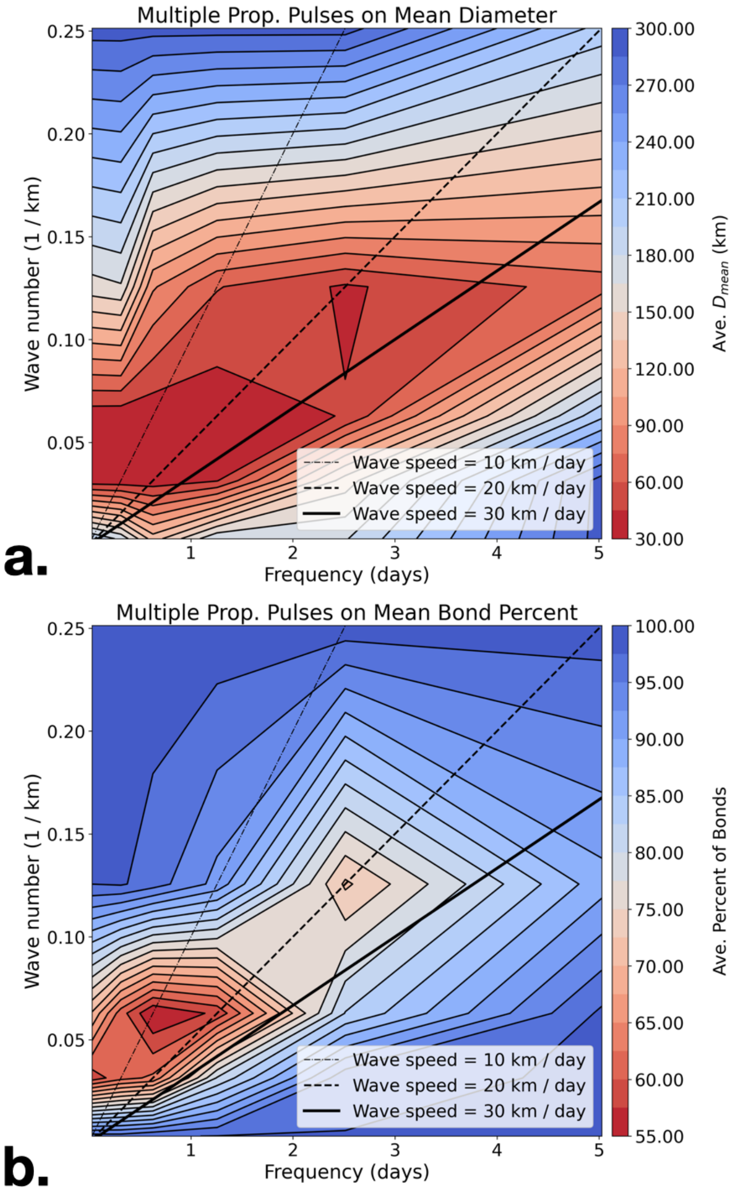

Figure 4.11: Phase space of wave number (k) vs. pulse frequency (ω) for: a. Average mean diameter and b. Average percent of remaining bonds with respect to initial state, for a multiple propagating pulses in a rectangle. Observe how minimum values of both sea ice indicators are located over a region equivalent to a wave propagation velocity c between 10 – 30 km/day, distributed as an inclined band.

to simulations we choose a more restricted period of continuous fast ice decay from July 13 to September 1, as before this period the ice sheet is very stable and after, some sea ice recovery starts occurring. Our main tools for observations are MODIS (Moderate Resolution Imaging Spectroradiometer) real color images, with a spatial resolution of 250 m and a temporal resolution of 1 day. Snapshots of MODIS from Terra and Aqua satellites were chosen depending on cloud cover in order to process them with less cloud cover. Figure 4.12 shows snapshots of major changes that can be appreciated for the ice sheet using MODIS images from an intact fast sea ice sheet to a completely decayed mass of small floes and fine slurry. Particularly for the snapshot of August 1, different kinds of floes are broken down, as described in the Introduction.

For a better understanding of the satellite images, we proceeded to obtain ocean velocity, ocean surface temperature, sea ice concentration, sea ice thickness, and snow thickness from the Copernicus Marine Database, with a spatial resolution of 12.5 km and temporal resolution of 1 day. Hence, most of this information was evaluated as a spatial mean evolving over time for the domain. Specifically, we used information from the Arctic Ocean Physics Analysis and Forecast reanalysis database for the same region and period.

Figure 4.12 shows the general trend of sea ice thickness reduction, which is also proportional to snow removal, temperature increase, and sea ice concentration decline during the summer transition. This figure also shows some major events observed in the MODIS snapshots underneath and how they are related to changes in sea ice thickness.

To go beyond a qualitative inspection of MODIS images, we apply a similar image processing methodology to (Moncada, Gupta, Thompson, & Andrade, 2023a) (see Figure 4.13) and proceeded to extract concentration, sea ice sheet area, floe size distribution, and cumulative floe number power law coefficient of critical snapshots over the period specified. These data will then be a reference for eddying simulation results in the next section.

Observational Results

By comparing observations of MODIS images with a time series of the reanalysis data, it was possible to observe certain trends in sea ice decline and life cycle:

1. Temperature increase is tied to a higher frequency of breakage events.
2. Changes in fast ice color are directly related to snow cover decrease and fast ice thinning.
3. In certain cases, increase in ocean velocity is correlated to breakage events. In others, ocean velocity is entirely unrelated.

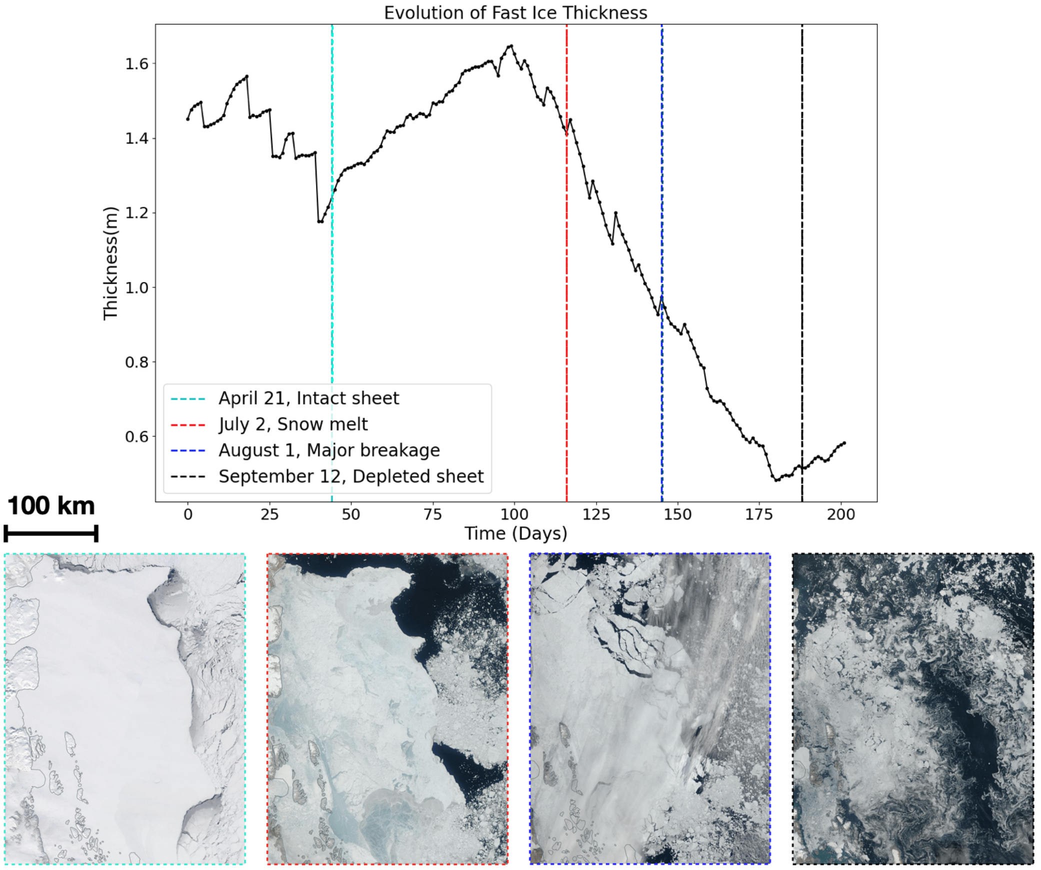

April 21 **July 2** **August 1** **September 12**

Figure 4.12: Copernicus Arctic reanalysis average data for sea ice thickness evolution over time with major regimes, with MODIS images framed by dashed lines indicating representative snapshots on April 21, July 2, August 1, and September 12 that summarize the main regimes experienced by the landfast sheet.

4. Thickness reduction is directly correlated to breakage events, periods of stability, and overall fast ice disintegration. Total collapse of the ice sheet only occurs below a thickness threshold.

5. Breakage mechanisms seem to be uneven across the ice sheet; in some places, large floes are formed, and in others only very fine. Both forcing and material properties may account for these differences.

6. Sea ice concentration is correlated to sea ice thickness.

7. Increase in sea ice thickness, concentration, and snow cover are all observed in the last chosen MODIS snapshots and the reanalysis data, indicating refreezing of the region.

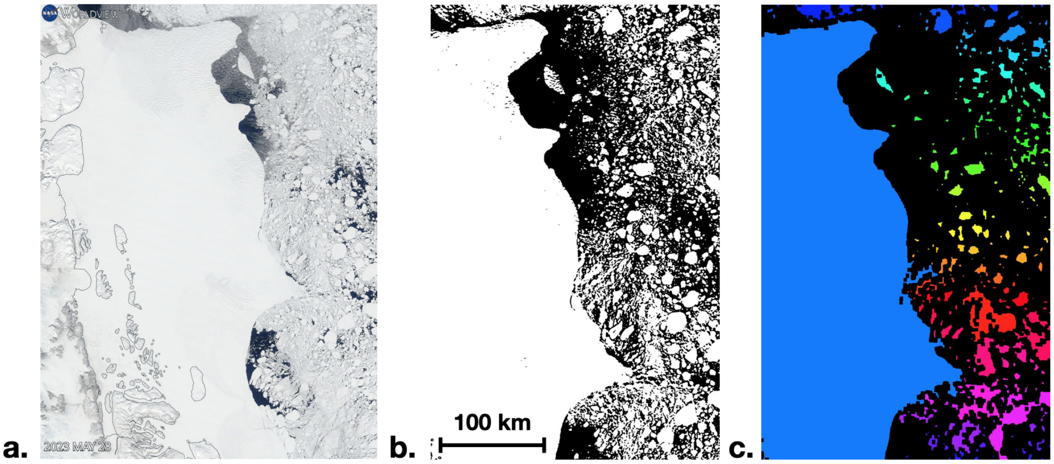

Figure 4.13: MODIS image processing sequence: a. original image, b. ice binarization, and c. floe segmentation

While we can argue that ocean currents developing at the ice sheet edges are associated with the localized breakage events after the ice starts thinning, breakage could also be facilitated by strong wind events from storms. However, the smaller scale of ocean currents compared to a larger scale of wind could result in the ocean currents having a stronger impact on spalling or edge failure (Manucharyan & Thompson, 2022; Timmermans & Marshall, 2020).

One of the main uncertainties in the development of the major collapse of the Fram Strait ice sheet is the uneven distribution of material and geometrical properties, including thickness. Our prior pulse simulations use an idealized homogeneous case for thickness (1 m) and bond strength. However, it is fairly clear from MODIS images, after the snow melt events, that the south extreme of the sheet failed early due to a relatively thinner ice (more translucent) than in the center or north of the sheet. Establishing whether this thinner region of the ice sheet was generated from spatial temperature variation in the atmosphere or ocean or was inherited from the prior winter season would require further study.

Data for sea ice concentration, FSD evolution at chosen snapshots, sea ice sheet area reduction and FSD slope changes are summarized in Figure 4.14. There is a trend of sea ice concentration and sheet area reduction. At the same time, there is a steepening of the FSD followed by flattening; that is, there is first an increase of the power coefficient, uniformity or slope of the FSD, followed by a decrease. These are characteristic responses of a process of initial breakage followed by melting of sea ice (Hwang & Wang, 2022; Moncada, Gupta, Thompson, & Andrade, 2023b).

Particularly, for the snapshot on August 1, 2023, there is an appreciable shift or jump in the FSD (compare prior FSDs in Figure 4.14 b.). Note how this trend starts reverting with increased melt by September 12 and less floes are present due to this melt. As fall and winter season approaches, snow and sea ice start recovering and the concentration of sea ice starts increasing at about the same time as it is observed in Copernicus data. All of these results match and summarize the trends explained above, but in a quantitative way.

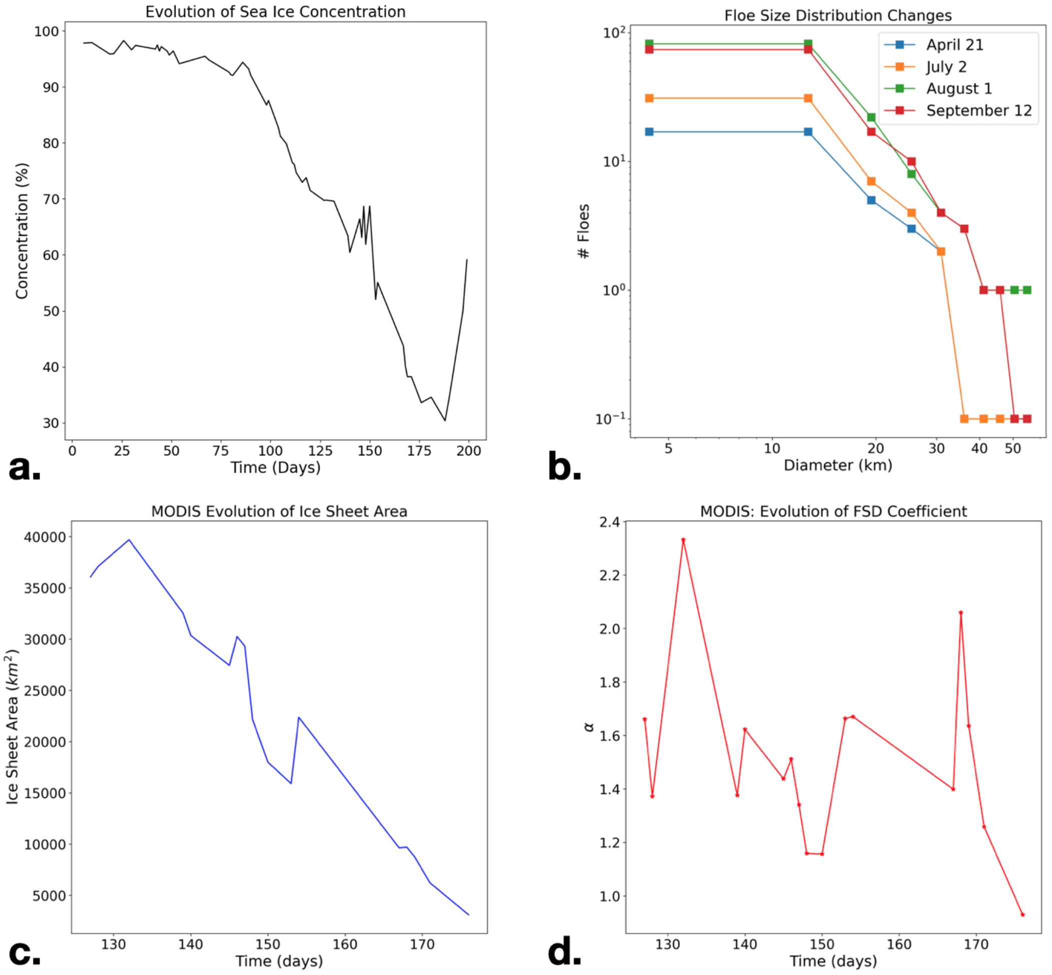

Figure 4.14: Image processing results for: a. sea ice concentration evolution for the whole breakage stage until the beginning of refreezing (March 8 – September 25) , b. FSD snaps over time related to visible changes in the fast ice sheet, exactly those shown in Figure 4.12, c. Sea ice sheet area reduction trends detected for the main failure period (July 13 – September 1) of observation and d. Variations in the floe size distribution power exponent α during the failure period, as well.

4.6 Eddying Currents Simulations

Setup of Eddying Currents Simulations

Eddying ocean currents will come from the `Oceananigans.jl` model (Ramadhan et al., 2020) based on the MITgcm (Adcroft et al., 2004). This is a three-dimensional fluid mechanics, thermally coupled, and geostrophic model that replicates geophysical ocean conditions. A set of initial conditions for temperature, salinity, and mixed ocean layer depth are specified to vary how diffuse or concentrated ocean vorticity or eddies are, in a way analogous to controlling the wave number k or wavelength λ in the simpler pulse cases.

For these more realistic currents, we also propose to use an irregular ice sheet setup. This irregular fast ice is based on a MODIS snapshot of Fram Strait from May 28, 2023, drawn into a CAD software to convert it to a polygon, then overlaid versus the hexagonal DEM packing to generate an arbitrary floe setup and, finally, rotated for simulation convenience (it can be observed in Figure 4.15 a. and b. and also shown in Figure 4.2 b.). We use the eddying currents of the following characteristics and the parameters and properties of Table 4.2:

- Diffuse eddy regime, moderate spread (Wavelength or eddy range: 30 – 150 km, average: 42 km) (Figure 4.15 a.);
- Sharp eddy/filament regime (Wavelength or thickness range: 5 – 20 km, average: 15 km) (Figure 4.15 b.).

Table 4.2: Parameters for Numerical Simulations for Eddying Currents

Variable	Meaning	Value	Units
K^{bond}	Bond Stiffness	6e9	N/m
σ^{cr}	Bond critical normal strength	240e6	Pa
η	Global damping	2	Ns/m
Δt	Time step size	1e-4	s
n^{steps}	Number of time steps	4,3200,000	None
r^{floe}	Floe radius	0.5	km
d^{coh}	Cohesive distance	0.1	km
D^{s}	Ice damping tuning constant	2.5	km
N^{floes}	Number of floes	31,454	None
N^{bonds}	Number of bonds	93,377	None
h^{ice}	Sea ice thickness	1.0	m

To further increase the realism of our eddying simulations we need to consider that, underneath sea ice sheets, ocean currents suffer significant damping. This is one of the main reasons spalling is observed in satellite images and why it is more prevalent than total fast ice collapse unless thickness is reduced significantly. To emulate sea ice damping of the ocean underneath the ice sheet and approximate this ocean-ice momentum exchange, we use the expression

$$\eta^{\text{ice}} = \exp\left(\frac{-d^{\text{edge}}}{D^{s}}\right), \tag{4.36}$$

to damp the ocean current velocity $\mathbf{U}$, where $\eta^{\text{ice}} \in [0, 1]$ is the damping coefficient responsible for reducing ocean currents. If a section of ice is not submerged, η^{ice} is simply equal to 1. Here, d^{edge} is the nearest distance of a specific ocean cell or grid point from the edge of the ice sheet or floe, and D^{s} is a tuning constant to regulate how horizontal ocean currents lose strength as the distance from the edge increases (set to 2.5 km based on observations, or to infinity if we assume no damping is present). In some cases, especially when the direction of ocean current loading and failure propagation is predictable, the geometry of d^{edge} can be simplified to a horizontal or vertical front from the mean location of the furthest ice edge of the portion of the material still connected to the fixed or fast zones of the sheet. We will use this front or simplified edge approach for the eddying currents to simplify computations and not apply damping underneath broken floes. Furthermore, we emphasize that the idealized pulse currents described in Sec. 4.4 were not damped.

Eddying currents results

For convenience, we continue using synthetic computational parameters to study the sensitivity of currents, just as specified in the above setup section (see Table 4.2). That is, we will then require to adjust time step size to fully represent geophysical times in a one-to-one ratio, rather than utilizing ‘synthetic’ days, which was not done due to restrictions in computational resources. From here onward, we will refer to the two eddying regimes described as *diffuse* and *sharp*. Aspects that are affected by different geophysical formulations include eddy filament size, temperatures, damping and coupling conditions with sea ice and the average velocity of eddies or angular velocity or Rossby Number. Hence, the wavelengths provided in the Eddying setup section are only approximations. While tuning pulse conditions is very straightforward, adjusting eddying current regimes to approach desired conditions is more difficult to control and choosing features such as wavelength is more restricted.

Figure 4.15 shows representative snapshots of both regimes applied to the irregular ice sheet configuration. Note that while eddy and filament size do change over time, they tend to stay within the specified wavelengths as explained below. For the diffuse regime, the sea ice sheet breaks over a larger area and into more floes than the sharp regime, to an extent where some sections of the ice sheet completely decay into individual floes similar to sea ice fines or slurry. The sharp regime also generates several floes but does not break as much area of the landfast sheet. While there are some differences, the sharp regime is closer to the clear-cut example in Figure 4.1 a., where there are not so many very small floes or fines, but mostly distinct coarse floes. On the other hand, the diffuse regime is more similar to Figure 4.1 b., where more small floes are present and also a significant amount of decayed fines. However, the diffuse regime also generated several coarse floes, which contrasts with this example. Regardless, comparing the FSDs shown in Figure 4.1 and the FSDs in Figure 4.17 d., indeed shows that the diffuse regime approaches the broken down case and the sharp regime is closer to more coarse floe cut example. Observe that, for both regimes, using ice damping results in a similar spalling or edge failure behavior as that of observations, confirming the need for sea ice damping in the model. Without this damping addition, the entire sheet would start failing from the very beginning and the progression of breakage from edge towards the interior could not be replicated.

Hence, for these two regimes, we observe different breakage and FSD behaviors in response to the spatial variation of the currents. For example, diffuse eddies qualitatively approximate observations better than sharp filaments. Even then, there is a critical point where sea ice breaks more thoroughly in observations than in the eddying simulations, perhaps due to the need of a longer wavelength. To validate the impact of wavelength, Figure 4.16 a. presents the average maximum vorticity magnitude or Rossby number (the ratio of inertial versus Coriolis forces, normalized with respect to the maximum vorticity of the domain for each snapshot) over time for both cases and how they have similar values. But, sharp filaments tend to have a stronger vorticity or velocity magnitude than diffuse eddies, while resulting in less breakage of the ice sheet. Maximum kinetic energy of the domain also behaves similarly and sharp filaments having higher values than diffuse eddies. Thus, we again confirm the vital role of eddy spatial distribution or wavelength effect on sea ice fracture. This is because higher vorticity, kinetic energy or ocean velocity alone might not necessarily result in more breakage.

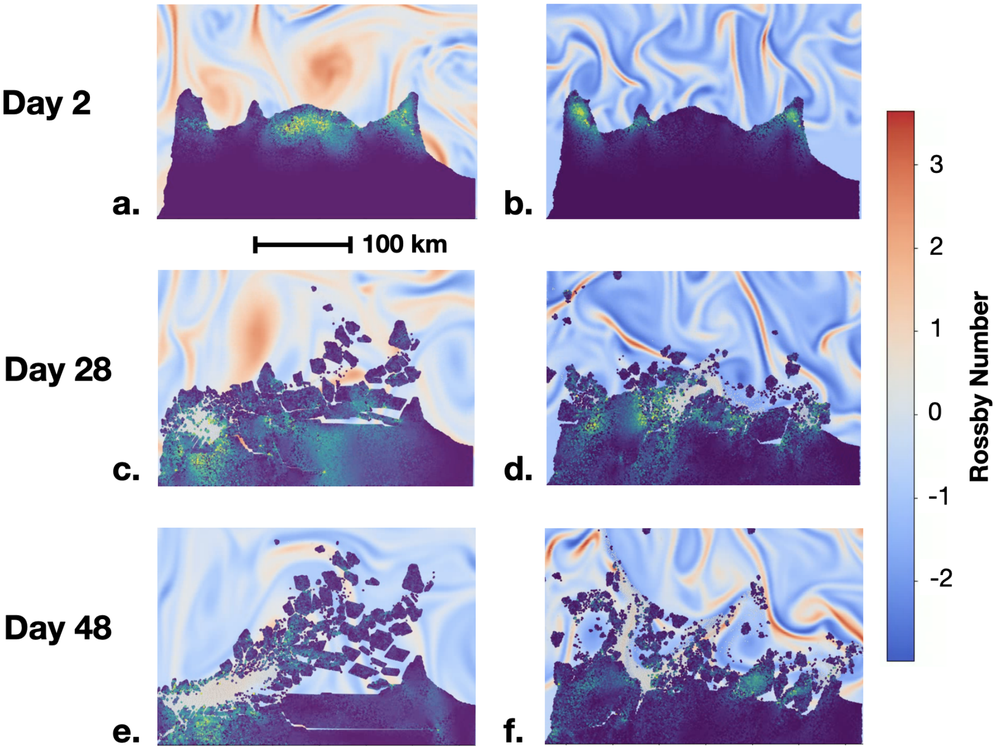

Figure 4.15: Snapshots of diffuse current regime on the Fram Strait sheet at the a. beginning: Day 2, c. middle: Day 28, and e. end of failure: Day 48. Snapshots of sharp current regime on Fram Strait sheet at the b. beginning: Day 2, d. middle: Day 28, and f. end of failure: Day 48. Stronger normal stress is highlighted in brighter colors. The broken-down slurry is emulated by non-bonded white floes. A reference scale for the heat map of vorticity or normalized Rossby number is also provided.

To further elucidate this point we can refer to Figures 4.16 b. and c. The evolution of weighted average wavelength obtained from the radial kinetic energy wave number (or KEK) spectrum combining x and y ocean current velocities is presented in Figure 4.16 b. It is evident that diffuse eddies consistently keep a longer average wavelength than the sharp filaments for all the simulation period and that both regimes do not change their wavelengths drastically. While maximum values are stronger for sharp filaments, the average kinetic energy of the domain is very similar for both current regimes. Note that Figure 4.16 c. shows that the more diffuse eddies contain slightly more kinetic energy for the entire domain, but overall diffuse and sharps regimes converge to a similar average value. Therefore, for most of the simulation the sharp filament regime contains higher kinetic energy maxima and similar mean kinetic energy compared to diffuse eddies. Nonetheless, as expected from our pulse results, the diffuse eddies having more reach due to their longer wavelength results in them ultimately breaking more ice.

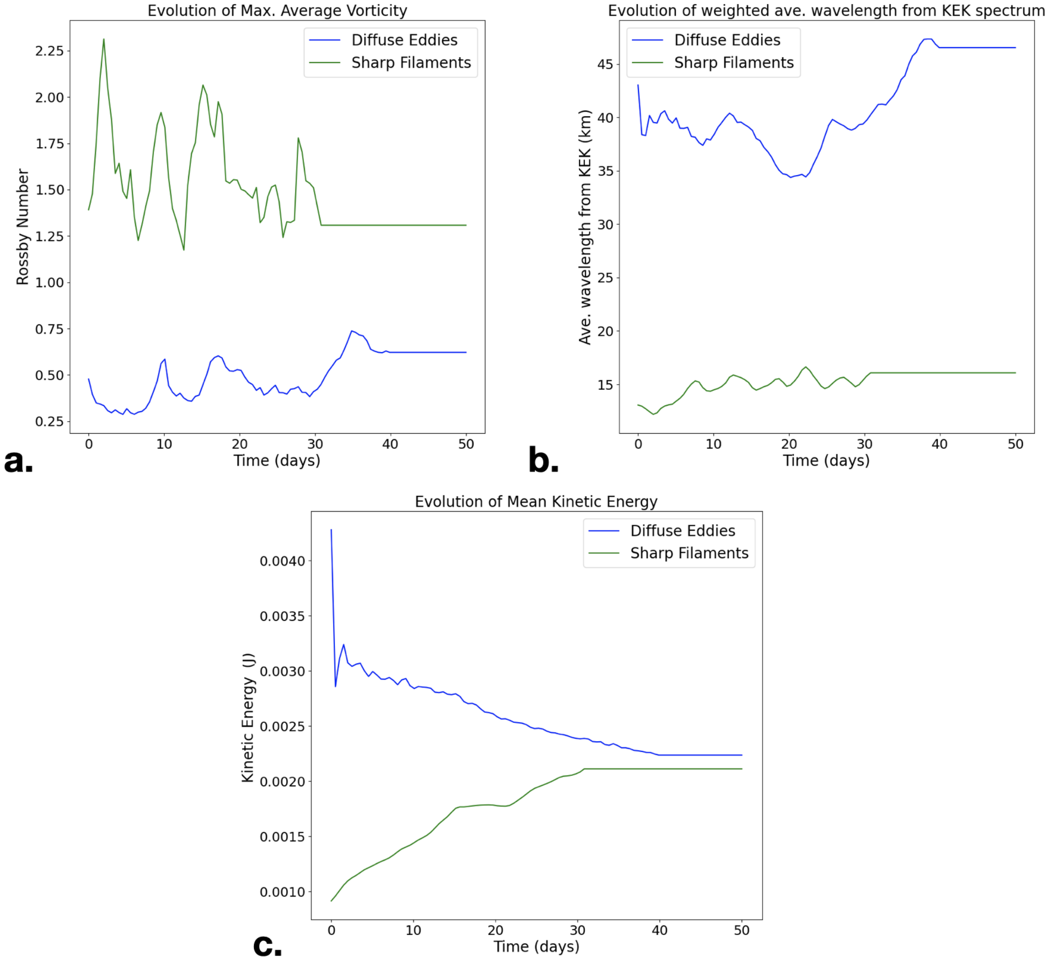

Figure 4.16: Comparison of diffuse and sharp current regimes: a. Evolution in the maximum average vorticity or normalized Rossby Number of diffuse and sharp regimes. b. Evolution of the weighted mean value of wavelength from the kinetic energy wave number spectrum of the domain. c. Evolution of the average kinetic energy for the entire domain, while not possible to make them the same, values were similar in average for both cases. Note that sharper currents have consistently higher vorticity maxima and shorter wavelength over simulation time. Due to limitations in the amount of ocean current data, a fraction of the last time steps was left constant to match desired simulation time, for both types of currents.

For a more quantitative comparison of diffuse and sharp cases and the effect of eddy wavelength on sea ice sheet breakage, Figure 4.17 shows the evolution of average diameter, ice sheet area for the diffuse and sharp cases and FSD changes. For Figure 4.17 a. both diffuse eddies and sharp filaments result in a similar decline of the average diameter and converge to the same final average value. In contrast, in Figure

4.17 b., diffuse eddies result in the total area of the landfast sea ice to be reduced more significantly and earlier than the sharp filaments, definitively confirming that the longer wavelength regime tends to break more landfast sea ice. This behavior agrees with the results of the idealized pulse examples shown before, where sharper filaments or pulses induce concentrated breakage that does not extend to the full ice sheet, while longer wavelengths resulted in more broken sea ice. Figures 4.17 c. and d. compare the evolution in power law coefficient or slope of the cumulative floe number distribution and show the final floe number distribution for each regime, respectively. Initially, the sharp filaments break floes more uniformly and have a higher coefficient due to their stronger velocities. But eventually, the more diffuse eddies result in a more uniform or steeper FSD curve with a lower number of large sizes compared to the sharp case, but with much more smaller floes and a higher power coefficient α for a longer time. The sharp regime increases uniformity to a similar extent as the diffuse eddies, but more spatially limited and its final FSD slope α is less than that of the diffuse regime. Overall, more diffuse eddies tend to break sea ice into several smaller floes. Sharp filaments cut the ice sheet into fewer large floes, with less smaller floes than the diffuse case, analogous to the longer wavelength and shorter wavelength scenarios shown in the previous section (Figure 4.8). Compared to observations, bonded particle method simulations show similar power coefficients, sheet area and diameters, but due to a combination of processing noises, advection of external floes, and less breakage of smaller floes, observational results and simulations differ slightly, albeit following similar trends and observations being more closely represented by the diffuse regime.

4.7 Discussion

Landfast sea ice breakage can be subjected to varying material and forcing conditions that affect sea ice FSD evolution, how quickly an ice sheet can be fractured into fine floes and the extent to which sea ice is completely removed. To replicate this phenomenon, we used a bonded particle method (LS-DEM-BPM) that provided the capabilities of representing intact sea ice sheets, coarse broken floes and fine slurry. Response of this sheet-floe system to ocean current characteristics was the main focus of this chapter.

To better assess the impact of ocean current properties, we first implemented a series of idealized pulse simulations using very simple sinusoidal unidirectional spatial velocity distributions on regular geometries. We started with a single fixed pulse, then a propagating single pulse and approached more realistic conditions with mul-

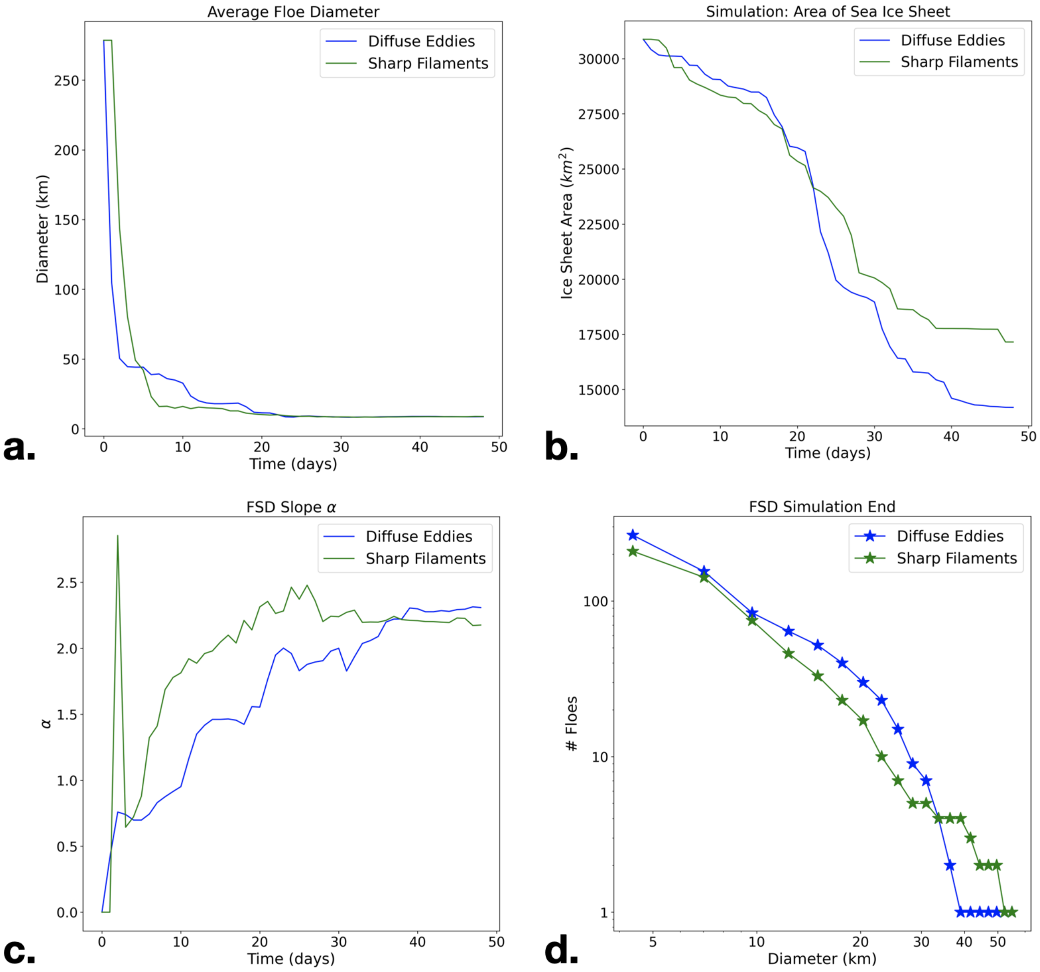

Figure 4.17: Comparison of results for diffuse and sharp regimes. First, we present a. mean diameter evolution plots. Diffuse and sharp results are very similar. Then, we have b. extent of fast ice sheet area in sq. kilometers. As expected, sea ice sheet area is reduced faster and more for the diffuse regime. Finally, we compare FSD indicators. c. Power coefficient evolution for the diffuse regime takes longer to increase uniformity due to less energetic breakage but, gradually, reaches and surpasses sharp current uniformity. d. Final floe size distribution also shows how the diffuse regime has more broken floes, in particular, for smaller sizes. They even show a similar trend to the FSD slopes shown in Figure 4.1.

tiple propagating pulses. For the fixed pulse, we were able to identify characteristic length and time scales for breakage, obtained from material properties, current magnitude or amplitude and pulse wavelength. Also, for single and multiple propagating pulse scenarios we found wavelength and wave propagation speed conditions which optimized sea ice sheet breakage. Hence, pulse wavelength was associated with failure area and this was a general trend that applied to all idealized pulses. In other words, wider pulses broke ice over a larger area, while concentrated (short wavelength) pulses cut the ice sheet along narrow and focused locations. However, this wavelength-breakage length or area relation cannot keep increasing indefinitely. A cutoff length was identified for this wavelength effect, as well. If a pulse becomes too widely spread, its low relative velocity over space is unable to generate forces that exceed critical fracture values. As a result, an optimal pulse wavelength exists that maximizes the area of sea ice broken for all these pulses. Pulse frequency or wave propagation speed was also found to foster greater breakage in ice sheets if particular wave speeds are reached to optimize fracture. Specifically, very slow pulses are limited in how much ice they can reach to break while very fast pulses cannot exchange ocean momentum with sea ice unless they have sufficient time to develop forcing. So, an optimal pulse wave propagation velocity maximizes sea ice sheet breakage and it is related to material properties, amplitude and wavelength. These optimal regimes identified are tied to minimizing the average diameter of broken floes and total sea ice sheet area and maximizing the uniformity coefficient or FSD slope of this system.

To transition to more realistic currents and validate their results, satellite data from MODIS images was used to provide qualitative and quantitative insight into the changes of fast ice in a particular region chosen for Fram Strait in 2023. These images were also very convenient to initialize geometry. Many of the changes observed in images were also presented in and further explained by reanalysis data from repositories such as the Copernicus Marine Database. As a result, there is sufficient observational data available to both help calibrate models and, inversely, deduce characteristics of field forcing conditions, specifically by measuring concentration, area, diameters and FSD changes in fast sea ice. These data has been used as a reference to assess the behavior of more realistic runs of our numerical model.

With a better understanding of the impact of ocean current wavelength and in situ behavior of sea ice sheets, it was only then we could proceed to work with arbitrary eddying currents and irregular observational-based geometries. As hypothesized, similar results to simple pulses were found when developing breakage simulations with eddying geostrophic currents based on `Oceananigans.jl`. We proposed two extreme regimes (*diffuse* and *sharp*) and found out that the way ocean eddies are spatially configured, especially their wavelength, significantly affects breakage evolution. More diffuse eddies induce more breakage, generate smaller floes, and increase the power coefficient or slope of the FSD. The opposite happens for sharper filaments, which induce less areal breakage, generate more larger floes, and do not increase the FSD uniformity as much. For similar maximum vorticity and much lower average kinetic energy, the wider wavelength diffuse regime maximized breakage, as it was also identified in the sinusoidal pulse examples. This allows us to conclude that the characteristic wavelength of ocean currents can control landfast sea ice breakage, with all other conditions kept the same, and certain values of current wavelength may maximize breakage in specific types of sea ice sheets.

Compared to observations, diffuse eddying currents were qualitatively closer in terms of ice sheet area reduction, mean diameter evolution and changes in floe size distribution. This is promising, since without any fine-tuning, our method can replicate the overall trends of observed landfast sea ice decay. This can be improved by trying additional current regimes, employing eddying currents closer to observational behaviors or adjusting them to approach in situ image processing results and modifying material properties.

While our findings are promising and show the close relationship among currents, sea ice properties and fracture, there are several more opportunities in this area of research. Fast ice failure is a thermodynamic process, not only mechanical. Temperature rise in the atmosphere and ocean surface gradually thins the ice sheet until it reaches a failure threshold. Before certain threshold, fast ice is relatively undisturbed, but after sufficient melt, breakage events accelerate. So we will implement simulations with varying thickness to study this effect. To further analyze ocean currents, we also plan to develop additional numerical experiments in terms of propagation velocity of eddying currents, to validate a possible optimal wave speed for breakage as suggested by the pulse simulations. Moreover, we can combine both ocean currents and winds from a much larger scale to capture the importance of breakage events during storms. Using vertical waves together with the horizontal eddies from this study might also enhance fracture and spalling representation.

Finally, aside from Fram Strait, there are several regions such as the Beaufort Sea, Kara Sea, Nares Strait, and Baffin Bay that can be studied using the methodology and ideas presented here.

Chapter 5

CONCLUSIONS AND FUTURE WORK

In this document we present various contributions to the state of the art of sea ice discrete element modeling, focusing on the critical phenomena of breakage and melt. With increasing temperatures in the Arctic and Antarctic regions, sea ice will be more exposed to both of these event more frequently and in more complex ways, which have shown, cannot be merely analyzed from a continuum standpoint. We discuss contributions ranging from a new method that uses satellite-based sea ice floe shapes susceptible to breakage and melt; a study of breakage and melt intensity relative dominance over floe size distribution changes in sea ice and mass loss effects; and an analysis, using bonded particle DEM, of the relationship of oceanic currents properties and vertical melt with respect to the breakage of monolithic fast ice sheets transitioning into a broken-down floe regime. Hence, we are able to examine, respectively, the MIZ decay stage from discrete floes into slurry ice or open ocean (for the new method and study) and the initial failure stage that converts a solid ice sheet into these discrete floes (BPM analysis).

5.1 LS-ICE Method

For the new method developed, called LS-ICE, we leveraged the versatility of level sets in LS-DEM to better model sea ice floes. This is particularly relevant in two aspects. The first one, is the intrinsic irregular shape of sea ice and how it affects its kinematics, ensemble packing fraction, response to oceanic and wind forcing, breakage behavior and exposed surface area for melt. Irregular floe mosaics or ensemble will behave differently than idealized circles, hence using satellite data and level sets to fully use irregular shapes has a significant impact, in particular for aggressive melt and break regimes. The second one is that we can use level set to overlap the floe geometry grid, with temperature and thickness grid and induced changes in floe properties based on thermodynamic fields. This allows to make ice kinematic properties such as mass and moment of inertia to be coupled with thermodynamic changes. Also, as temperature is directly tied to thickness it is very straightforward to melt ice and, with some additional assumptions, to also re-freeze sea ice floes. Since the method is tied to satellite data, it is possible to implement direct comparison for concentration and FSD evolution. With the correct tuning of the model, in-situ behavior for specific regions and periods can be replicated adequately and there is the potential for implementing predictive models combining a realistic geometry, well tuned-changes and comprehensive initial and evolving conditions for temperature, currents and waves.

5.2 Break versus Melt Regimes and FSD

With our LS-ICE method developed and bench-marked or calibrated to a specific scenario of breakage frequency and melt rate, it is a natural progression to ask: How would the system evolve in response to these two vital parameters if we take them to the extreme and run a sensitivity analysis? How does the combination that minimizes observational error explains properties of the region that cannot be obtained from observations? So far, only continuum implementations of FSD evolution have been developed, even within some discrete implementations. As a result, we propose using the individual statistic of each floe and keep track of them rather than using an average per square kilometer. Albeit computationally expensive, having the capacity to track changes in every single sea ice block in a domain has its advantages. Foremost, by using a pseudo-3D approach with thickness, we can simulate sea ice mass evolution rather than concentration only evolution, even more so as thickness information of sea ice is still very limited in time and space. But, more importantly, this allows a more thorough track of sea ice for its changes in FSD. In addition to keeping good control of the power law coefficient, it is also possible to keep track of changes among sizes and even understand the relative contribution of lateral and vertical melt. We can use this mass and FSD to develop indicators to study the sea ice system. For the region of West Greenland / Baffin Bay explored, a certain combination in which melt has a slight dominance in removing large or coarse floe mass is that which minimizes concentration and FSD error. However, there are other combinations which favor breakage more or for which melt removes most of the mass. We can then use observational results to indirectly deduce which is the regime for a period and region, thanks to the high level of detail offered by the DEM.

5.3 Ocean Currents and Breakage

With a better understanding of the floe to the open ocean regime, we then focus on the fast ice to floe regime. In this work, we focused on the spring to summer transition, where both sea ice sheets and floes do not recover via refreezing and tend to monotonically decrease in concentration or sea ice sheet area. This regime is favored both by our LS-ICE method and the fact observational snapshots are easier to obtain between March – October of each year. Other sea ice models have elaborated more on the re-freezing winter regime, so we dedicated to the decomposition, breakage and melt regime. Fast ice sheets have now less time to heal or re-freeze and longer periods during which melt and oceanic forcing occurs, so we consider this a more relevant time to analyze the system. For this type of sea ice condition, handling LS-ICE floes can become computationally prohibitive, as we would require FEM, re-meshing and Phase Field Modeling of the largest floes at frequent time stepping. As floes break down fractally, it becomes even more complex. As a result, we switch to LS-DEM-BPM and make our sea ice sheet out of bonded simple shapes that break down into smaller floes which can keep breaking down into a fine scale. The evolution of sharp floes into rounded floes and the breakdown of large floes into fine slurry can be captured by this method, showcasing its convenience for this stage of sea ice modeling. We subject this landfast sea ice to a similar conditions as in LS-ICE, but keep an isothermal regime to emphasize ocean current effects. The most novel contribution for this BPM-modelled-breakage comes from using more complex and closer to reality oceanic forcing regimes than any other previous works shown in Chapter 1. Most prior BPM-DEMs for fast ice have used idealized (unidirectional and mostly non-evolving) and large scale winds (>500 km), so we choose instead to use arbitrary eddying ocean currents at smaller scales (5–200 km) with more complicated spatial variations below the sea ice sheet. First, we try ideal scenarios in shape using sinusoidal currents, to extract the fundamental aspects of ocean velocity spatial distribution and sea ice fracture. But then we transition to realistic eddy regimes with varying wavelengths as their main distinction. Using these eddies and filaments, progressive failure of ice and characteristic time and length scales for failure can be implemented, which simpler winds are unable to do. In particular, identifying eddying wavelengths that maximize sea ice sheet breakage, found to be diffuse eddy regimes, is something our method is particularly effective in achieving. Our approach provides the opportunity to better understand fast ice break-up responding to upper ocean turbulence evolution under changing Arctic conditions.

5.4 Comparison of DEM Methods and Cryosphere Applications

For this work we use the more traditional bonded particle method approach with circular disks with many elements, so floe ensembles can approach continuum fast ice. And we use a floe-by-floe multi-grid and level set method with LS-ICE to study discrete floe systems such as those of the MIZ. While a significant part of this work emphasizes the development of LS-ICE (with extremely high control of each single coarse floe), we choose to switch to other methods whenever it is convenient. This philosophy is at the core of incorporating mechanics approaches to complex geomechanical and geophysical systems. Conventional continuum methods using parametrizations have a limit to mostly large scales, so discrete models are becoming more commonplace. However, this discrete models often come from other disciplines and require caution when used to deal with different materials, for example from sands at the micro scale, to sea ice at a regional scale. Dimensional consistency, adequate time-stepping and numerical stability can all be compromised if not done carefully. Regardless, the opportunities offered by adapting and embracing these methods in new disciplines are an active area of study and provide a new frontier in terms of gaining insight about subjects that have never been tackled this way before. While challenging, the potential and opportunities of using mechanics for studying the cryosphere can provide the necessary boost to further project our changing planet under global warming.

5.5 Relevance of Observational Data for Sea Ice Modeling

One of the main limitations for modeling these large-scale systems is the lack of experimental and observational data. While experiments can be developed at smaller scales, several phenomena that can have a significant impact cannot be easily replicated at these scales (Coriolis forces, temperature and fluid variations across large regions, etc.). Furthermore, very few experimental facilities and publications exist in the topic of both sea ice as a mosaic of floes and as a fast ice sheet. Nevertheless, the only way to calibrate sea ice simulations is often using material properties from unrelated experiments and indirect measurements of mechanical changes such as concentration and the floe size distribution. Often, temporal and spatial resolution of reference values for thickness, critical fracture energy, elastic modulus, temperature and others is very limited; the more rich the information, the more sparse it becomes or it is only available for smaller scales. On top of that there is a very high level of certainty of the initial state and the forcing conditions of sea ice systems. Thickness distribution, brine inclusions, melt ponds, cracks beyond image resolution and material damage are all very challenging to define for floes and sheets initial state and they can play a critical role in failure events. Only simplifications or random distributions can often be utilized. For forcing conditions, things can be as challenging. Sufficiently-scaled information for atmospheric and ocean temperature, solar flux, wave effects, floe collisions and wind and ocean currents is not easy to obtain and average values or approximations have to be used most of the time. So, we have to consider uncertain forcing conditions acting on unknown initial states for our model to then be compared with restricted observational or experimental data. As a result, limitations for full scale sea ice ensembles require modelers to establish sensible idealizations and understanding the current limits. Even then, it is possible to extract vital indicator and understand better, but finding new tools and research to address these limitation is a pressing matter for this sensitive area of study.

5.6 Melt and Breakage Synergies

Another reason why sea ice systems are particularly challenging to model is their simultaneous vulnerability to two feedback loops: melt and breakage (see Figure 5.1 a. and b.). The melt positive feedback loop consists in that after a certain amount of melt leading to a critical concentration threshold in a region, the albedo in this region decreases, which leads to more solar flux being absorbed by the ocean, which increases temperature faster, which melts more sea ice and decreases albedo even more, until all ice is removed in shorter periods. The breakage positive feedback consists in that after a certain threshold area of sea ice is broken down, ocean currents can get more energetic due to diminished current damping since less ocean-sea ice momentum exchange can happen as the result of having less solid ice, which lead to more ice being broken down, stronger currents and the whole ice mass being fractured. Naturally, these two feedback loops can interact with each other to make sea ice decline even faster, as summarized in Figure 5.2. Higher temperatures related to melt and albedo reduction can lead to stronger storms which can then break ice faster (Zhang et al., 2023). More broken down ice has a higher surface area that leads to enhanced melt. Significant melt can reduce sea ice thickness which makes it easier to break down. Stronger ocean currents within broken ice can advect warmer fluids into a sea ice region faster or broken down floes can be easier to drift to warmer areas and so on. Fortunately, our methods have the adequate characteristics to capture the impact of both these loops, at least in simpler combinations. Nonetheless, interactions between these loops and other unknowns can still make sea ice predictions have significant uncertainty even if experimental data, initial conditions and forcing conditions were all know to perfection, as the physical system itself is very complex.

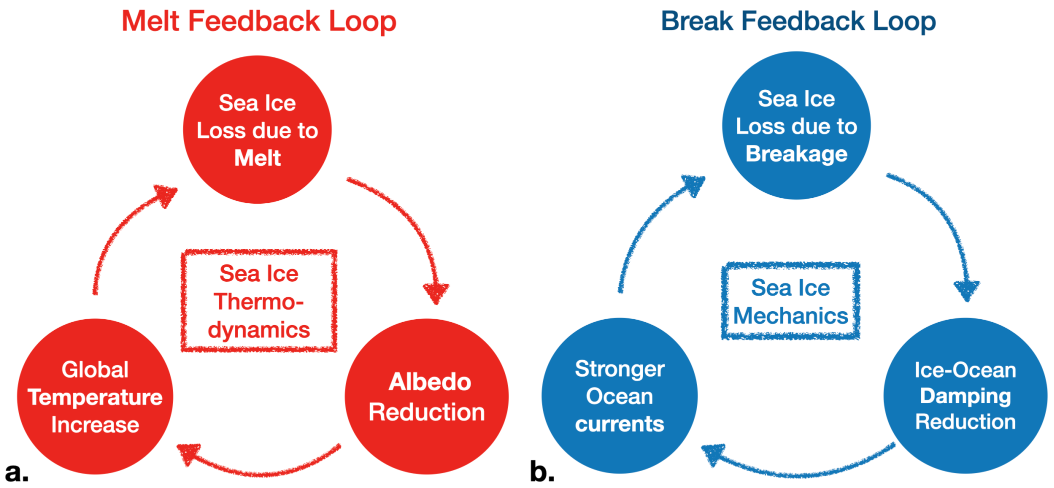

Figure 5.1: Observed feedback loops in sea ice: a. Melt feedback loop, where temperature increase melts more sea ice, which reduces albedo and lead to further temperature increase. b. Breakage feedback loop, where agitated ocean currents break more sea ice, which reduces oceanic damping or the energy lost from ice-ocean momentum exchange, which results in even stronger currents.

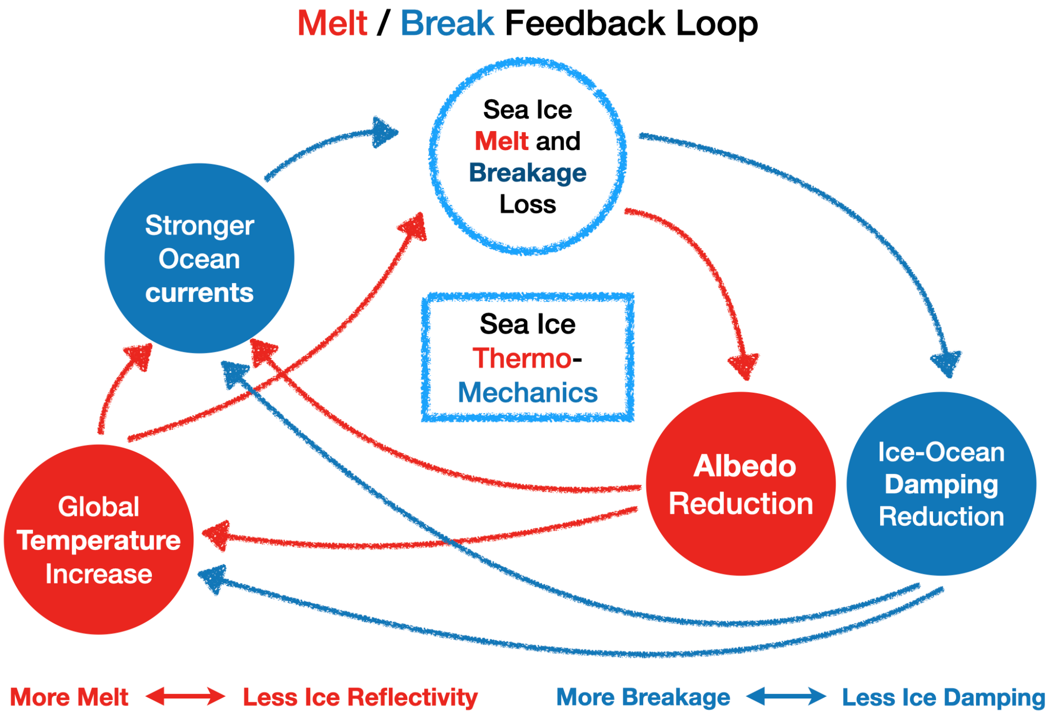

Figure 5.2: Combination of melt and breakage feedbacks, including conditions than increase ice loss, consequences of ice loss as damping and albedo reduction and role of these reductions into increasing sea ice thermodynamic and mechanical forcings.

5.7 Future Work to Implement

Given its complex and challenging nature, discrete element modeling of sea ice is a very active research field and potential contributions and improvements are numerous. In the case of our work, several successive steps can be proposed. For LS-ICE we can combine its simplified breakage model with a phase field continuum damage mechanics model to break larger floes into physically-based shapes, responding to floe collisions and wind and oceanic currents, rather than using a breakage frequency, which was not fully implemented due to time and computational constraint that can be worked on with sufficient resources. Melt ponds and a snow layer component can also be added to consider additional albedo and vertical melt consideration and enhance thermodynamics aspect as well. Other regions apart from West Greenland can also be analyzed for the characteristic melt and breakage regimes. For fast ice modeling using bonded particle method, damping using nearest distance instead of a damping front simplification could be optimized for better spalling. A more rigorous bonded particle method considering cumulative damage and visco-plastic components can be implemented as well. For both approaches obtaining a more sophisticated thickness distribution over space and time from observations would provide a much-needed detail for enhance realism. In the aspect of currents, observations can be better tied to arbitrary currents and approximate close regimes to on-going climate conditions, without making computations impractical.

5.8 Other Applications of this Work

There are several opportunities for applying the methods and findings of this work in other research areas, mostly LS-ICE. An obvious example are other types of geomaterials. For rock mechanics, level set functions that consider weathering rocks (analogous to melt) can be used for changing properties and geometries of rock cliffs or ensembles of jointed or disjointed rocks. This can similarly be done for failure in ice cliffs in glaciers, where contact with broken down icebergs can play an important role in additional damage or fluid interactions. Suspensions of granular materials than can dissolve or agglomerate over time being transported by currents, are also a possibility such as those in rivers or coastal areas.

In addition, industrial and chemical processing of granular material undergoing breakage and dissolution at the same or in difference sequences could also use LS-ICE, Bonded particles or a combination of both to replicate and build predictive models, particularly with more controlled conditions. Then, sensitivity testing could be done to optimize desired processes using virtual experiments and tuning breakage and dissolution or agglomeration or growth parameters. Following with these, for biological sciences or medicine, particulate materials that break and melt in tandem and in contact with fluids are very relevant. For example, blood clotting formed at irregularities and the conditions leading to it, can be approximated with this method, especially the capacity to grow or shrink due to a forcing field. More on the fracture aspect, lithotripsy (fracturing kidney stones or other organ solid deposits) combining breakage and melt could be analyzed using our methods.

BIBLIOGRAPHY

Adcroft, A. J., Hill, C., Campin, J. M., Marshall, J., & Heimbach, P. (2004). Overview of the formulation and numerics of the mit gcm . vnorth uwest ueast vsouth wup. https://api.semanticscholar.org/CorpusID:203558468

Andersson, T. R., Hosking, J. S., Pérez-Ortiz, M., Paige, B., Elliott, A., Russell, C., Law, S., Jones, D. C., Wilkinson, J., Phillips, T., Byrne, J., Tietsche, S., Sarojini, B. B., Blanchard-Wrigglesworth, E., Aksenov, Y., Downie, R., & Shuckburgh, E. (2021). Seasonal arctic sea ice forecasting with probabilistic deep learning. *Nature Communications*, *12*(1). https://doi.org/10.1038/s41467-021-25257-4

Armitage, T. W. K., Manucharyan, G. E., Petty, A. A., Kwok, R., & Thompson, A. F. (2020). Enhanced eddy activity in the beaufort gyre in response to sea ice loss. *Nature Communications*, *11*(1). https://doi.org/10.1038/s41467-020-14449-z

Asplin, M. G., Scharien, R., Else, B., Howell, S., Barber, D. G., Papakyriakou, T., & Prinsenberg, S. (2014). Implications of fractured arctic perennial ice cover on thermodynamic and dynamic sea ice processes. *Journal of Geophysical Research: Oceans*, *119*(4), 2327–2343. https://doi.org/10.1002/2013jc009557

Astakhov, V. (1998). The last ice sheet of the kara sea: Terrestrial constraints on its age. *Quaternary International*, *45-46*, 19–28. https://doi.org/10.1016/s1040-6182(97)00003-7

Åström, J., Cook, S., Enderlin, E. M., Sutherland, D. A., Mazur, A., & Glasser, N. (2021). Fragmentation theory reveals processes controlling iceberg size distributions. *Journal of Glaciology*, *67*(264), 603–612. https://doi.org/10.1017/jog.2021.14

Barber, D. G., Babb, D. G., Ehn, J. K., Chan, W., Matthes, L., Dalman, L. A., Campbell, Y., Harasyn, M. L., Firoozy, N., Theriault, N., Lukovich, J. V., Zagon, T., Papakyriakou, T., Capelle, D. W., Forest, A., & Gariepy, A. (2018). Increasing mobility of high arctic sea ice increases marine hazards off the east coast of Newfoundland. *Geophysical Research Letters*, *45*(5), 2370–2379. https://doi.org/10.1002/2017gl076587

Bateman, S. P., Orzech, M. D., & Calantoni, J. (2019). Simulating the mechanics of sea ice using the discrete element method. *Mechanics Research Communications*, *99*, 73–78. https://doi.org/10.1016/j.mechrescom.2019.06.009

Bateson, A. W., Feltham, D. L., Schröder, D., Hosekova, L., Ridley, J. K., & Aksenov, Y. (2020). Impact of sea ice floe size distribution on seasonal fragmentation and melt of arctic sea ice. *The Cryosphere*, *14*(2), 403–428. https://doi.org/10.5194/tc-14-403-2020

Bateson, A. W., Feltham, D. L., Schröder, D., Wang, Y., Hwang, B., Ridley, J. K., & Aksenov, Y. (2022). Sea ice floe size: Its impact on pan-arctic and local ice mass and required model complexity. *The Cryosphere*, *16*(6), 2565–2593. https://doi.org/10.5194/tc-16-2565-2022

Bažant, Z. P. (1992). Large-scale thermal bending fracture of sea ice plates. *Journal of Geophysical Research: Oceans*, *97*(C11), 17739–17751. https://doi.org/10.1029/92jc00816

Blanchard-Wrigglesworth, E., Cullather, R., Wang, W., Zhang, J., & Bitz, C. (2015). Model forecast skill and sensitivity to initial conditions in the seasonal sea ice outlook. *Geophysical Research Letters*, *42*(19), 8042–8048.

Boutin, G., Williams, T., Rampal, P., Olason, E., & Lique, C. (2020). Wave–sea-ice interactions in a brittle rheological framework. *The Cryosphere*. https://doi.org/10.5194/tc-2020-19

Boutin, G., Williams, T., Rampal, P., Olason, E., & Lique, C. (2021). Wave–sea-ice interactions in a brittle rheological framework. *The Cryosphere*, *15*(1), 431–457. https://doi.org/10.5194/tc-15-431-2021

Clayton, T., Duddu, R., Siegert, M., & Martınez-Pañeda, E. (2022). A stress-based poro-damage phase field model for hydrofracturing of creeping glaciers and ice shelves. *Engineering Fracture Mechanics*, *272*, 108693. https://doi.org/10.1016/j.engfracmech.2022.108693

Cohen, J., Screen, J. A., Furtado, J. C., Barlow, M., Whittleston, D., Coumou, D., Francis, J., Dethloff, K., Entekhabi, D., Overland, J., & Jones, J. (2014). Recent arctic amplification and extreme mid-latitude weather. *Nature Geoscience*, *7*(9), 627–637. https://doi.org/10.1038/ngeo2234

Cole, D. M. (2001). The microstructure of ice and its influence on mechanical properties. *Engineering Fracture Mechanics*, *68*(17-18), 1797–1822. https://doi.org/10.1016/s0013-7944(01)00031-5

Coon, M. D., Knoke, G. S., Echert, D. C., & Pritchard, R. S. (1998). The architecture of an anisotropic elastic-plastic sea ice mechanics constitutive law. *Journal of Geophysical Research: Oceans*, *103*(C10), 21915–21925. https://doi.org/10.1029/98jc01259

Crabeck, O., Galley, R. J., Mercury, L., Delille, B., Tison, J.-L., & Rysgaard, S. (2019). Evidence of freezing pressure in sea ice discrete brine inclusions and its impact on aqueous-gaseous equilibrium. *Journal of Geophysical Research: Oceans*, *124*(3), 1660–1678. https://doi.org/10.1029/2018jc014597

Cundall, P. A., & Strack, O. D. L. (1979a). A discrete numerical model for granular assemblies [Publisher: ICE Publishing]. *Géotechnique*, *29*(1), 47–65. https://doi.org/10.1680/geot.1979.29.1.47

Cundall, P. A., & Strack, O. D. L. (1979b). A discrete numerical model for granular assemblies. *Géotechnique*, *29*(1), 47–65. https://doi.org/10.1680/geot.1979.29.1.47

Damsgaard, A., Adcroft, A., & Sergienko, O. (2018). Application of discrete element methods to approximate sea ice dynamics. *Journal of Advances in Modeling Earth Systems*, *10*(9), 2228–2244. https://doi.org/10.1029/2018ms001299

Damsgaard, A., Sergienko, O., & Adcroft, A. (2021). The effects of ice floe-floe interactions on pressure ridging in sea ice. *Journal of Advances in Modeling Earth Systems*, *13*(7). https://doi.org/10.1029/2020ms002336

Dansereau, V., Weiss, J., Saramito, P., Lattes, P., & Coche, E. (2017). Ice bridges and ridges in the maxwell-EB sea ice rheology. *The Cryosphere*, *11*(5), 2033–2058. https://doi.org/10.5194/tc-11-2033-2017

Dempsey, Adamson, R., & Mulmule, S. (1999). *International Journal of Fracture*, *95*(1/4), 347–366. https://doi.org/10.1023/a:1018650303385

Dempsey, Cole, D. M., & Wang, S. (2018). Tensile fracture of a single crack in first-year sea ice. *Philosophical Transactions of the Royal Society A: Mathematical, Physical and Engineering Sciences*, *376*(2129), 20170346. https://doi.org/10.1098/rsta.2017.0346

Dempsey, DeFranco, S. J., Blanchet, D., & Prodanovic, A. (1994). Mechanisms of fracture of sea ice. *Hydrotechnical Construction*, *28*(3), 164–168. https://doi.org/10.1007/bf01545933

Denton, A. A., & Timmermans, M.-L. (2022). Characterizing the sea-ice floe size distribution in the canada basin from high-resolution optical satellite imagery. *The Cryosphere*, *16*(5), 1563–1578. https://doi.org/10.5194/tc-16-1563-2022

Deser, C., Tomas, R., Alexander, M., & Lawrence, D. (2010). The seasonal atmospheric response to projected arctic sea ice loss in the late twenty-first century. *Journal of Climate*, *23*(2), 333–351. https://doi.org/10.1175/2009jcli3053.1

Diamond, R., Sime, L. C., Schroeder, D., & Guarino, M.-V. (2021). The contribution of melt ponds to enhanced arctic sea-ice melt during the last interglacial. *The Cryosphere*, *15*(11), 5099–5114. https://doi.org/10.5194/tc-15-5099-2021

Dinh, H., Giannakis, D., Slawinska, J., & Stadler, G. (2022). Phase-field models of floe fracture in sea ice. https://doi.org/10.5194/egusphere-2022-790

Dou, T. F., Pan, S. F., Bintanja, R., & Xiao, C. D. (2022). More frequent, intense, and extensive rainfall events in a strongly warming arctic. *Earth's Future*, *10*(10). https://doi.org/10.1029/2021ef002378

Duriez, J., & Bonelli, S. (2021). Precision and computational costs of level set-discrete element method (LS-DEM) with respect to DEM. *Computers and Geotechnics*, *134*, 104033. https://doi.org/10.1016/j.compgeo.2021.104033

Egger, A., Pillai, U., Agathos, K., Kakouris, E., Chatzi, E., Aschroft, I. A., & Triantafyllou, S. P. (2019). Discrete and phase field methods for linear elastic fracture mechanics: A comparative study and state-of-the-art review. *Applied Sciences*, *9*(12), 2436. https://doi.org/10.3390/app9122436

Einstein, N. (2023). Fram strait. https://en.wikipedia.org/wiki/Fram_Strait

ESA. (2021). Rus webinar: Sea ice monitoring using sentinel-1 data. https://eo4society.esa.int/event/rus-webinar-sea-ice-monitoring-using-sentinel-1-data/

Feltham, D. L. (2008). Sea ice rheology. *Annual Review of Fluid Mechanics*, *40*(1), 91–112. https://doi.org/10.1146/annurev.fluid.40.111406.102151

Fenty, I., & Heimbach, P. (2013). Hydrographic preconditioning for seasonal sea ice anomalies in the labrador sea. *Journal of Physical Oceanography*, *43*(5), 863–883. https://doi.org/10.1175/jpo-d-12-064.1

Ford, V. L., Frauenfeld, O. W., Nowotarski, C. J., & Bombardi, R. J. (2021). Effective sea ice area based on a thickness threshold. *Climate Dynamics*, *56*(11-12), 3541–3552. https://doi.org/10.1007/s00382-021-05655-6

Girard, L., Bouillon, S., Weiss, J., Amitrano, D., Fichefet, T., & Legat, V. (2011). A new modeling framework for sea-ice mechanics based on elasto-brittle rheology. *Annals of Glaciology*, *52*(57), 123–132. https://doi.org/10.3189/172756411795931499

Gray, J., & Morland, L. (1994). A two-dimensional model for the dynamics of sea ice. *Philosophical Transactions of the Royal Society of London. Series A: Physical and Engineering Sciences*, *347*(1682), 219–290. https://doi.org/10.1098/rsta.1994.0045

Guarino, M.-V., Sime, L. C., Schröeder, D., Malmierca-Vallet, I., Rosenblum, E., Ringer, M., Ridley, J., Feltham, D., Bitz, C., Steig, E. J., Wolff, E., Stroeve, J., & Sellar, A. (2020). Sea-ice-free arctic during the last interglacial supports fast future loss. *Nature Climate Change*, *10*(10), 928–932. https://doi.org/10.1038/s41558-020-0865-2

Guemas, V., Blanchard-Wrigglesworth, E., Chevallier, M., Day, J. J., Déqué, M., Doblas-Reyes, F. J., Fučkar, N. S., Germe, A., Hawkins, E., Keeley, S., et al. (2016). A review on arctic sea-ice predictability and prediction on seasonal to decadal time-scales. *Quarterly Journal of the Royal Meteorological Society*, *142*(695), 546–561.

Gupta, M., Marshall, J., Song, H., Campin, J.-M., & Meneghello, G. (2020). Sea-ice melt driven by ice-ocean stresses on the mesoscale. *Journal of Geophysical Research: Oceans*, *125*(11). https://doi.org/10.1029/2020jc016404

Gupta, M., & Thompson, A. F. (2022a). Regimes of sea-ice floe melt: Ice-ocean coupling at the submesoscales. *Journal of Geophysical Research: Oceans*, *127*(9), e2022JC018894. https://doi.org/10.1029/2022JC018894

Gupta, M., & Thompson, A. F. (2022b). Regimes of sea-ice floe melt: Ice-ocean coupling at the submesoscales. *Journal of Geophysical Research, submitted*. https://doi.org/Pending

Gutfraind, R., & Savage, S. B. (1997). Marginal ice zone rheology: Comparison of results from continuum-plastic models and discrete-particle simulations. *Journal of Geophysical Research: Oceans*, *102*(C6), 12647–12661. https://doi.org/10.1029/97jc00124

Harmon, J. M., Arthur, D., & Andrade, J. E. (2020). Level set splitting in DEM for modeling breakage mechanics. *Computer Methods in Applied Mechanics and Engineering*, *365*, 112961. https://doi.org/10.1016/j.cma.2020.112961

Harmon, J. M., Karapiperis, K., Li, L., Moreland, S., & Andrade, J. E. (2021). Modeling connected granular media: Particle bonding within the level set discrete element method. *Computer Methods in Applied Mechanics and Engineering*, *373*, 113486. https://doi.org/10.1016/j.cma.2020.113486

Herman, A. (2018). Wave-induced surge motion and collisions of sea ice floes: Finite-floe-size effects. *Journal of Geophysical Research: Oceans*, *123*(10), 7472–7494. https://doi.org/10.1029/2018jc014500

Herman, A. (2011). Molecular-dynamics simulation of clustering processes in sea-ice floes. *Physical Review E*, *84*(5). https://doi.org/10.1103/physreve.84.056104

Herman, A. (2013). Numerical modeling of force and contact networks in fragmented sea ice. *Annals of Glaciology*, *54*(62), 114–120. https://doi.org/10.3189/2013aog62a055

Herman, A. (2017). Wave-induced stress and breaking of sea ice in a coupled hydrodynamic discrete-element wave–ice model. *The Cryosphere*, *11*(6), 2711–2725. https://doi.org/10.5194/tc-11-2711-2017

Herman, A., Wenta, M., & Cheng, S. (2021). Sizes and shapes of sea ice floes broken by waves–a case study from the east antarctic coast. *Frontiers in Earth Science*, *9*. https://doi.org/10.3389/feart.2021.655977

Hibler, I., W. D. (1979). A dynamic thermodynamic sea ice model. *Journal of Physical Oceanography*, *9*(4), 815–846. https://doi.org/10.1175/1520-0485(1979)009<0815:adtsim>2.0.co;2

Hopkins, M. A. (2004). A discrete element lagrangian sea ice model. *Engineering Computations*, *21*(2/3/4), 409–421. https://doi.org/10.1108/02644400410519857

Horvat, C., & Tziperman, E. (2015). A prognostic model of the sea-ice floe size and thickness distribution. *The Cryosphere*, *9*(6), 2119–2134. https://doi.org/10.5194/tc-9-2119-2015

Horvat, C., Roach, L. A., Tilling, R., Bitz, C. M., Fox-Kemper, B., Guider, C., Hill, K., Ridout, A., & Shepherd, A. (2019). Estimating the sea ice floe size distribution using satellite altimetry: Theory, climatology, and model comparison. *The Cryosphere*, *13*(11), 2869–2885. https://doi.org/10.5194/tc-13-2869-2019

Horvat, C., & Tziperman, E. (2017). The evolution of scaling laws in the sea ice floe size distribution. *Journal of Geophysical Research: Oceans*, *122*(9), 7630–7650. https://doi.org/10.1002/2016jc012573

Horvat, C., Tziperman, E., & Campin, J.-M. (2016). Interaction of sea ice floe size, ocean eddies, and sea ice melting. *Geophysical Research Letters*, *43*(15), 8083–8090. https://doi.org/10.1002/2016gl069742

Hunke, E. C., & Dukowicz, J. K. (1997). An elastic–viscous–plastic model for sea ice dynamics. *Journal of Physical Oceanography*, *27*(9), 1849–1867. https://doi.org/10.1175/1520-0485(1997)027<1849:aevpmf>2.0.co;2

Hwang, B., & Wang, Y. (2022). Multi-scale satellite observations of arctic sea ice: New insight into the life cycle of the floe size distribution. *Philosophical Transactions of the Royal Society A: Mathematical, Physical and Engineering Sciences*, *380*(2235). https://doi.org/10.1098/rsta.2021.0259

Hwang, B., Wilkinson, J., Maksym, T., Graber, H. C., Schweiger, A., Horvat, C., Perovich, D. K., Arntsen, A. E., Stanton, T. P., Ren, J., & Wadhams, P. (2017). Winter-to-summer transition of arctic sea ice breakup and floe size distribution in the beaufort sea (J. W. Deming & J. Thomson, Eds.). *Elementa: Science of the Anthropocene*, *5*. https://doi.org/10.1525/elementa.232

Jenkins, M., & Dai, A. (2021). The impact of sea-ice loss on arctic climate feedbacks and their role for arctic amplification. *Geophysical Research Letters*, *48*(15). https://doi.org/10.1029/2021gl094599

Johannessen, O. M., Johannessen, J. A., Svendsen, E., Shuchman, R. A., Campbell, W. J., & Josberger, E. (1987). Ice-edge eddies in the fram strait marginal ice zone. *Science*, *236*(4800), 427–429. https://doi.org/10.1126/science.236.4800.427

Jou, O., Celigueta, M. A., Latorre, S., Arrufat, F., & Oñate, E. (2019). A bonded discrete element method for modeling ship–ice interactions in broken and unbroken sea ice fields. *Computational Particle Mechanics*, *6*(4), 739–765. https://doi.org/10.1007/s40571-019-00259-8

Kacimi, S., & Kwok, R. (2022). Arctic snow depth, ice thickness, and volume from ICESat-2 and CryoSat-2: 2018–2021. *Geophysical Research Letters*, *49*(5). https://doi.org/10.1029/2021gl097448

Kawamoto, R., Andò, E., Viggiani, G., & Andrade, J. E. (2016). Level set discrete element method for three-dimensional computations with triaxial case study. *Journal of the Mechanics and Physics of Solids*, *91*, 1–13. https://doi.org/10.1016/j.jmps.2016.02.021

Kawamoto, R., Andò, E., Viggiani, G., & Andrade, J. E. (2018). All you need is shape: Predicting shear banding in sand with LS-DEM. *Journal of the Mechanics and Physics of Solids*, *111*, 375–392. https://doi.org/10.1016/j.jmps.2017.10.003

Key, J., & McLaren, A. S. (1991). Fractal nature of the sea ice draft profile. *Geophysical Research Letters*, *18*(8), 1437–1440. https://doi.org/10.1029/91gl01761

Kimmritz, M., Losch, M., & Danilov, S. (2017). A comparison of viscous-plastic sea ice solvers with and without replacement pressure. *Ocean Modelling*, *115*, 59–69. https://doi.org/10.1016/j.ocemod.2017.05.006

King, E. C., Rydt, J. D., & Gudmundsson, G. H. (2018). The internal structure of the brunt ice shelf from ice-penetrating radar analysis and implications for ice shelf fracture. *The Cryosphere*, *12*(10), 3361–3372. https://doi.org/10.5194/tc-12-3361-2018

Koldunov, N. V., Aizinger, V., Rakowsky, N., Scholz, P., Sidorenko, D., Danilov, S., & Jung, T. (2019). Scalability and some optimization of the finite-volumE sea ice–ocean model, version 2.0 (FESOM2). *Geoscientific Model Development*, *12*(9), 3991–4012. https://doi.org/10.5194/gmd-12-3991-2019

Konietzky, H. (2017). *Numerical modeling in micromechanics via particle methods* (H. Konietzky, Ed.). Routledge. https://doi.org/10.1201/9780203745335

Kumar, A., Yadav, J., & Mohan, R. (2020). Global warming leading to alarming recession of the arctic sea-ice cover: Insights from remote sensing observations and model reanalysis. *Heliyon*, *6*(7), e04355. https://doi.org/10.1016/j.heliyon.2020.e04355

Kwok, R. (2004). Fram Strait sea ice outflow. *Journal of Geophysical Research*, *109*(C1). https://doi.org/10.1029/2003jc001785

Kwok, R. (2018). Arctic sea ice thickness, volume, and multiyear ice coverage: Losses and coupled variability (1958–2018). *Environmental Research Letters*, *13*(10), 105005. https://doi.org/10.1088/1748-9326/aae3ec

Kwok, R., Spreen, G., & Pang, S. (2013). Arctic sea ice circulation and drift speed: Decadal trends and ocean currents. *Journal of Geophysical Research: Oceans*, *118*(5), 2408–2425. https://doi.org/10.1002/jgrc.20191

Lei, R., Gui, D., Hutchings, J. K., Heil, P., & Li, N. (2020). Annual cycles of sea ice motion and deformation derived from buoy measurements in the western arctic ocean over two ice seasons. *Journal of Geophysical Research: Oceans*, *125*(6). https://doi.org/10.1029/2019jc015310

Leppäranta, M. (2011). Free drift, 185–212. https://doi.org/10.1007/978-3-642-04683-4_6

Li, Z., Zhao, J., Su, J., Li, C., Cheng, B., Hui, F., Yang, Q., & Shi, L. (2019). Spatial and temporal variations in the extent and thickness of arctic landfast ice. *Remote Sensing*, *12*(1), 64. https://doi.org/10.3390/rs12010064

Lilja, V.-P., Polojärvi, A., Tuhkuri, J., & Paavilainen, J. (2021). Finite-discrete element modelling of sea ice sheet fracture. *International Journal of Solids and Structures*, *217-218*, 228–258. https://doi.org/https://doi.org/10.1016/j.ijsolstr.2020.11.028

Lin, L., Lei, R., Hoppmann, M., Perovich, D. K., & He, H. (2022). Changes in the annual sea ice freeze–thaw cycle in the arctic ocean from 2001 to 2018. *The Cryosphere*, *16*(12), 4779–4796. https://doi.org/10.5194/tc-16-4779-2022

Lopez-Acosta, R., Schodlok, M., & Wilhelmus, M. (2019). Ice floe tracker: An algorithm to automatically retrieve lagrangian trajectories via feature matching from moderate-resolution visual imagery. *Remote Sensing of Environment*, *234*, 111406. https://doi.org/10.1016/j.rse.2019.111406

Løset, S. (1994). Discrete element modelling of a broken ice field — Part I: Model development. *Cold Regions Science and Technology*, *22*(4), 339–347. https://doi.org/10.1016/0165-232x(94)90019-1

Lu, W., Lubbad, R., & Løset, S. (2015). In-plane fracture of an ice floe: A theoretical study on the splitting failure mode. *Cold Regions Science and Technology*, *110*, 77–101. https://doi.org/10.1016/j.coldregions.2014.11.007

Lubbad, R., & Løset, S. (2011). A numerical model for real-time simulation of ship–ice interaction. *Cold Regions Science and Technology*, *65*(2), 111–127. https://doi.org/10.1016/j.coldregions.2010.09.004

Makarov, O. A., & Bekker, A. T. (2021). Modeling of ice impacts using cohesive element method: Influence of element size. *IOP Conference Series: Earth and Environmental Science*, *666*(6), 062029. https://doi.org/10.1088/1755-1315/666/6/062029

Manucharyan, G. E., & Montemuro, B. P. (2022). SubZero: A sea ice model with an explicit representation of the floe life cycle. *Journal of Advances in Modeling Earth Systems*. https://doi.org/10.1029/2022ms003247

Manucharyan, G. E., & Thompson, A. F. (2022). Heavy footprints of upper-ocean eddies on weakened arctic sea ice in marginal ice zones. *Nature Communications*, *13*(1). https://doi.org/10.1038/s41467-022-29663-0

Meier, W. N. (2021). NOAA arctic report card 2021: Sea ice. https://doi.org/10.25923/Y2WD-FN85

Mercator Ocean International. (2015). Arctic ocean physics analysis and forecast. https://doi.org/10.48670/MOI-00001

Min, C., Yang, Q., Mu, L., Kauker, F., & Ricker, R. (2021). Ensemble-based estimation of sea-ice volume variations in the Baffin Bay. *The Cryosphere*, *15*(1), 169–181. https://doi.org/10.5194/tc-15-169-2021

MODIS Science Team. (2017). Modis/Terra calibrated radiances 5-min l1b swath 1km. https://doi.org/10.5067/MODIS/MOD021KM.NRT.061

Moncada, R., Gupta, M., Thompson, A., & Andrade, J. (2023a). Level set discrete element method for modeling sea ice floes. *Computer Methods in Applied Mechanics and Engineering*, *406*, 115891. https://doi.org/10.1016/j.cma.2023.115891

Moncada, R., Gupta, M., Thompson, A., & Andrade, J. (2023b). Role of breakage, melt and floe size distribution on sea ice summer transition. *Geophysical Research Letters*, *Pending*, Pending. https://doi.org/Pending

Moncada, R., Gupta, M., Thompson, A., & Andrade, J. E. (2023). Role of breakage, melt and floe size distribution on sea ice summer transition. *Geophysical Research Letters. In Review.*

Moncada, R., Ulloa, J., Gupta, M., Thompson, A., & Andrade, J. (2024). Impact of ocean currents on landfast sea ice fracture: Bonded discrete element method analysis. *Computer Methods in Applied Mechanics and Engineering. In Preparation.*

Montiel, F., & Squire, V. A. (2017). Modelling wave-induced sea ice break-up in the marginal ice zone. *Proceedings of the Royal Society A: Mathematical, Physical and Engineering Sciences*, *473*(2206), 20170258. https://doi.org/10.1098/rspa.2017.0258

Moon, T. A., M.L., D., & Thoman, R. (2021). NOAA arctic report card 2021 executive summary. https://doi.org/10.25923/5S0F-5163

Moore, G. W. K., Howell, S. E. L., Brady, M., Xu, X., & McNeil, K. (2021). Anomalous collapses of nares strait ice arches leads to enhanced export of arctic sea ice. *Nature Communications*, *12*(1). https://doi.org/10.1038/s41467-020-20314-w

Moore, G., Steele, M., Schweiger, A. J., Zhang, J., & Laidre, K. L. (2022). Thick and old sea ice in the beaufort sea during summer 2020/21 was associated with enhanced transport. *Communications Earth &amp Environment*, *3*(1). https://doi.org/10.1038/s43247-022-00530-6

Mulmule, S., & Dempsey, J. (2000). LEFM size requirements for the fracture testing of sea ice. *International Journal of Fracture*, *102*(1), 85–98. https://doi.org/10.1023/a:1007603428907

NOAA. (2022). Sea ice coastal erosion. https://www.pmel.noaa.gov/arctic-zone/detect/human-shishmaref.shtml

Notz, D., & Community, S. (2020). Arctic sea ice in CMIP6. *Geophysical Research Letters*, *47*(10). https://doi.org/10.1029/2019gl086749

NSDIC. (2022). http://nsidc.or/arcticseaicenews/2022/05/

Oggier, M., & Eicken, H. (2022). Seasonal evolution of granular and columnar sea ice pore microstructure and pore network connectivity. *Journal of Glaciology*, 1–16. https://doi.org/10.1017/jog.2022.1

Olonscheck, D., Mauritsen, T., & Notz, D. (2019). Arctic sea-ice variability is primarily driven by atmospheric temperature fluctuations. *Nature Geoscience*, *12*(6), 430–434.

Osher, S., & Fedkiw, R. (2001). Level set methods: An overview and some recent results. *Journal of Computational Physics*, *169*, 463–502.

Panteleev, G., Yaremchuk, M., Stroh, J. N., Francis, O. P., & Allard, R. (2020). Parameter optimization in sea ice models with elastic–viscoplastic rheology. *The Cryosphere*, *14*(12), 4427–4451. https://doi.org/10.5194/tc-14-4427-2020

Perovich, D. K., & Jones, K. F. (2014). The seasonal evolution of sea ice floe size distribution. *Journal of Geophysical Research: Oceans*, *119*(12), 8767–8777. https://doi.org/10.1002/2014jc010136

Plante, M., & Tremblay, L. B. (2021). A generalized stress correction scheme for the maxwell elasto-brittle rheology: Impact on the fracture angles and deformations. *The Cryosphere*, *15*(12), 5623–5638. https://doi.org/10.5194/tc-15-5623-2021

Polashenski, C., Perovich, D., & Courville, Z. (2012). The mechanisms of sea ice melt pond formation and evolution. *Journal of Geophysical Research: Oceans*, *117*(C1). https://doi.org/10.1029/2011jc007231

Rabatel, M., Labbé, S., & Weiss, J. (2015). Dynamics of an assembly of rigid ice floes. *Journal of Geophysical Research: Oceans*, *120*(9), 5887–5909. https://doi.org/10.1002/2015jc010909

RadioCanadaInternational. (2013). Inuit seal hunt. https://www.rcinet.ca/eye-on-the-arctic/2013/03/05/inuit-seal-hunt/

Rae, J. G. L., Hewitt, H. T., Keen, A. B., Ridley, J. K., West, A. E., Harris, C. M., Hunke, E. C., & Walters, D. N. (2015). Development of the global sea ice 6.0 CICE configuration for the Met office global coupled model. *Geoscientific Model Development*, *8*(7), 2221–2230. https://doi.org/10.5194/gmd-8-2221-2015

Ramadhan, A., Wagner, G., Hill, C., Campin, J.-M., Churavy, V., Besard, T., Souza, A., Edelman, A., Ferrari, R., & Marshall, J. (2020). Oceananigans.jl: Fast and friendly geophysical fluid dynamics on GPUs. *Journal of Open Source Software*, *5*(53), 2018. https://doi.org/10.21105/joss.02018

Rampal, P., Dansereau, V., Olason, E., Bouillon, S., Williams, T., Korosov, A., & Samaké, A. (2019). On the multi-fractal scaling properties of sea ice deformation. *The Cryosphere*, *13*(9), 2457–2474. https://doi.org/10.5194/tc-13-2457-2019

Rantanen, M., Karpechko, A. Y., Lipponen, A., Nordling, K., Hyvärinen, O., Ruosteenoja, K., Vihma, T., & Laaksonen, A. (2022). The arctic has warmed nearly four times faster than the globe since 1979. *Communications Earth and Environment*, *3*(1). https://doi.org/10.1038/s43247-022-00498-3

Ren, H., Zhang, C., & Zhao, X. (2021). Numerical simulations on the fracture of a sea ice floe induced by waves. *Applied Ocean Research*, *108*, 102527. https://doi.org/10.1016/j.apor.2021.102527

Rheinlænder, J. W., Davy, R., Ólason, E., Rampal, P., Spensberger, C., Williams, T. D., Korosov, A., & Spengler, T. (2022). Driving mechanisms of an extreme winter sea ice breakup event in the beaufort sea. *Geophysical Research Letters*, *49*(12). https://doi.org/10.1029/2022gl099024

Roach, L. A., Bitz, C. M., Horvat, C., & Dean, S. M. (2019). Advances in modeling interactions between sea ice and ocean surface waves. *Journal of Advances in Modeling Earth Systems*, *11*(12), 4167–4181. https://doi.org/10.1029/2019ms001836

Roach, L. A., Horvat, C., Dean, S. M., & Bitz, C. M. (2018). An emergent sea ice floe size distribution in a global coupled ocean-sea ice model. *Journal of Geophysical Research: Oceans*, *123*(6), 4322–4337. https://doi.org/10.1029/2017jc013692

Roberts, A. F., Hunke, E. C., Allard, R., Bailey, D. A., Craig, A. P., Lemieux, J.-F., & Turner, M. D. (2018). Quality control for community-based sea-ice model development. *Philosophical Transactions of the Royal Society A: Mathematical, Physical and Engineering Sciences*, *376*(2129), 20170344. https://doi.org/10.1098/rsta.2017.0344

Rosenblum, E., & Eisenman, I. (2017). Sea ice trends in climate models only accurate in runs with biased global warming. *Journal of Climate*, *30*(16), 6265–6278. https://doi.org/10.1175/jcli-d-16-0455.1

Rothrock, D. A., & Thorndike, A. S. (1984). Measuring the sea ice floe size distribution. *Journal of Geophysical Research*, *89*(C4), 6477. https://doi.org/10.1029/jc089ic04p06477

Sammonds, P., Montagnat, M., Bons, P., & Schneebeli, M. (2017). Ice microstructures and microdynamics. *Philosophical Transactions of the Royal Society A: Mathematical, Physical and Engineering Sciences*, *375*(2086), 20160438. https://doi.org/10.1098/rsta.2016.0438

Serreze, M. C., & Meier, W. N. (2018). The arctic's sea ice cover: Trends, variability, predictability, and comparisons to the Antarctic. *Annals of the New York Academy of Sciences*, *1436*(1), 36–53. https://doi.org/10.1111/nyas.13856

Serreze, M. C., & Stroeve, J. (2015a). Arctic sea ice trends, variability and implications for seasonal ice forecasting. *Philosophical Transactions of the Royal Society A: Mathematical, Physical and Engineering Sciences*, *373*(2045), 20140159.

Serreze, M. C., & Stroeve, J. (2015b). Arctic sea ice trends, variability and implications for seasonal ice forecasting. *Philosophical Transactions of the Royal Society A: Mathematical, Physical and Engineering Sciences*, *373*(2045), 20140159. https://doi.org/10.1098/rsta.2014.0159

Shrestha, K., & Manucharyan, G. E. (2022). Parameterization of submesoscale mixed layer restratification under sea ice. *Journal of Physical Oceanography*, *52*(3), 419–435. https://doi.org/https://doi.org/10.1175/JPO-D-21-0024.1

Smith, M. M., Holland, M., & Light, B. (2022). Arctic sea ice sensitivity to lateral melting representation in a coupled climate model. *The Cryosphere*, *16*(2), 419–434. https://doi.org/10.5194/tc-16-419-2022

Smith, M. M., Angot, H., Chamberlain, E. J., Droste, E. S., Karam, S., Muilwijk, M., Webb, A. L., Archer, S. D., Beck, I., Blomquist, B. W., Bowman, J., Boyer, M., Bozzato, D., Chierici, M., Creamean, J., D'Angelo, A., Delille, B., Fer, I., Fong, A. A., . . . Zhan, L. (2023). Thin and transient meltwater layers and false bottoms in the arctic sea ice pack—recent insights on these historically overlooked features. *Elem Sci Anth*, *11*(1). https://doi.org/10.1525/elementa.2023.00025

Squire, V. A. (2022). Marginal ice zone dynamics. *Philosophical Transactions of the Royal Society A: Mathematical, Physical and Engineering Sciences*, *380*(2235). https://doi.org/10.1098/rsta.2021.0266

Steele, M. (1992). Sea ice melting and floe geometry in a simple ice-ocean model. *Journal of Geophysical Research: Oceans*, *97*(C11), 17729–17738. https://doi.org/10.1029/92jc01755

Steiner, N. S., Bowman, J., Campbell, K., Chierici, M., Eronen-Rasimus, E., Falardeau, M., Flores, H., Fransson, A., Herr, H., Insley, S. J., Kauko, H. M., Lannuzel, D., Loseto, L., Lynnes, A., Majewski, A., Meiners, K. M., Miller, L. A., Michel, L. N., Moreau, S., . . . Wongpan, P. (2021). Climate change impacts on sea-ice ecosystems and associated ecosystem services. *Elementa: Science of the Anthropocene*, *9*(1). https://doi.org/10.1525/elementa.2021.00007

Stern, H. L., Schweiger, A. J., Stark, M., Zhang, J., Steele, M., & Hwang, B. (2018). Seasonal evolution of the sea-ice floe size distribution in the beaufort and chukchi seas (J. W. Deming & T. Maksym, Eds.). *Elementa: Science of the Anthropocene*, *6*. https://doi.org/10.1525/elementa.305

Stern, H. L., Schweiger, A. J., Zhang, J., & Steele, M. (2018). On reconciling disparate studies of the sea-ice floe size distribution (J. W. Deming & T. Maksym, Eds.). *Elementa: Science of the Anthropocene*, *6*. https://doi.org/10.1525/elementa.304

Stroeve, J. C., Markus, T., Boisvert, L., Miller, J., & Barrett, A. (2014). Changes in arctic melt season and implications for sea ice loss. *Geophysical Research Letters*, *41*(4), 1216–1225. https://doi.org/10.1002/2013gl058951

Sun, X., Duddu, R., & Hirshikesh. (2021). A poro-damage phase field model for hydrofracturing of glacier crevasses. *Extreme Mechanics Letters*, *45*, 101277. https://doi.org/10.1016/j.eml.2021.101277

Suryawanshi, K., Jena, B., Bajish, C. C., & Anilkumar, N. (2023). Recent decline in antarctic sea ice cover from 2016 to 2022: Insights from satellite observations, argo floats, and model reanalysis. *Tellus A: Dynamic Meteorology and Oceanography*, *75*(1). https://doi.org/10.16993/tellusa.3222

TheArcticInstitute. (2011). Exxonmobil gains access to arctic oil and gas reserves in deal with Rosneft. https://www.thearcticinstitute.org/exxonmobil-gains-access-arctic-oil/

Thorndike, A. S. (1992). A toy model linking atmospheric thermal radiation and sea ice growth. *Journal of Geophysical Research*, *97*(C6), 9401. https://doi.org/10.1029/92jc00695

Timmermans, M.-L., & Marshall, J. (2020). Understanding arctic ocean circulation: A review of ocean dynamics in a changing climate. *Journal of Geophysical Research: Oceans*, *125*(4). https://doi.org/10.1029/2018jc014378

Tooth, M., & Tschudi, M. (2018). Investigating arctic sea ice survivability in the Beaufort Sea. *Remote Sensing*, *10*(2), 267. https://doi.org/10.3390/rs10020267

Toyota, T., Takatsuji, S., & Nakayama, M. (2006). Characteristics of sea ice floe size distribution in the seasonal ice zone. *Geophysical Research Letters*, *33*(2). https://doi.org/10.1029/2005gl024556

Tuhkuri, J., & Polojärvi, A. (2018). A review of discrete element simulation of ice–structure interaction. *Philosophical Transactions of the Royal Society A: Mathematical, Physical and Engineering Sciences*, *376*(2129), 20170335. https://doi.org/10.1098/rsta.2017.0335

Turner, A. K., Peterson, K. J., & Bolintineanu, D. (2022). Geometric remapping of particle distributions in the discrete element model for sea ice (DEMSI v0.0). *Geoscientific Model Development*, *15*(5), 1953–1970. https://doi.org/10.5194/gmd-15-1953-2022

Valkonen, E., Cassano, J., & Cassano, E. (2021). Arctic cyclones and their interactions with the declining sea ice: A recent climatology. *Journal of Geophysical Research: Atmospheres*, *126*(12). https://doi.org/10.1029/2020jd034366

Van der Walt, S., Schönberger, J. L., Nunez-Iglesias, J., Boulogne, F., Warner, J. D., Yager, N., Gouillart, E., & Yu, T. (2014). Scikit-image: Image processing in python. *PeerJ*, *2*, e453.

Vlahinić, I., Kawamoto, R., Andò, E., Viggiani, G., & Andrade, J. E. (2016). From computed tomography to mechanics of granular materials via level set bridge. *Acta Geotechnica*, *12*(1), 85–95. https://doi.org/10.1007/s11440-016-0491-3

Wang, Q., Danilov, S., Mu, L., Sidorenko, D., & Wekerle, C. (2021). Lasting impact of winds on arctic sea ice through the ocean's memory. *The Cryosphere*, *15*(10), 4703–4725. https://doi.org/10.5194/tc-15-4703-2021

Wang, Y., Hwang, B., Bateson, A. W., Aksenov, Y., & Horvat, C. (2022). Summer sea ice floe size distribution in the arctic: High-resolution optical satellite imagery and model evaluation. *The Cryosphere*. https://doi.org/10.5194/tc-2022-130

Watkins, D. M., Bliss, A. C., Hutchings, J. K., & Wilhelmus, M. M. (2023). Evidence of abrupt transitions between sea ice dynamical regimes in the east greenland marginal ice zone. *Geophysical Research Letters*, *50*(15). https://doi.org/10.1029/2023gl103558

Wei, J., Zhang, X., & Wang, Z. (2019). Reexamination of fram strait sea ice export and its role in recently accelerated arctic sea ice retreat. *Climate Dynamics*, *53*(3-4), 1823–1841. https://doi.org/10.1007/s00382-019-04741-0

West, O'Connor, D., Parno, M., Krackow, M., & Polashenski, C. (2022). Bonded discrete element simulations of sea ice with non-local failure: Applications to nares strait. *Journal of Advances in Modeling Earth Systems*, *14*(6). https://doi.org/10.1029/2021ms002614

West, O'Connor, D. T., Parno, M., Krackow, M., & Polashenski, C. M. (2021). Improving discrete element simulations of sea ice break up: Applications to nares strait. *Journal of Advances in Modeling Earth Systems*. https://doi.org/10.1002/essoar.10507028.1

WHOI. (2023). https://divediscover.whoi.edu/polar-regions/arctic-ecosystem/

Willmes, S., Heinemann, G., & Schnaase, F. (2023). Patterns of wintertime arctic sea-ice leads and their relation to winds and ocean currents. *The Cryosphere*, *17*(8), 3291–3308. https://doi.org/10.5194/tc-17-3291-2023

Xu, Z., Tartakovsky, A. M., & Pan, W. (2012). Discrete-element model for the interaction between ocean waves and sea ice. *Physical Review E*, *85*(1). https://doi.org/10.1103/physreve.85.016703

Zhang, X., Tang, H., Zhang, J., Walsh, J. E., Roesler, E. L., Hillman, B., Ballinger, T. J., & Weijer, W. (2023). Arctic cyclones have become more intense and longer-lived over the past seven decades. *Communications Earth &amp Environment*, *4*(1). https://doi.org/10.1038/s43247-023-01003-0